Holographic Array Processing in the Ocean

by Azmi A. Al-Kurd

Technical Report
APL-UW TR 9306
March 1993

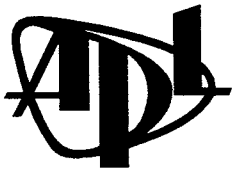

Applied Physics Laboratory University of Washington
1013 NE 40th Street Seattle, Washington 98105-6698

Report Documentation Page

Form Approved
OMB No. 0704-0188

1. REPORT DATE	2. REPORT TYPE	3. DATES COVERED
01 MAR 1993	**N/A**	**-**

4. TITLE AND SUBTITLE	5a. CONTRACT NUMBER
Holographic Array Processing in the Ocean	5b. GRANT NUMBER **ONR N00014-90-J-1369**
	5c. PROGRAM ELEMENT NUMBER

6. AUTHOR(S)	5d. PROJECT NUMBER
Azmi A. Al-Kurd	5e. TASK NUMBER
	5f. WORK UNIT NUMBER

7. PERFORMING ORGANIZATION NAME(S) AND ADDRESS(ES)	8. PERFORMING ORGANIZATION REPORT NUMBER
Applied Physics Laboratory University of Washington 1013 NE 40th St. Seattle, WA. 98105-6698	**APL-UW TR 9306**

9. SPONSORING/MONITORING AGENCY NAME(S) AND ADDRESS(ES)	10. SPONSOR/MONITOR'S ACRONYM(S)
Office of Naval Research 800 N. Quincy Street Arlington, VA. 22217-5660 ATTN: Code 3243	11. SPONSOR/MONITOR'S REPORT NUMBER(S)

12. DISTRIBUTION/AVAILABILITY STATEMENT

Approved for public release, distribution unlimited

13. SUPPLEMENTARY NOTES

This dissertation was submitted in partial fulfillment of the requirements for the degree of Doctor of Philosophy in the Department of Electrical Engineering at the University of Washington., The original document contains color images.

14. ABSTRACT

This dissertation provides detailed analysis, performance evaluation, and modeling of a source localization method that is based on medium calibration. In the past, processing the signals received on an array of sensors in the ocean to locate an acoustic source has been treated by methods which are based on detailed knowledge of the sound speed structure between the source and the receiving array.

15. SUBJECT TERMS

source localization, array processing, holography, virtual imaging, wavefront construction, underwater acoustics, wave propagation, ambient noise, truncated arrays, normal mode theory

16. SECURITY CLASSIFICATION OF:			17. LIMITATION OF ABSTRACT	18. NUMBER OF PAGES	19a. NAME OF RESPONSIBLE PERSON
a. REPORT	b. ABSTRACT	c. THIS PAGE			
unclassified	**unclassified**	**unclassified**	**UU**	**154**	

FOREWORD

This dissertation was submitted in partial fulfillment of the requirements for the degree of Doctor of Philosophy in the Department of Electrical Engineering at the University of Washington. Robert P. Porter, Head, Ocean Acoustics and Electromagnetics Department, Applied Physics Laboratory, and Professor of Electrical Engineering, was chairman of the Supervisory Committee. Financial support for this research was provided by the ARL Program, Office of Naval Research.

ABSTRACT

This dissertation provides detailed analysis, performance evaluation, and modeling of a source localization method that is based on medium calibration. In the past, processing the signals received on an array of sensors in the ocean to locate an acoustic source has been treated by methods which are based on detailed knowledge of the sound speed structure between the source and the receiving array.

The general problem considers an array of sensors distributed throughout the water column. From the signal measured at this array, the location (range and depth) of the unknown source is determined. A holographic array processing (HAP) algorithm is developed, which uses measured field data from the unknown source, and measurements from a reference source deployed near the target and transmitting at several depths. A virtual image of the wavefront from the unknown source is constructed at the location of the reference array by processing the measurements at the receiving array.

Conventional array processing algorithms, such as matched field processing (MFP), require precise knowledge of the medium between the source and the receiving array, but the HAP relaxes this stiff requirement. It calibrates the integrated effect of a great portion of the medium, and geoacoustic parameter estimation is needed only for a small portion of the ocean, between the unknown source and the virtual array. The virtual array is constructed by moving a reference source to incremental depths of the water column.

The detection criterion being used is based on the maximum intensity of the reconstructed field, which can be generated by weighting a replica field from a test source at a hypothetical location with the filtered wavefront from the unknown source at the virtual array.

Theoretical analysis is provided using the WKB approximation for a range dependent ocean with both N^2-bilinear and exponential stratification of the

sound speed profile (SSP). Also, numerical simulation is performed using a wide angle PE code[1] (FEPE) for a range dependent analytical SSP, and real sound speed data from the North Pacific ocean. The results of the analysis and simulation show the possibility of localizing a source at large distance with great accuracy.

In deep water, the ideal situation of having a receiving array and reference source that span the water column is prohibitively complex. How truncation of both the receiving and virtual arrays affects the performance of the HAP algorithm is investigated. Simulation for a range dependent, horizontally stratified ocean is performed using FEPE. It is shown that the holographic array processing algorithm is more susceptible to the length of the virtual array than the length of the receiving array.

Detailed analysis is provided for the case where the signals at the receiving array are observed in the presence of additive, spatially correlated ambient noise. For the numerical simulation, a simplified but representative, isotropic ambient noise model is used. It is shown that the power level of both the unknown and the reference source is critical to the performance of the HAP algorithm in the presence of ambient noise.

1. PE code is a numerical model for the wave propagation in a range dependent medium based on the parabolic approximation to the wave equation solution.

Table of Contents

List of Figures

List of Tables

ACKNOWLEDGMENTS

I would like to express gratitude to my committee members: Prof. Robert P. Porter, Prof. Dean W. Lytle, Prof. Blake Hannaford, Prof. Les E. Atlas, Prof. Donald B. Percival, and Prof. Chi H. Chan.

Special thanks are due my advisor, Professor Robert P. Porter, for his support, able guidance, constant encouragement and patience throughout my work on this dissertation.

Also, I would like to thank the University of Washington Applied Physics Laboratory staff whose contribution to this dissertation came in many forms. In particular, the technical assistance provided by Dr. Darrell R. Jackson, Dr. Donald B. Percival, Dr. Robert Odom, Dr. Pierre D. Mourad, Dr. Daniel Rouseff, Dr. Bruce M. Howe, Dr. Kevin Williams, William C. Kooiman, the library staff and the publication department is much appreciated. Special thanks to Monty Bolstad and Al Brookes for their general support and efficient handling of administrative and organizational matters. I want to express my special appreciation to George J. Dworski. My thanks to Thomas M. Siderius, David Frank-Molnia, and Christopher G. Walter for the help and company during the tough times.

This work was supported by U. S. Office of Naval Research contract N00014-90-J-1369.

Finally, I want to mention my deep and loving appreciation for my wife Shawn R. Al-Kurd. She stood by me through the long school years and always had an encouraging word during the most difficult periods.

With respect to what is contained herein, the words of Robert Service are offered as though mine:

> I have no doubt at all the Devil grins,
> as seas of ink I spatter.
> Ye gods, forgive my "literary" sins
> the other kind don't matter.

This dissertation is dedicated to humanity,

but most of all to my family.

INTRODUCTION

Processing the signals received on an array of sensors in the ocean to locate a sound source has been treated by methods which are based on detailed knowledge of the sound speed structure between the source and the receiving array.

This dissertation provides detailed analysis, performance evaluation, and modeling of a source localization method that is based on medium calibration.

1.0 Background

Underwater acoustics comprises a major part of ocean exploration research. Only sound waves can propagate in water over large distances. Practically all kinds of telemetry, communication, localization, and remote sensing of water masses and the ocean bottom use sound waves. Propagating over thousands of kilometers in the ocean, they bring information on remote objects, earthquakes, eruptions of volcanoes, distant storms, and global warming.

The most characteristic feature of the ocean medium is its inhomogeneous nature. There are two kinds of inhomogeneities, regular and random, and both strongly influence the underwater sound field. For example the regular variation of the sound velocity with depth leads to the formation of the underwater sound channel (USC), and as a consequence, to long range propagation. The random inhomogeneities give rise to scattering of sound waves and therefore to fluctuations in the sound field.

The general problem we consider here involves an array of sensors distributed throughout the water column. From the signal measured at this array, the location (range and depth) of the unknown source is determined. A holographic array processing (HAP) algorithm is developed, which uses measured field data from the unknown source and measurements from a reference source deployed near the target and transmitting at several depths. A virtual image of the wavefront from the unknown source is constructed at the location of the reference array by processing the measurements at the receiving array.

Conventional array processing algorithms, such as matched field processing

(MFP), require precise knowledge of the medium between the source and the receiving array, but the HAP relaxes this stiff requirement. It calibrates the integrated effect of a great portion of the medium, and geoacoustic parameter estimation is needed only for a small portion of the ocean, between the unknown source and the virtual array.

The detection criterion being used is based on the maximum intensity of the reconstructed field, which can be generated by weighting a replica field from a test source at a hypothetical location, with the filtered wavefront from the unknown source at the virtual array. It will be demonstrated that the HAP algorithm satisfies the detection criterion when the test source is at the location of the unknown target.

Our prime concern in this thesis will be to pose the HAP algorithm in precise terms and evaluate its performance for various system parameters and oceanic environments.

2.0 Approach

The analytical tools used in this research come from the fields of normal mode theory, multidimensional geometry, and multivariate statistics. The ocean model is assumed to be cylindrically symmetric with pressure release surface and absorbing bottom. Advantage is taken of the WKB approximation to the wave equation solution in a range dependent, horizontally stratified medium.

The computer simulation tools used in this thesis are based on a wide angle PE code, FEPE[1], and a normal mode code, for an adiabatic medium, based on the WKB approximation[2]. The geoacoustic data being used is both analytical and experimental.

The first chapter will shed some light on the intricacy of underwater wave propagation. The structure of the energy flow in the ocean makes the source localization problem very complex. Readers who are familiar with the funda-

---

1. FEPE was written by Mike Collins. The author modified the code for the HAP application.
2. This code was developed by the author using Matlab software.

mentals of underwater wave propagation can proceed to chapter 2.

Chapter 2 describes the problems associated with conventional source localization techniques and presents the motivation behind the HAP method. The HAP method has its genesis in optics, where the need to improve the resolution of imaging systems had led Goodman, Huntley, Jackson, and Lehman [1] to propose the use of a reference source in the vicinity of the object, record on a hologram the intensity caused by both the object and the reference, and then expose the hologram to a coherent reference only. This results in an improved image of the object. This chapter presents the HAP algorithm for source localization in a range dependent medium.

Chapter 3 provides theoretical and numerical evaluation of the performance of the HAP algorithm. The theoretical analysis is provided for an arbitrary adiabatic medium by the WKB approximation to the wave equation. Detailed results are obtained for a range dependent ocean with both N^2-bilinear and exponential stratification of the sound speed profile (SSP). Also, numerical simulation is performed using a wide angle PE code, FEPE, for a range dependent analytical SSP, and real sound speed data from the North Pacific ocean.

Chapter 4 presents the effect of truncating the receiving and virtual array on the performance of the HAP algorithm. It will be demonstrated that the performance of the HAP algorithm is more severely degraded by truncating the virtual array than by truncating the receiving array.

Chapter 5 provides detailed analysis for the performance of the HAP algorithm in the presence of additive, spatially correlated ambient noise. Numerical simulation is provided for the case when both the target and reference signals are contaminated by the ambient noise. A simplified, but representative isotropic ambient noise model will be used for the numerical simulation.

3.0 Contribution

There are four areas within which contributions have been made:

First, the geometry of the emitter location problem is defined. The distribution of the receiving and reference array relative to the location of the unknown source is determined. The issue of sampling the receiving and virtual array is discussed.

Second, the holographic array processing method is implemented for source localization in a range dependent ocean. Detailed theoretical and numerical analysis is provided. The theoretical analysis is based on the WKB approximation to the solution of the wave equation. The numerical modeling is performed using normal mode code for an adiabatic medium and a high-order PE code (FEPE) which is based on the Pade series approximation to the wave equation. The performance of the holographic method is compared with the performance of conventional methods, such as matched field processing.

Third, the performance of the holographic method in different environmental conditions is evaluated. Detailed theoretical and numerical analysis is provided for the effect of the sound speed profile variation with range and the presence of ambient noise.

Fourth, the performance of the holographic method with varying system parameters is evaluated. Detailed theoretical and numerical analysis is provided for the effect of implementing a truncated receiving and a truncated virtual array.

4.0 Glossary

$\hat{a} = (r', z')$	The test source location
$C(r)$	Eq. (3-11)
c(z,r)	Sound speed [m/sec] at depth z and range r
c_{a0}	Axial sound speed at range zero (reference sound speed)
c_a	Axial sound speed [m/sec]
c_{tp}	Sound speed at a turning point
$E^{TR}(r', z')$	The error term due to truncating the receiving array
$E^{TV}(r', z')$	The error term due to truncating the virtual array
FEPE	Computer code based on higher-order approximation to the PE
f	The acoustical frequency in [Hz]
G(r,z)	Green's function
$G_{12}(d,f)$	Spatial cross-spectral density
HAP	Holographic Array Processing
$H(z_R)$	The holographic image at reference depth z_R
h	The water depth at the receiving array
h_R	The water depth at the reference array
$\hat{h}$	The length of the truncated receiving array
$\hat{h}_R$	The length of the truncated virtual array
I	Intensity

k	wavenumber $= \frac{2\pi}{\lambda} = \frac{\omega}{c}$
MFP	Matched Field Processing
N(z,r)	Normalized index of refraction
$N(\theta)$	Ambient noise intensity per solid angle
PE	Parabolic Equation
P(r,z)	Complex pressure field at range r and depth z
P_t	Pressure field from the target
P_R	Pressure field from the reference source
$Q(r', z')$	The reconstructed field at range r' and depth z'
$R_{12}(d, \tau)$	Temporal-spatial cross correlation function
S or s	The horizontal gradient in the sound speed
S_u	The slope of the upper portion of the N^2-bilinear profile
S_{lo}	The slope of the lower portion of the N^2-bilinear profile
SNR	Signal to noise ratio
SSP	Sound Speed Profile
TL	Transmission Loss
z	Depth [m]
z_{ltp}	Depth of the lower turning point
z_{utp}	Depth of the upper turning point
α	Attenuation factor [dB/m]
$\alpha(m)$	Eq. (3-15)

$\beta(r)$	Eq. (3-16)
γ	The vertical eigennumber
$\Delta_t = r_t - r_R$	The separation between the target and the reference array
$\Delta = r' - r_R$	The separation between the test source and the reference array
$\delta_\varepsilon = r' - r_t$	The separation between the test source and the target
η_m	Eq. (3-1), the phase term in the modal expression of Q
$\theta(z_1,z_2)$	The phase accumulation in the vertical between z_1 and z_2
λ	The acoustic wave length
ξ	The horizontal eigennumber (eigenvalue)
ξ_m	The modal eigennumber
σ_t^2	The power of the unknown target [dB]
σ_R^2	The power of the reference source [dB]
σ_{nt}^2	The intensity of the ambient noise [dB]
ϕ_m	The exit angle that corresponds to mode m
$\Psi(r,z)$	The eigenfunction at range r and depth z
Ψ_m	The modal eigenfunction
Ω	Solid angle
ω	The acoustical frequency in radians; $\omega = 2\pi f$

CHAPTER 1

Underwater Wave Propagation

The ocean, together with its boundaries, forms a remarkably complex medium for the propagation of sound. Propagating through the ocean, an underwater sound signal becomes delayed, distorted, smeared, and weakened.

1-1 Transmission Loss

Transmission loss quantitatively describes the weakening of signal between a reference point (one meter from the source) and the point under consideration. If I_0 is the intensity at the reference point and I_1 is the intensity at a distant point, then transmission loss at the distant point is

$$TL = 10\log\left(\frac{I_0}{I_1}\right) \quad . \tag{1-1}$$

Transmission loss summarizes the effect of a variety of underwater propagation phenomena, and can be considered as the sum of a loss due to spreading and a loss due to attenuation.

1-1.1 Spreading Loss

Spreading loss is a geometrical effect representing the weakening of the signal as it spreads outward from the source. Two kinds of spreading are of special interest in underwater propagation.

- Spherical spreading: The power generated by the source is radiated equally in all directions, and, assuming no loss in the medium, then the power crossing all spheres must be the same:

$$P = 4\pi r_0^2 I_0 = 4\pi r_1^2 I_1 = \ldots = 4\pi r_n^2 I_n \tag{1-2}$$

where r_0 is the reference distance (usually one meter), and I_n is the intensity of sound at range r_n. Transmission loss in decibels is

$$TL = 10\log\left(\frac{I_0}{I_n}\right) = 10\log\left(\frac{r_n^2}{r_0^2}\right) = 20\log(r_n) \quad . \tag{1-3}$$

- Cylindrical spreading: The power radiated by the source is distributed over the surface of a cylinder having a radius equal to the range and a height equal to the distance between the upper and lower boundaries of the medium:

$$P = 2\pi r_0 H I_0 = 2\pi r_1 H I_1 = \ldots = 2\pi r_n H I_n \tag{1-4}$$

and the transmission loss in decibels is

$$TL = 10\log\left(\frac{I_0}{I_n}\right) = 10\log\left(\frac{r_n}{r_0}\right) = 10\log(r_n) \quad . \tag{1-5}$$

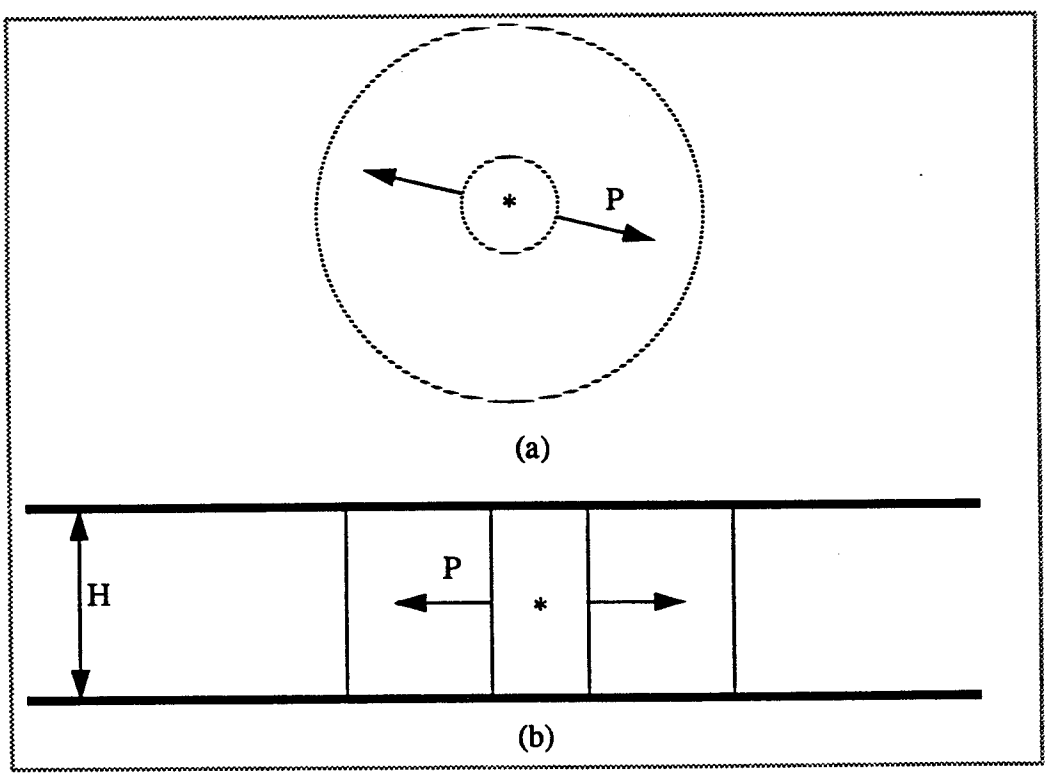

FIGURE 1-1. (a) Spherical spreading in unbounded medium. (b) Cylindrical spreading between two parallel planes.

1-1.2 Attenuation Loss

Attenuation loss includes the effects of absorption, scattering, and leakage out of sound channels. The presence of attenuation will lead to a modification to the transmission loss expressions. For spherical spreading

$$TL = 20\log(r) + \alpha r \quad , \tag{1-6}$$

and for cylindrical spreading

$$TL = 10\log(r) + \alpha r \quad , \tag{1-7}$$

where r is the range in meters, and α is the attenuation in dB/meter.

Extensive theoretical and experimental analysis have been conducted [2] to study the behavior and causes of wave attenuation in the sea water. It has been found that the main factors that cause the absorption of sound in the sea water are:

- volume viscosity due to some relaxation processes in sea water,
- scattering of sound waves by inhomogeneities of different kind.

The empirical formula, due to Marsh and Schulkin [3], for attenuation coefficient in sea water at frequencies between 3 kHz and 0.5 MHz is

$$\alpha = 8.68 \times 10^3 \left(\frac{2.34 \times 10^{-6} S f_T f^2}{f_T^2 + f^2} + \frac{3.38 \times 10^{-6} f^2}{f_T} \right) (1 - 6.54 \times 10^{-4} P) \tag{1-8}$$

where S is the salinity [parts per thousand], 0<S<37, P is the pressure [kg/cm^2], 1<P<1000, f is the frequency [kHz], $f_T = 21.9 \times 10^{6 - 1520/(T+273)}$ is the relaxation frequency [kHz], and T is temperature [^{o}C]. Since T ranges between 0^o and 30^o, then f_T ranges between 59 and 210 kHz.

At low frequencies (100 Hz - 3 kHz) the attenuation is better described by Thorp's formula [4]

$$\alpha = \frac{0.11f^2}{1+f^2} + \frac{44f^2}{4100+f^2} \quad , \tag{1-9}$$

where α is the attenuation coefficient in dB/km.

Fig. 1-2 shows the attenuation coefficient , α, as a function of frequency on a logarithmic scale. The curve is calculated for T=20°C, S=35 parts per thousand, and P=100 kg/cm^2.

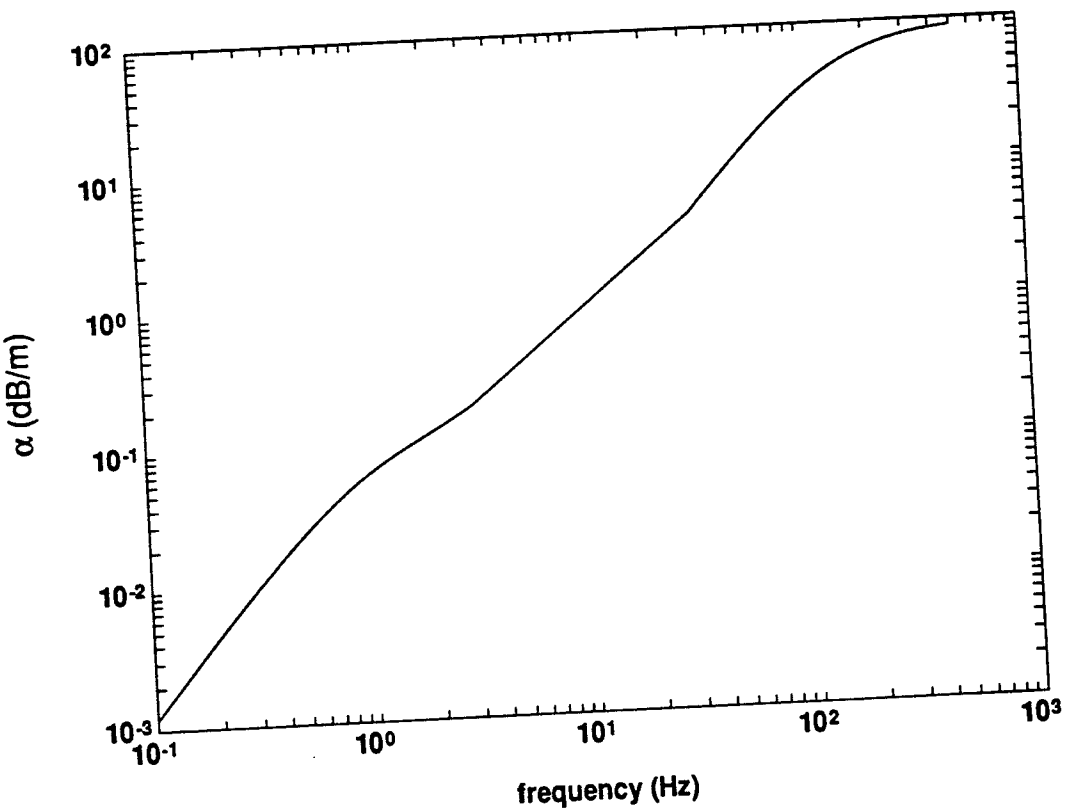

FIGURE 1-2. Attenuation coefficient in seawater as a function of frequency.

1-2 Sound Speed Structure in the Ocean

The sound speed profile (SSP) reveals the variation of sound velocity with depth. Several empirical expressions for the sound speed as a function of depth, temperature, and salinity were proposed by many researchers. The most accurate

formula is the one developed by Wilson [5]. However, it is a complicated expression containing many high-order and cross-product terms, and cannot be implemented without the use of a computer. Leroy [6] proposed simpler expressions that are believed to fit the data as well as the Wilson formula. Leroy's formula, often sufficient for practical work, is

$$c = 1492.9 + 3\,(T-10) - 0.006\,(T-10)^2 - 0.04\,(T-18)^2 + 1.2\,(S-35) - 0.01\,(T-18)\,(S-35) + \frac{Z}{61} \tag{1-10}$$

where c is the sound speed, T is temperature [°C], S is the salinity [parts per thousand] (0<S<37), and Z is the depth in meters.

1-2.1 Layers of the SSP in the Ocean

A typical deep water SSP is shown in Fig. 1-3. The profile may be divided into several layers having different thicknesses, characteristics and occurrence depending on the latitude, season, time of the day, and meteorological conditions. These layers are:

- Surface layer, just below the sea surface. The sound speed in this layer is susceptible to daily and local changes of heating, cooling and wind action. This layer may contain a mixed layer of isothermal water that is formed by the action of wind as it blows across the surface above. Sound tends to be trapped or channeled in this mixed layer. Under prolonged calm and sunny conditions the mixed layer disappears and is replaced by water in which the temperature decreases with depth.
- Seasonal thermocline, just below the surface layer. In this layer the temperature changes with depth. This layer is characterized by a negative thermal or sound speed gradient that varies from season to season. During the summer and fall, when the near-surface water of the sea is warm, the seasonal thermocline is strong and well defined; during winter and spring and in the Arctic, it tends to merge with, and be undistinguished from, the surface layer.

- Main thermocline, just below the seasonal thermocline. This layer is affected only slightly by seasonal changes. Temperature and velocity decreases with depth.
- Isothermal layer, below the main thermocline. This layer has nearly constant temperature near 4°C. The speed of sound increases with depth because of the effect of pressure (depth) on the sound speed.
- SOFAR (SOund Fixing And Ranging) axis. Between the negative sound speed gradient of the main thermocline and the positive sound speed gradient of the isothermal layer, there is a minimum sound speed. Sound traveling at great depths tends to be bent or focused by refraction toward the SOFAR axis.

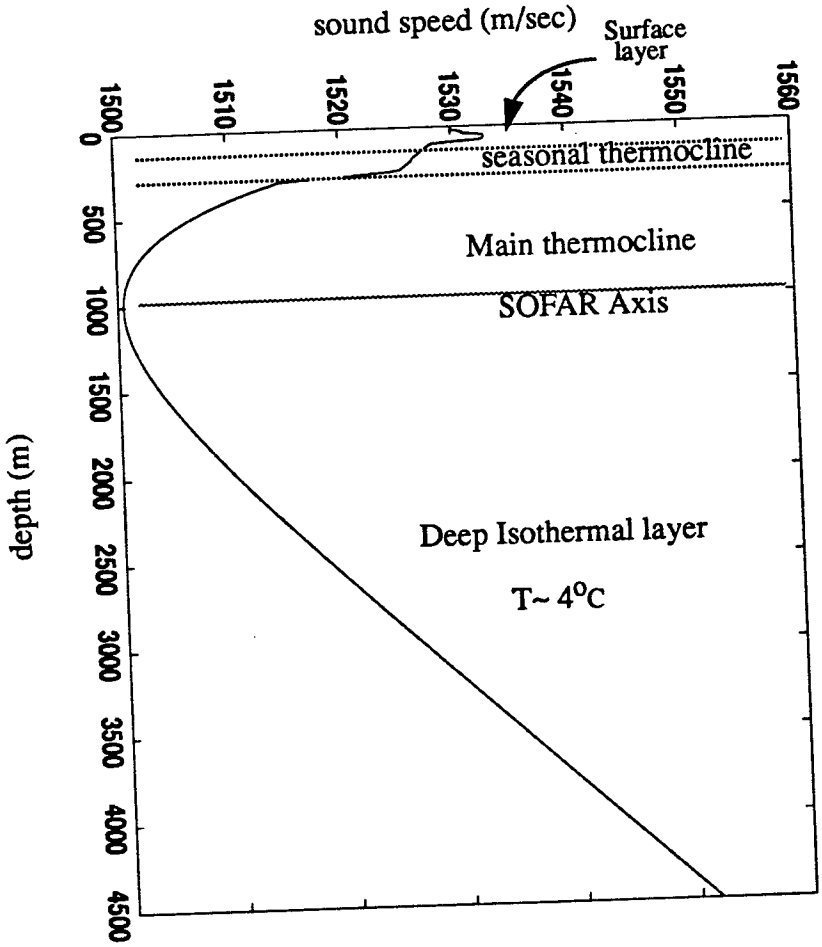

FIGURE 1-3. Typical deep-ocean Sound Speed Profile (SSP) divided into layers.

1-3 Patterns of Sound Propagation in the Ocean

As the sound wave leaves the source, it follows different ray paths, and the wave propagates along each path with different velocity, making the wavefront nonplanar. Two major types of paths exist, reflected and refracted paths.

Reflected paths are created upon reflection from the surface and/or the bottom; these paths are not important for long range propagation, because of the attenuation (loss) associated with them upon reflection. Refracted paths, on the other hand, carry with them the relative information about the source and volume of the medium. These paths are confined between turning points that can be found from Snell's law

$$\frac{\cos\varphi_a}{c_a} = \frac{\cos\varphi_i}{c_i} = \ldots = \frac{\cos\varphi_N}{c_N} \tag{1-11}$$

where φ_a is the initial ray exit angle, and

$$\left|\varphi_a^{max}\right| < \sqrt{\frac{(c_{tp}-c_a)^2}{c_{tp}}} \quad , \tag{1-12}$$

φ_i is the ray angle with the horizontal at depth z_i,

φ_{tp} is the array angle with the horizontal at the turning point, $\varphi_{tp}=0^o$,

c_i is the sound speed at depth z_i,

c_{tp} is the sound speed at the turning point.

The sound energy is trapped in the USC (Underwater Sound Channel) and does not reach the boundaries; therefore, the wave will not undergo scattering and absorption at these boundaries. The greater $\Delta c = c_{tp} - c_a$, the larger is the interval of angles in which the rays are trapped; i.e. the waveguide is more effective.

The maximum distance of sound propagation in the USC is limited mainly by absorption in the sea water. Sound of sufficiently low frequency, for which

absorption is fairly small, can propagate over hundreds and thousands of kilometers.

1-3.1 Caustics and Convergence Zones

In a ray diagram, a caustic is the envelope formed by the intersection of adjacent rays. It is a region of partial focusing with high intensity. When a caustic intersects the sea surface, the region at or near the surface, within which high sound levels occur, is known as a convergence zone.

Fig. 1-4 shows ray diagrams for a source at different depths in an ocean with the SSP shown in Fig. 1-3. These diagrams illustrate the following features for a fairly typical ocean:

- The variation of relative insonification and shadow zones at different depths and ranges for selected source positions.
- The strong convergence and shadow zones for a source near the surface or the bottom.
- The importance of caustics in all cases.

As the source approaches the USC axis, the width of the shadow zones decreases and that of the insonified zones increases. If the source is on the axis of the USC, shadow zones disappear at this depth. Several rays arrive at the receiver if the latter is not far from the USC axis. Such multipath propagation is a characteristic feature of the sound field in the USC.

The spatial and temporal (multipath) structure of the energy flow reveals the difficulty of locating an emitter in the far field. As an example, if the receiver is located in a shadow zone, then the source will not be heard; therefore, it will not be detected. Also, if the receiver is located in an insonified zone, then it will receive multiple signals from various directions over a period of time, causing ambiguity in determining the exact location of the source. The time spread of the received signals is a result of the medium stratification, where different rays (paths) will travel with different velocities.

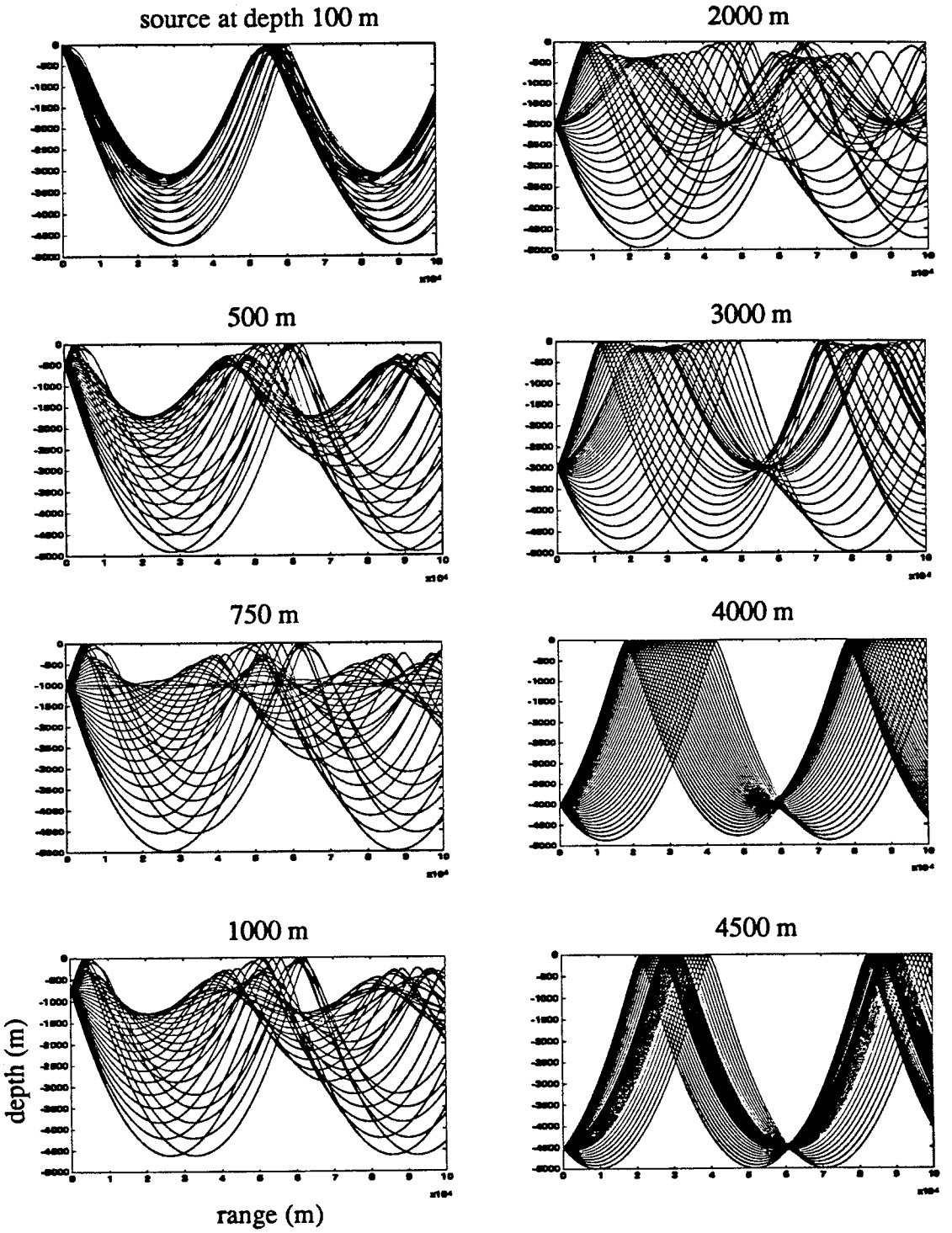

FIGURE 1-4. Ray diagram for source at different depths, as shown on the graphs, for an ocean with sound speed profile shown in Fig. 1-3.

CHAPTER 2

Underwater Source Localization

In recent years, scientists and engineers have shown an increasing interest in merging underwater propagation models with signal processing algorithms. Here, we will present three ways of tackling the source localization problem. The first two approaches are based on meticulous knowledge of the sound speed structure; the third approach is a novel one, and is based on acoustic calibration. The general problem is to infer the location of the acoustic source from the measured field at a vertical receiving array, Fig. 2-1.

2-1 Backpropagation Method

The location of an acoustic source can be determined by backpropagating, in the same medium, the measured field on the receiving array. This will lead the backpropagating wavefronts to converge at the source location.

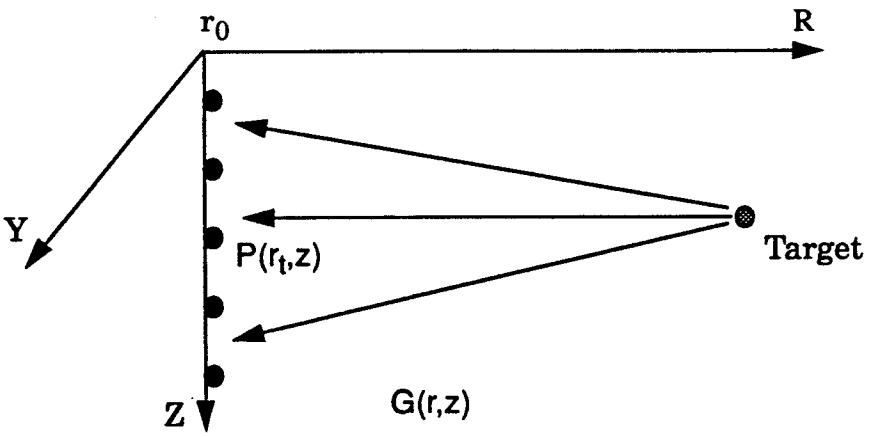

FIGURE 2-1. Backpropagation method. In ideal situation P(r,z) will focus at $r=r_t$ and $z=z_t$.

The measured pressure field, $P(r_t, z_t; r_0, z)$, can be backpropagated, toward the unknown source, by convolving its conjugate with the spatial impulse response of the medium. Meticulous oceanographic information is needed for accurate representation of the spatial impulse response of the medium.

The back propagated pressure field, from the receiving array through a medium with estimated spatial impulse response, is

$$P(r, z) = \int P_t^* (r_t, z_t; r_0, \tilde{z})\, \hat{G}(r, z; r_0, \tilde{z})\, d\tilde{z} \qquad (2\text{-}1)$$

where $P_t^* (r_t, z_t; r_0, \tilde{z})$ is the complex conjugate of the pressure field from the target at (r_t, z_t), as measured at a vertical receiving array located at range r_0; $\hat{G}(r, z; r_0, \tilde{z})$ is the estimated spatial impulse response of the medium between the point (r, z) and a hydrophone at $(r_0, \tilde{z})$.

The integral in Eq. (2-1) is performed along the receiving array at range r_0. Ideally, P(r,z) will focus at the exact location of the source, $r=r_t$ and $z=z_t$. The quality of the focus depends on the accuracy of the estimated Green's function, $\hat{G}(r, z)$.

2-2 Matched Field Processing Method

Bartlett developed an algorithm for plane wave propagation in a homogeneous medium. Matched-field processing (MFP) is a generalization of plane-wave beamforming [7], where the plane-wave weighting vectors, i.e., replicas, are replaced by solutions to the wave equation for the particular environment of interest.

Matched field processing has been investigated in underwater acoustics for more than ten years. Matched field processors use the field measurements as the inputs and obtain the source coordinates as the output. This processor is implemented by constructing forward solutions of the wave equation for many test source locations (the replica fields) and finding the best "match" to the measured data. This processor is ill-posed [8]; it is highly unstable to such effects as noise, errors in the input parameters and the introduction of new data. The matched-field problem itself is ill-posed in that it is very sensitive to errors in the model. This is usually referred to as the "mismatch" problem.

MFP methods require accurate oceanographic information about the medium, such as the sound speed structure between the source and the receiving array, the attenuation and scattering strength, the bathymetry, and the characteristics and structure of the ocean bottom. Collecting and maintaining an updated version of this information over a dense grid (with range increment about half

the wavelength) is a very complicated task. Therefore, inaccurate oceanographic information will result in false replica fields, and as a consequence MFP will fail to provide a unique solution to the source location problem.

An ambiguity function is defined in terms of the measured and replica fields. The peaks of the ambiguity function correspond to estimates of the source location candidates. Fig. 2-2 shows a block diagram of a conventional matched field processor. $P(a)$ is the measured pressure field from the source along the receiving array; $P(\hat{a})$ are the replica fields generated by a numerical wave propagation model such as PE; each replica field represents the pressure field along the receiving array from a hypothetical test source at range r′ and depth z′. Different algorithms use different rules to find the ambiguity surface $S(\hat{a})$. Bartlett, or the conventional estimator, has the ambiguity surface

$$S(\hat{a}) = P^*(\hat{a}) R P(\hat{a}) \tag{2-2}$$

where the * denotes the complex conjugate, $\hat{a} = (r', z')$ is the estimated source location, and R is the cross spectral matrix of the received field whose (i,j) th element is

$$R_{ij} = E[d_i d_j^*] \tag{2-3}$$

where d_i denotes the discrete Fourier transform of the received field, $P_t(a)$, on hydrophone i. Assuming the measurement was accomplished over a period of time T, then the discrete Fourier transform is performed at the frequency being used for localization [9] and then the expected value is calculated by averaging over a sequence of time frames.

The minimum variance method (Capon estimator) is given by

$$S(\hat{a}) = 1 / \{P^\dagger(\hat{a}) R^{-1} P(\hat{a})\} \quad . \tag{2-4}$$

In case of normal distribution, the Capon estimator is usually referred to as the maximum likelihood (ML) estimator[10].

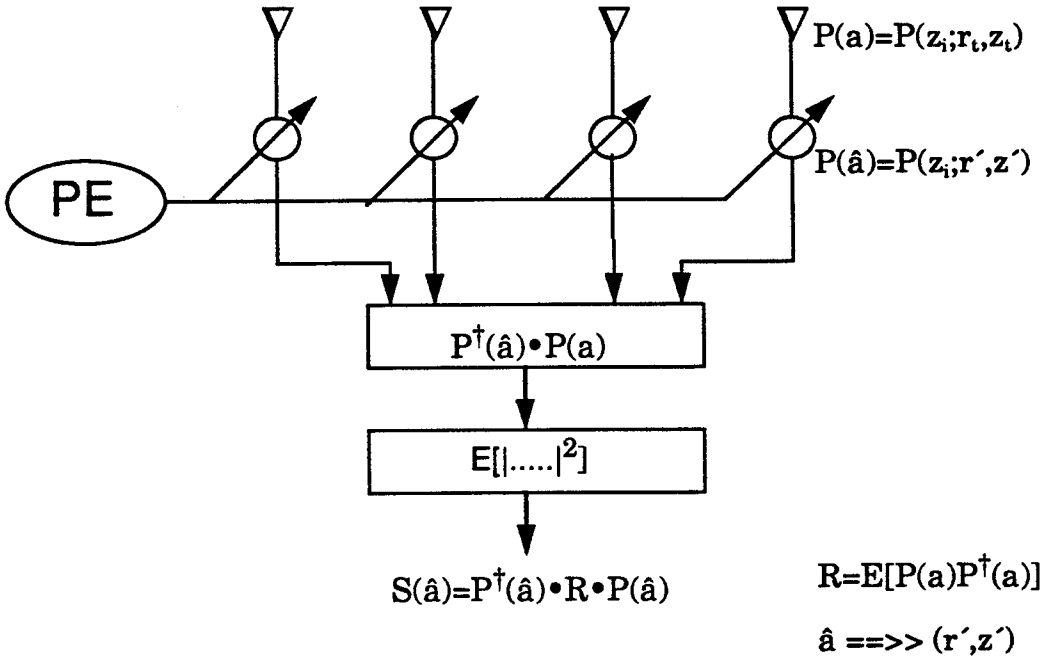

FIGURE 2-2. Conceptual diagram of the conventional matched field processor method.

Figs. 2-3 through 2-6 represent the SSP and the ambiguity surface for a Bartlett MFP for a target located at the axis of the channel and at range 100 km from the receiving array. The acoustic frequency being used for localization is 100 Hz. The ambiguity surface is plotted over 50 km (75 km to 125 km from the receiving array). The simulation was done using a wide angle parabolic equation (PE) code, FEPE, where the ocean was assumed to be range dependent to simulate the measured field. A range independent SSP was used to generate the replica fields. The range dependence was modeled as a linear variation of the sound speed at the axis on the order of one meter per second per hundred kilometers. It is evident from Fig. 2-4, where the red is a high intensity area and blue is a low intensity, that the focus is blurred, and the volume is populated with false images. Fig. 2-5 shows a horizontal slice of the ambiguity surface at the source's depth. High sidelobes indicate the existence of images at ranges other than the target's range, in this case 100 km from the receiving array. Fig. 2-6 is the same as Fig. 2-5, except the scanning is performed over a cylinder of radius 5 km

from the target; we notice the wide main lobe at the target's range which indicates a blurred focus.

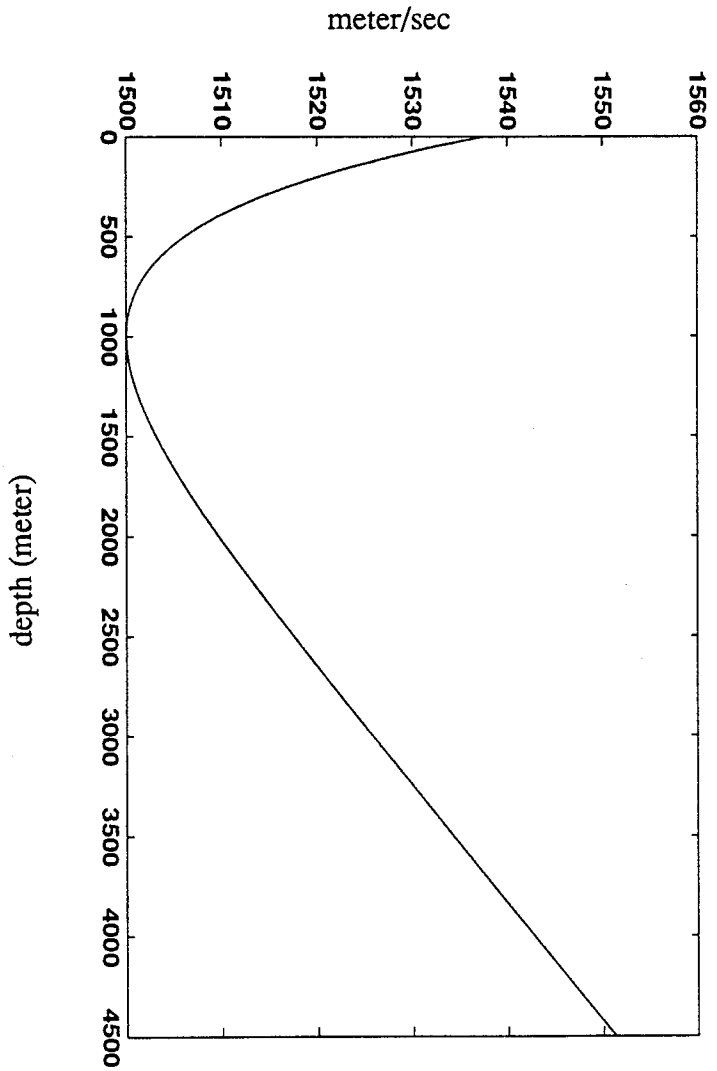

FIGURE 2-3. Sound Speed Profile for a range independent ocean.

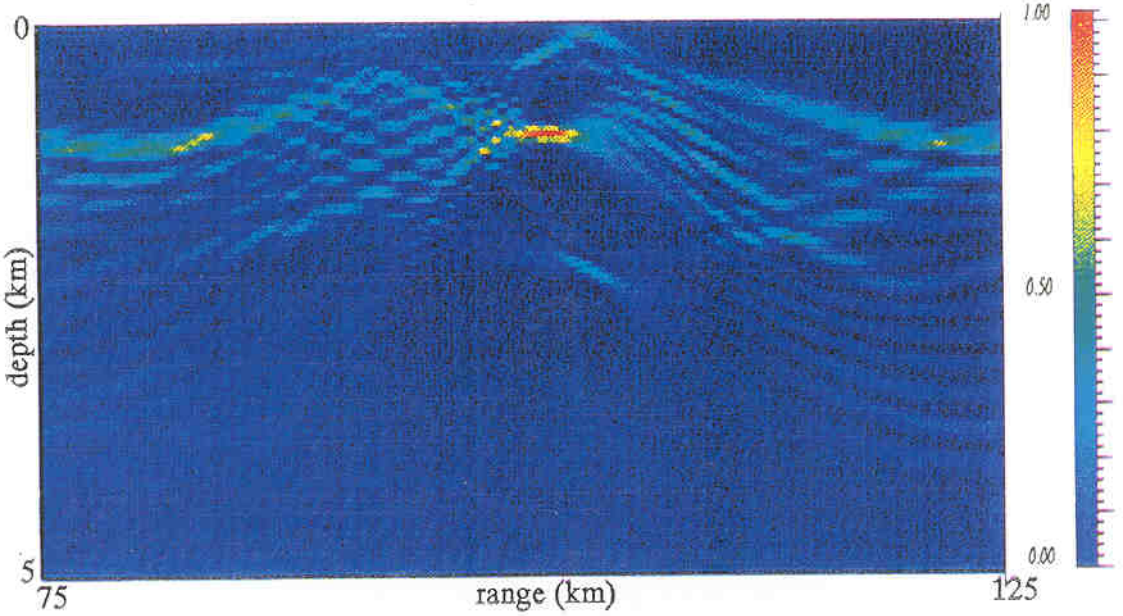

FIGURE 2-4. Color Image of the ambiguity surface for the MFP. The target is at range 100 km and depth 1000 m. The color bar shows the linear scale of the normalized intensity grading.

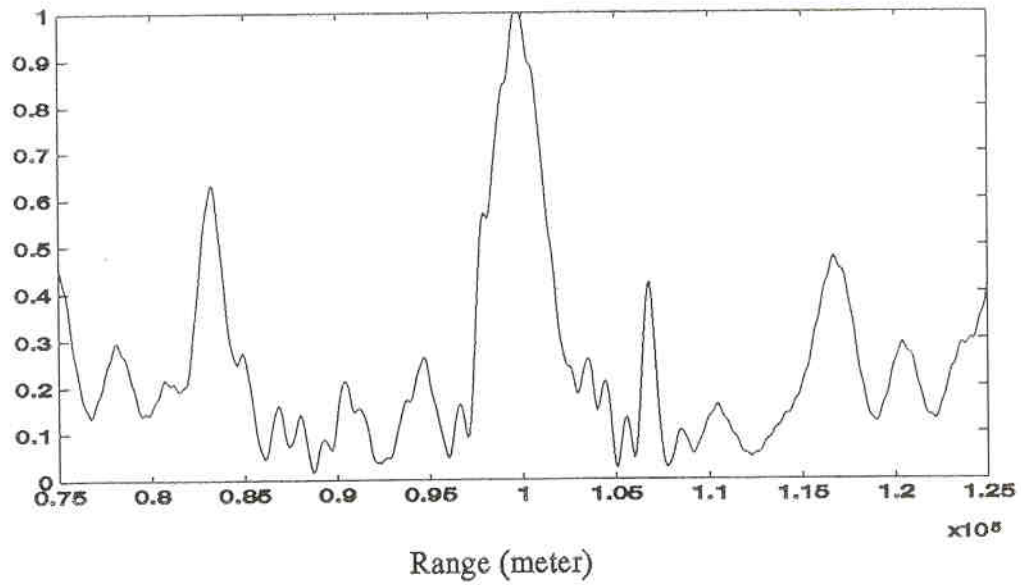

FIGURE 2-5. A horizontal slice of the MFP ambiguity surface at $z=z_t=1000$ m.

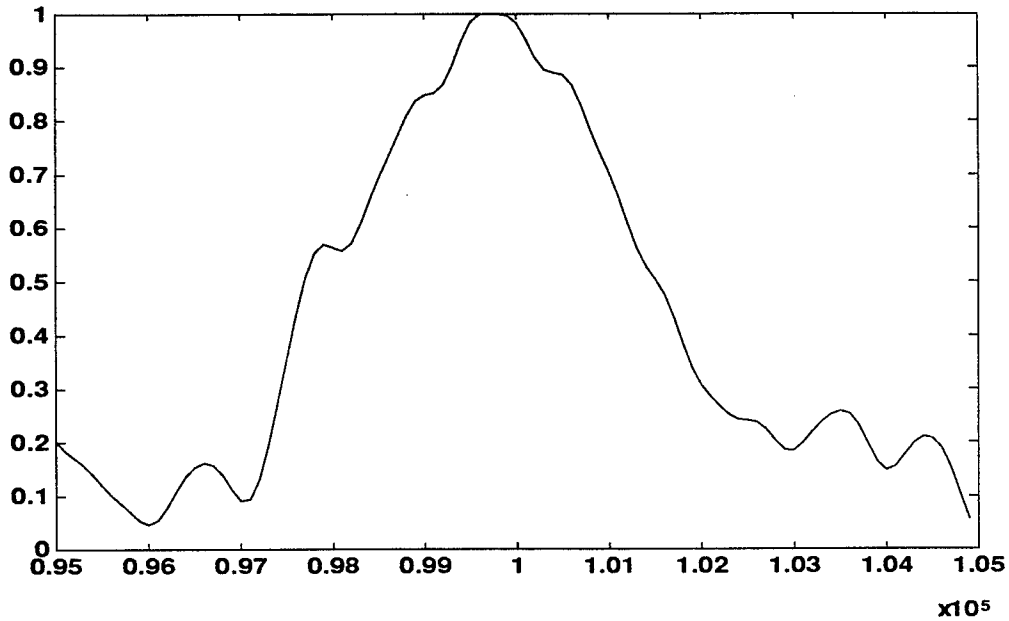

FIGURE 2-6. Same as figure 2-5, but zoomed-in around the source.

2-3 The Holographic Approach

The mismatch in the MFP methods can be reduced by using a reference source near the target. This approach brings the source into focus by calibrating most of the ocean between the source and the receiving array. The holographic method has its genesis in optics.

2-3.1 Holography in Optics

An outstanding problem in optics has been the desire to minimize the effect of the medium on the resolution capability of imaging systems, Goodman, Huntley, Jackson, and Lehman [1] has proposed the use of a reference source in the vicinity of the object, so that the object and reference rays received at any one point on the recording plane (hologram) pass through identical portions of the perturbing medium. The distortions of the reference and object waves are thus nearly identical as illustrated in Fig. 2-7. The reference and object waves reaching the hologram may thus be written as $P_R(x,y)\,exp\,[j\beta(x,y)]$ and

$P_t(x, y)\, exp\,[j\beta\,(x, y)]$, where $exp\,[j\beta\,(x, y)]$ is the transmittance of the aberrating medium. The hologram records the average intensity of the total field

$$I = |P_R|^2 + P_R^* P_t + P_R P_t^* + |P_t|^2 \tag{2-5}$$

where P_t^* is the complex conjugate of the object field, and P_R is the reference field. The interference pattern between the two is free from the distorting effects of the aberrating medium. This technique will work over a limited object field, since points too far from the reference may produce waves with aberrations different than those of the reference wave.

A Hologram is a film [11] with transmittance

$$T = KI^{\gamma} \tag{2-5)a}$$

where K is a positive constant, γ is the film contrast factor[1], and I is the recorded intensity. Therefore, coherent illumination of the hologram yields

$$I\hat{P}_R = |P_R|^2 \hat{P}_R + P_R^* P_t \hat{P}_R + P_R P_t^* \hat{P}_R + |P_t|^2 \hat{P}_R \tag{2-6}$$

where we assumed $\gamma = 1$. $\hat{P}_R$ is the reference field in the absence of the aberrating medium. The fourth term, in Eq. (2-6), can be neglected under the assumption that the reference intensity is greater than the object intensity, $|P_R|^2 \gg |P_t|^2$. The result is a pair of twin images of the object symmetrically located about a bright image of the reference.

Fig. 2-8 illustrates experimental results [1] obtained using conventional and wavefront reconstruction imaging techniques. The object is a transparency containing both a sign and a bright reference point, as shown in Fig. 2-8(a). The aberrating medium was common shower glass. Fig. 2-8(d) shows the wavefront reconstruction images obtained in the presence of the aberrating medium. For comparison, Fig. 2-8(b) shows the conventionally formed images, obtained by

1. γ is the slope of the linear region of the Hurter-Driffield (H&D) curve that relates the photographic density to the logarithm of exposure. A film with large γ is called a high-contrast film, while the one with low γ is called a low-contrast film.

replacing the film with a positive lens which directly forms the image in the presence of the aberrating medium. Resolution in the conventionally formed image has been totally destroyed by the aberrations. The wavefront-reconstruction images, however, have suffered minor degradations.

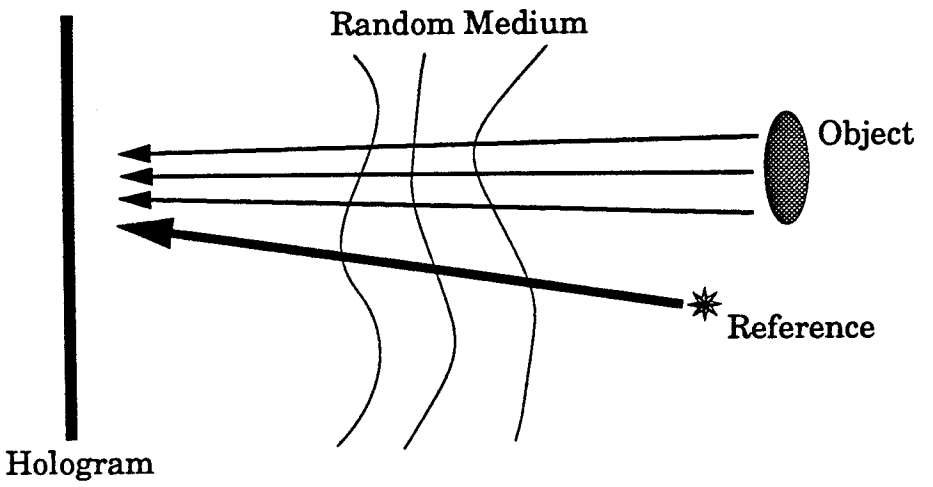

Recording step===>> $I = |(P_R + P_t)|^2 = I_R + I_t + P_R^* P_t + P_R P_t^*$

Reconstruction===>> $I\hat{P}_R = I_R \hat{P}_R + I_R P_t + \hat{P}_R P_R P_t^*$

$I_R \gg I_t$

FIGURE 2-7. Conceptual diagram of the wavefront reconstruction (holographic) imaging method in optics.

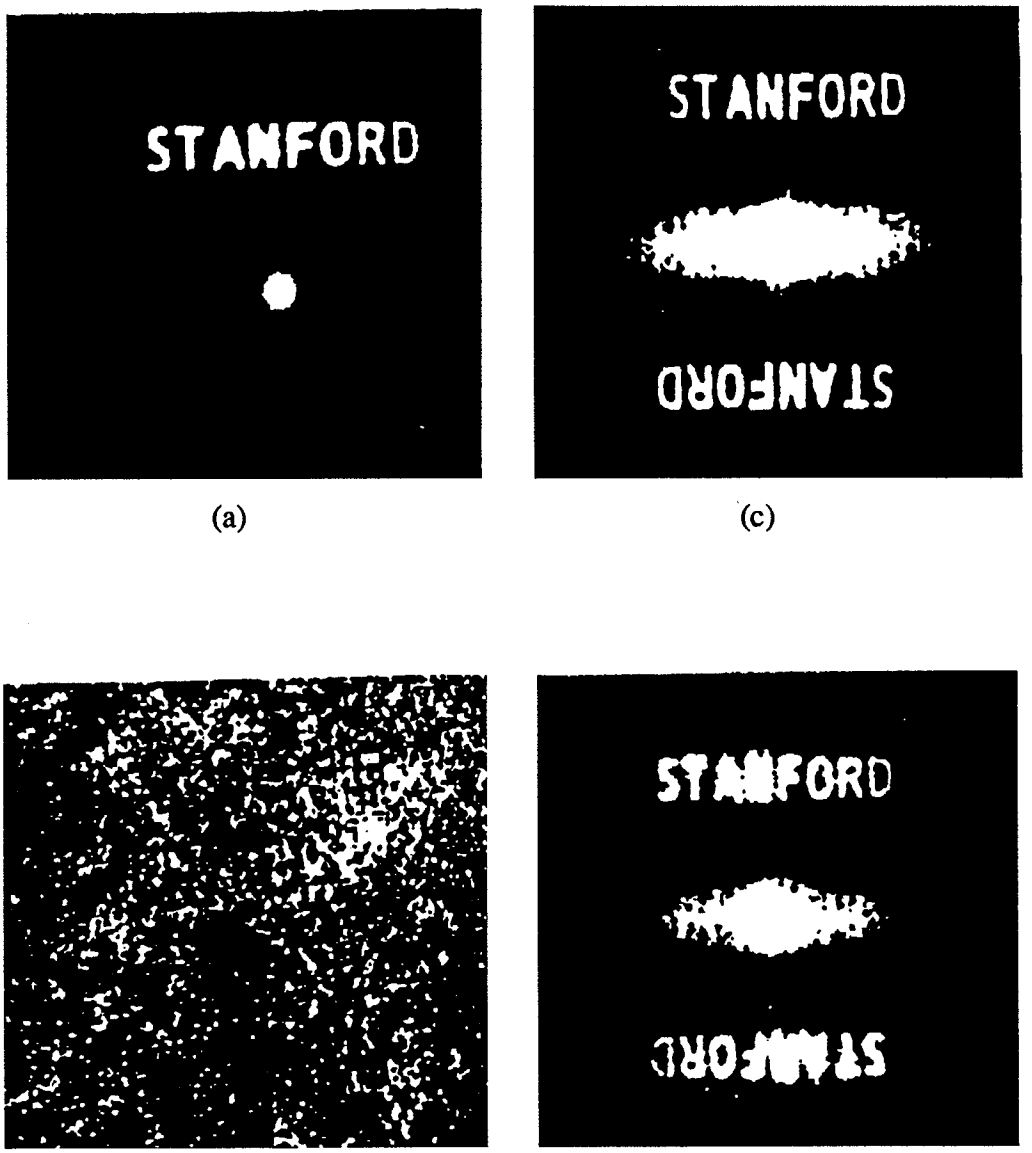

FIGURE 2-8. The effect of random media on the resolution of imaging systems; (a) conventional imaging with no random medium present, (b) conventional imaging in the presence of random medium between the object and the film, (c) wavefront reconstruction method with no random medium present, (d) wavefront reconstruction method with random medium present between the object and the hologram.

2-3.2 Holography in the Ocean

The optical technique for wavefront reconstruction is not directly applicable to long range propagation in the ocean, because the sound speed profile, Fig. 1-3, varies significantly with depth. Sound is refracted along several paths between the source and the receiver. In the ocean, the received field is the sum of fields over all paths

$$P_R = \sum_i P_R(i) \tag{2-7}$$

for the reference source, and

$$P_t = \sum_j P_t(j) \tag{2-8}$$

for the object, or target, source; i and j are the path numbers. The cross term in the holographic intensity is

$$P^*_R P_t = \sum_i \sum_j P^*_R(i)\, P_t(j) \tag{2-9}$$

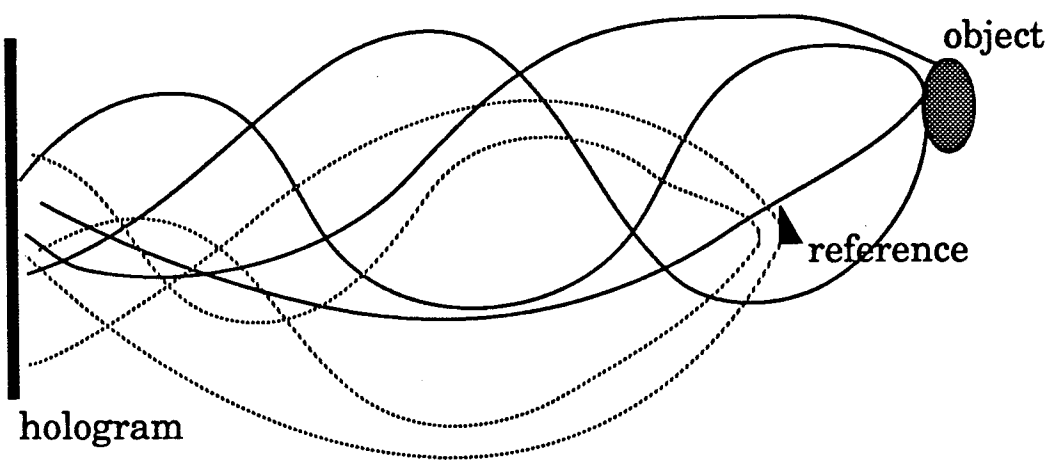

FIGURE 2-9. One reference cannot compensate for phase perturbation along all paths.

Only the cross terms for which the object and reference waves travel the same paths, i=j, will benefit from the reduction of the phase perturbation due to the random media. Since sound propagates to long distances in the ocean over many paths and since each of these paths is distorted in a different way, a different phase correction must be provided for each path. This can be accomplished by the use of multiple reference sources deployed at the same range, but distributed in depth.

We shall show that the appropriate holographic combiner is given by the operation

$$H(z_R) = \int_{hologram} P^*_R(z, z_R) P_t(z)\, dz \tag{2-10}$$

where z is the position along the receiving array (hologram), and z_R is the depth of the associated reference source.

2-3.3 Wave Equation in a Range Dependent Ocean

The acoustic pressure P in the ocean is a solution of the Helmholtz equation,

$$\nabla^2 P + \frac{\omega^2}{c^2} P = 0 \quad , \tag{2-11}$$

with the appropriate boundary conditions, acoustic frequency ω, and sound speed c. Consider the solution when the depth is uniform, the medium is range independent, the acoustic characteristics of the sea bottom do not change with range, and the sound speed is a function of depth only, c=c(z). The solution to the Helmholtz equation is easily obtained [12] by the method of separation of variables

$$P(r, z) = H_0^{(1)}(\xi r)\, \psi(z) \tag{2-12}$$

where $H_0^{(1)}(\xi r)$ is the Hankel function of the first kind zero order (represents the range dependent part of an outgoing wave); for large argument, $\xi r \gg 1$, it has the asymptotic form:

$$H_0^{(1)}(\xi r) = \sqrt{\frac{2}{\pi \xi r}} exp\left[i(\xi r - \frac{\pi}{4}) \right] \tag{2-13}$$

where ξ is the separation constant. The depth function satisfies the wave equation

$$\frac{d^2}{dz^2}\psi(z) + [k^2(z) - \xi^2]\psi(z) = 0 \tag{2-14}$$

and the boundary conditions

$$P(r, 0) = 0 \qquad \text{pressure release surface}$$

$$\left(\frac{\partial}{\partial z} P\right)\Big|_{z=h} = 0 \quad \text{rigid bottom}$$

Representing the solution as the sum of normal modes, we get

$$P(r, z) = i\pi \sum_m \psi_m(z_s)\psi_m(z) H_0^{(1)}(\xi_m r) \tag{2-15}$$

where $\psi_m(z)$ are orthonormal eigenfunctions, and ξ_m are horizontal wavenumbers (eigennumbers).

We are concerned about the generalization of this theory to the case when the characteristics of the ocean acoustic waveguide vary with range. Important cases include:

- when sound propagates in the coastal wedge, where variation of sea depth is significant,
- when sound waves cross frontal zones in the ocean, such as currents, gulf stream, cold or hot eddies, Kuroshio, etc.,
- when sound propagates over large ranges of the order of thousands of kilometers.

2-3.3.1 The Reference Waveguide Method

To solve the Helmholtz equation for a range and depth dependent medium, c=c(r,z), we will use a reference waveguide at fixed r=r_1 where c=c(r_1,z). Note that the depth depends on r, $h = h(r)$, but the reference waveguide corresponding to the range r_1 has a horizontal bottom at depth $h = h(r_1)$.

For the reference waveguide at an arbitrary r, there is a total system of orthogonal eigenfunctions [13], $\psi_m(r,z)$, m=1,2,..., depending on z (r is taken as a parameter) and satisfying the equation

$$\frac{d^2}{dz^2}\psi_m(r,z) + [k^2(r,z) - \xi_m^2]\psi_m(r,z) = 0 \tag{2-16}$$

and the boundary conditions at the surface and the bottom. Here $\xi_m=\xi_m(r)$ are the eigenvalues of the reference waveguide at r as illustrated in Fig. 2-10. The pressure field for a given r can be represented as an expansion in terms of the eigenfunctions

$$P(r,z) = \sum_m B_m H_0^{(1)}(\xi r)\psi_m(r,z) \tag{2-17}$$

where B_m are modal constants for a range independent stratified waveguide. Substituting $P(r,z)$ into the Helmholtz equation we get

$$\frac{\partial^2}{\partial z^2}P(r,z) = \sum_m B_m H_0^{(1)}(\xi_m r)\frac{\partial^2}{\partial z^2}\psi_m(r,z) \tag{2-18}$$

$$\nabla_r P(r,z) = \sum_m B_m H_0^{(1)}(\xi r)\nabla_r^2\psi_m + 2\nabla_r[B_m H_0^{(1)}(\xi_m r)]\nabla_r\psi_m + \psi_m\nabla_r^2[B_m H_0^{(1)}(\xi r)] \tag{2-19}$$

where $\nabla_r^2 = \frac{\partial^2}{\partial x^2} + \frac{\partial^2}{\partial y^2}$, and for brevity we omit the functional arguments.

Taking advantage of the orthonormal property of the eigenfunctions in each reference waveguide,

$$\int_0^h \psi_m(r,z)\,\psi_n(r,z)\,dz = \delta_{mn} \quad , \tag{2-20}$$

substituting Eq. (2-18) and Eq. (2-19) in Eq. (2-11), and considering Eq. (2-16) to substitute for $\frac{\partial^2}{\partial z^2}\psi_m$, and subsequent multiplication by $\psi_n(r,z)$ followed by integration over z from 0 to h, yields the following set of coupled differential equations

$$(\nabla_r^2 + \xi_n^2) B_n H_0^{(1)}(\xi_n r) = -2\sum_m \nabla_r [B_m H_0^{(1)}(\xi_m r)] \int_0^h \psi_n (\nabla_r \psi_m)\,dz - \sum_m B_m H_0^{(1)}(\xi_m r) \int_0^h \psi_n \nabla_r^2 \psi_m\,dz \tag{2-21}$$

2-3.3.2 Adiabatic Approximation

The right-hand side of Eq. (2-21) is small if the properties of the waveguide vary sufficiently slowly with horizontal range r [14]. If we assume the right-hand side is zero, then the equations for the normal modes are uncoupled. Each mode propagates in the waveguide independently of the others. This approximation, when the interaction between modes is neglected, is called the adiabatic approximation.

In cylindrical coordinates $\nabla_r^2 = \frac{1}{r}\frac{\partial}{\partial r}(r\frac{\partial}{\partial r})$, then the adiabatic approximation of the wave equation is

$$\frac{1}{r}\frac{\partial}{\partial r}(r\frac{\partial}{\partial r}\Phi_m(r)) + \xi_m^2(r)\,\Phi_m(r) = 0 \tag{2-22}$$

where we use

$$\Phi_m(r) = B_m H_0^{(1)}(\xi_m r) \tag{2-22}a$$

If we let

$$F_m(r) = r^{1/2}\Phi_m(r) \quad , \tag{2-22)b}$$

then substituting in Eq. (2-22), and neglecting the terms with $1/r^2$ when solving for the far field, $\xi_m r \gg 1$, we get

$$\frac{d^2}{dr^2}F_m(r) = -\xi_m^2(r)F_m(r) \quad . \tag{2-23}$$

If the eigennumbers were range independent, $\xi(r)=\xi$, then Eq. (2-23) has the solution

$$F(r) = A\exp[\pm i\xi r] \tag{2-24}$$

where A is a constant of integration, to be found from the boundary conditions.

Dividing the range of interest into intervals and assuming that ξ is constant in each interval, Fig. 2-10, and matching the solution at the boundaries of the neighboring intervals, then we get

$$F(r_0, r) = Ae^{i\xi(r_0)(r-r_0)} \tag{2-25}$$

where $r_0 \le r < r_1$

$$F(r_1, r) = A_1 e^{i\xi(r_1)(r-r_1)} \tag{2-26}$$

where $r_1 \le r < r_2$, and by matching the solutions at r_1, we get

$$A_1 = Ae^{i\xi(r_0)(r_1-r_0)} = Ae^{i\xi(r_0)\Delta_0} \quad ,$$

and in general for $r_l \le r < r_{l+1}$ we have

$$A_l = Ae^{i\xi(r_0)\Delta_0 + i\xi(r_1)\Delta_1 + \ldots + i\xi(r_{l-1})\Delta_{l-1}} \tag{2-27}$$

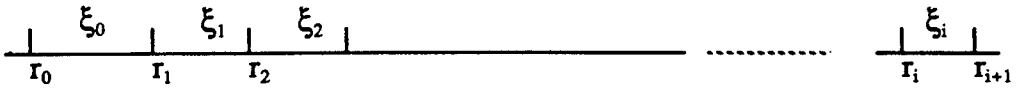

FIGURE 2-10. Dividing the range between the source and receiver into N incremental intervals, and the eigennumber within each interval is constant. Here we assumed that the source is at range r_0.

Letting the range increments be infinitesimally small, the summation is equivalent to integration, and the range dependent function becomes

$$F_m(r) = A_m exp\left[\int_{r_0}^{r} \xi_m(\tilde{r})\, d\tilde{r}\right] . \tag{2-28}$$

Taking into account all normal modes, the pressure field is

$$P(r,z) = \sum_m A_m \psi_m(r,z)\, r^{-1/2} exp\left[-i\int_{r_0}^{r} \xi_m(\tilde{r})\, d\tilde{r}\right] . \tag{2-29}$$

For a stratified, horizontally homogeneous waveguide, under the assumption that $\xi_m r \gg 1$ where the asymptotic form for the Hankel function can be used, the pressure field in Eq. (2-15) becomes

$$P(r,z) = \left(\frac{2}{\pi}\right)^{1/2} e^{-i(\pi/4)} \sum_m \psi_m(z)\, \psi_m(z_s)\, (\xi_m r)^{-1/2} \cdot exp\,[i\xi_m r] . \tag{2-30}$$

At relatively small ranges r from the source (but large compared with the wavelength) the variation of the medium properties in the horizontal does not affect the sound field, and ξ_m can be considered constant. Thus, for these ranges Eqs. (2-29) and (2-30) must be identical. This will yield

$$A_m = \left(\frac{2}{\pi}\right)^{1/2} e^{-i(\pi/4)} \psi_m(0, z_s)\, \xi_m^{-1/2} \quad . \tag{2-31}$$

Then the acoustic pressure for a range dependent ocean is

$$P(r, z) = \left(\frac{2}{\pi r}\right)^{1/2} e^{-i(\pi/4)} \sum_m \psi_m(0, z_s)\, \psi_m(r, z)\, [\xi_m(r)]^{-1/2} \cdot exp\left[-i \int_{r_0}^{r} \xi_m(\tilde{r})\, d\tilde{r}\right] \tag{2-32}$$

where $\psi_m(0, z_s)$ is the vertical eigenfunction in the region close to the source and $\xi_m(r)$ is the eigenvalue of the depth equation $\psi_m(z,r)$ for the reference waveguide corresponding to a given r.

2-3.4 Reconstruction of the scattered field at the virtual array

Without loss of generality we adopt a cylindrically symmetric model of the ocean, Fig. 2-11, where the axis of symmetry is at r_0. The sound speed varies with depth and range, c(z,r). The receiving array is at coordinate (z_i,r_0) where z_i denotes the depth of the individual hydrophones. The unknown object, at position (z_t,r_t), produces the scattered field when illuminated by the reference source, or when it radiates independently. The reference source is shown at position (r_R,z_R). While the following theory is presented with the assumption that $r_R<r_t$, we note where appropriate the minor change required for the case $r_R>r_t$.

Synthetic multiple reference sources can be generated by periodically lowering a reference source at the reference range r_R and allowing it to transmit at each incremental depth, Fig. 2-11. This way we create a virtual array of multiple references distributed over the water column.

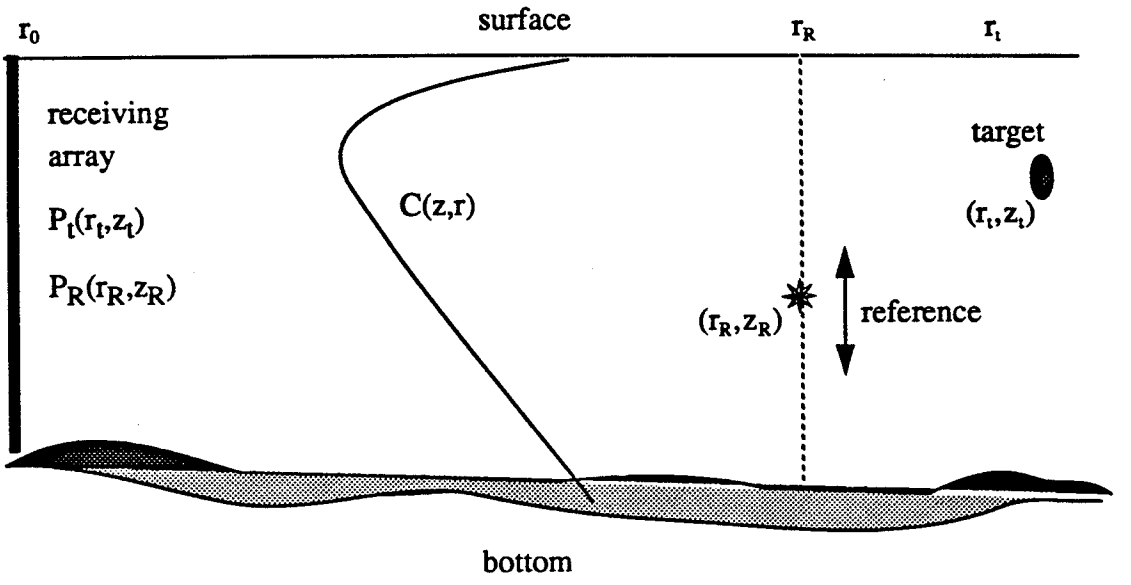

FIGURE 2-11. A vertical slice of a cylindrically symmetric ocean model, with a reference source deployed near the target to an array of depths.

2-3.4.1 Generating the Holographic Image of the Scattered Field

A holographic image of the scattered field from the target can be generated by combining the measured pressure field from the target with that from each and every reference source, and then averaging over all the hydrophones of the receiving array. We use normal mode theory in a slowly varying, horizontally stratified ocean to show that this process corrects for the variability of the medium.

Assuming that we can separately identify the arrival of the reference source and target signals at the receiving array, then the pressure field from the target on the i^{th} receiving hydrophone is

$$P_t(r_0, z_i) = \left(\frac{2}{\pi}\right)^{1/2} e^{-i(\pi/4)} \sum_m \psi_m(r_0, z_i)\, \psi_m(r_t, z_t)\, [r_t \xi_m(r_t)]^{-1/2} \cdot \exp\left[-i \int_{r_0}^{r_t} \xi_m(r)\, dr\right] \tag{2-33}$$

and that from a reference source at depth z_R is

$$P_R(r_0, z_i) = \left(\frac{2}{\pi}\right)^{1/2} e^{-i(\pi/4)} \sum_m \psi_m(r_0, z_s)\, \psi_m(r_R, z_R)\, [r_R \xi_m(r_R)]^{-1/2} \cdot \exp\left[-i \int_{r_0}^{r_R} \xi_m(r)\, dr\right] \tag{2-34}$$

The real functions $\psi_m(r,z)$ are the z-dependent discrete, or 'propagating' eigenfunctions for the 'reference waveguide problem' at position r, and $\xi_m(r)$ are their real eigenvalues. Although the continuous spectrum, which fills out the orthonormal basis set, can in general make a contribution with complex ψ_m, these evanescent modes are significant only in the immediate region near the source, for ranges that satisfy the inequality $kr \leq 1$, where k is the acoustic wavenumber.

The accumulated phase of a mode propagating between two points is given by the integral of the eigenvalue over the range between the two points, as indicated in the exponents of Eqs. (2-33) and (2-34). The structure of these equations reflects the relative positions of the source and receiver. One set of eigenfunctions, ψ_m, in each sum depends on the location of the receivers, while the other set depends on the location of the target or reference source.*

The holographic image 'filter', H, can be constructed by combining the pressure from the target and the references

$$H(r_t, z_t; r_R, z_R) = \int_0^h P_t(r_t, z_t; r_0, \tilde{z})\, P_R^*(r_R, z_R; r_0, \tilde{z})\, d\tilde{z} \quad . \tag{2-35}$$

Taking advantage of the orthonormality of the eigenfunctions of the reference waveguide at $r = r_0$, Eq. (2-20), the double sum over two different sets of modes will be reduced to a single sum, and the modal representation of the holographic image becomes

$$H(z_R) = \frac{2}{\pi\sqrt{(r_t r_R)}} \sum_m \frac{\psi_m(r_t, z_t)\,\psi_m(r_R, z_R)}{\sqrt{\xi_m(r_R)\,\xi_m(r_t)}} exp\left[-i\int_{r_R}^{r_t} \xi_m(r)\,dr\right] \quad . \quad (2\text{-}36)$$

H, the holographic image, can be viewed as a weighted version of P_t along the virtual array. In contrast with the recording step in optical holography, where we record the total intensity $|P_T|^2$, here we record $P_R^*(P_T - P_R)$, where $P_T = P_R + P_t$ is the total field from the object and the reference source.

H contains eigenfunctions calculated from a reference waveguide problem at ranges r_R and r_t. Also, it has the same phase as a field propagating from a source at r_t and received at r_R, the reference locations. This field is

$$P_t(r_R, z_R; r_t, z_t) = \left(\frac{2}{\pi}\right)^{1/2} e^{-i(\pi/4)} \sum_m \psi_m(r_R, z_R)\,\psi_m(r_t, z_t)\,[|r_t - r_R|\xi_m(r_t)]^{-1/2} \cdot \cdot \cdot \cdot exp\left[-i\int_{r_R}^{r_t} \xi_m(r)\,dr\right] \quad (2\text{-}37)$$

If the pressure field generated by the m^{th} mode is P_t^m, and the holographic image associated with the m^{th} mode is H^m, then

$$P_t^m = e^{i(\pi/4)} \left(\frac{\pi r_R r_t \xi_m(r_R)}{2|r_t - r_R|}\right)^{1/2} H^m \quad . \quad (2\text{-}38)$$

Therefore, we can write P_t, as the weighted sum of the modes of the holographic image H, i.e,

$$P_t(r_R, z_R; r_t, z_t) = e^{i(\pi/4)} \left(\frac{\pi r_R r_t}{2|r_t - r_R|} \right)^{1/2} \cdot \sum_m [\xi_m(r_R)]^{1/2} \psi_m(r_R, z_R) \int_0^{h(r_R)} H(r_R, z_R) \psi_m(r_R, z_R) \, dz_R \tag{2-39}$$

From this relation, we can see that given the holographic image at the virtual array, one can calculate the pressure field from the scatterer as if it was measured at the virtual array.

The main significance of H is that it is made up of measured data where the weighting of P_t by P_R^* filters out the effect of the oceanic variability. Furthermore, the phase of each modal component of H is the accumulated phase between the reference sources and the target. This phase is independent of the variability of the index of refraction between the source and the receiving array.

2-3.4.2 Localization Algorithm

Assume the ocean is frozen during the measurements. The localization algorithm consists of the following steps:

1. Measure the pressure field from the target along the vertically distributed receiving array, $P_t(z_i)$.
2. Deploy a reference source at range r_R and depth z_R, and allow it to transmit.
3. Measure the pressure field from the reference source. Its conjugate is $P_R^*(z_i, z_R)$.
4. Multiply the pressure from the target by the conjugate of the pressure from the reference source at each and every hydrophone of the receiving array.
5. Take the average of the previous step by adding the result of multiplication on each hydrophone and dividing by the number of hydrophones in the receiving array giving $H(z_{R1})$.
6. Deploy the reference source to a new depth and repeat step 2 through 5.
7. When all reference depths are used then we have the total holographic image, $H(z_{R1}, z_{R2}, \ldots, z_{RN})$, of the target as if it was recorded on the virtual array.
8. While deploying the reference source, we measure the SSP of the ocean at the virtual array.

9. Assume the ocean is range independent between the virtual array and the target, and it has the SSP obtained in step 8.

10. Using a propagation model, such as wide angle PE, compute the pressure field on the virtual array from a hypothetical point source at position (r´,z´) in the vicinity of the reference and target, giving $G(r_R, z_R; r', z')$, the spatial impulse response between the hypothetical location and the virtual array.

11. Multiply the pressure from the hypothetical position, G, by the conjugate of the hologram H, and average over all elements of the virtual array giving the reconstructed field.

$$Q(r', z') = \int_0^{h_{VA}} G(r_R, z_R; r', z')\, H^*(r_R, z_R; r_t, z_t)\, dz_R \qquad (2\text{-}40)$$

12. Repeat the steps 10 through 11 exhausting all possible candidate locations of the target, yielding a matrix of Q in range and depth.

13. The source location is where the magnitude of Q attains a maximum, then $(r', z') \Rightarrow (r_t, z_t)$.

The above steps can be summarized in a block diagram format, as shown in Figs. 2-12 and 2-13, where Fig. 2-12 shows a simplified block diagram for the holographic array processing algorithm, and Fig. 2-13 shows a more detailed block diagram for the HAP algorithm. In Fig. 2-13 we assumed N receivers and M reference sources. The STD is an instrument that measures salinity, temperature, and depth; this data can be used to calculate the sound speed profile at the virtual array, as described in chapter 1.

The HAP method assumes no communication link between the reference and the receiver, and the data processing takes place at the receiving site. In this case, the collected STD data will be useful only for updating the oceanographic data-base for that region for future implementation.

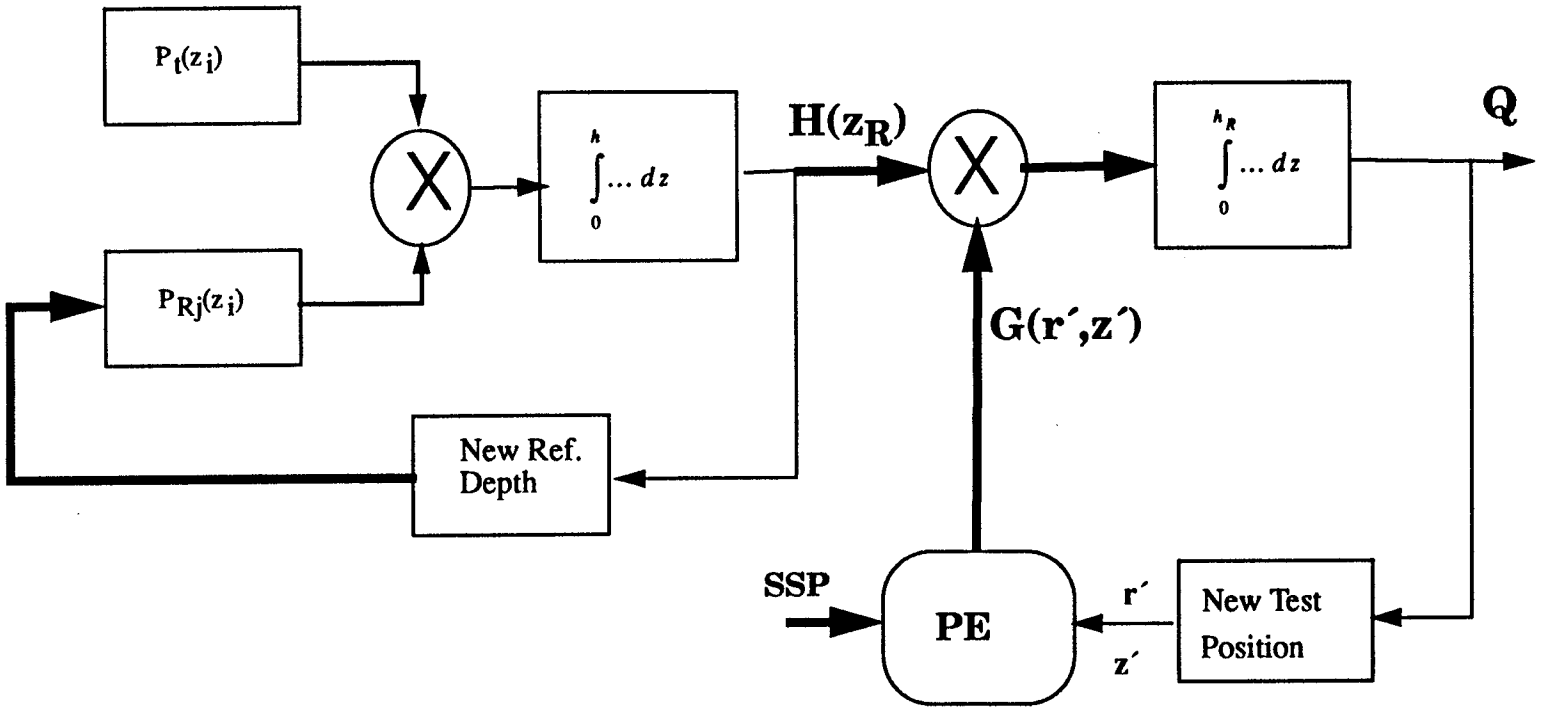

FIGURE 2-12. Simplified block diagram for the holographic array processing (HAP) algorithm.

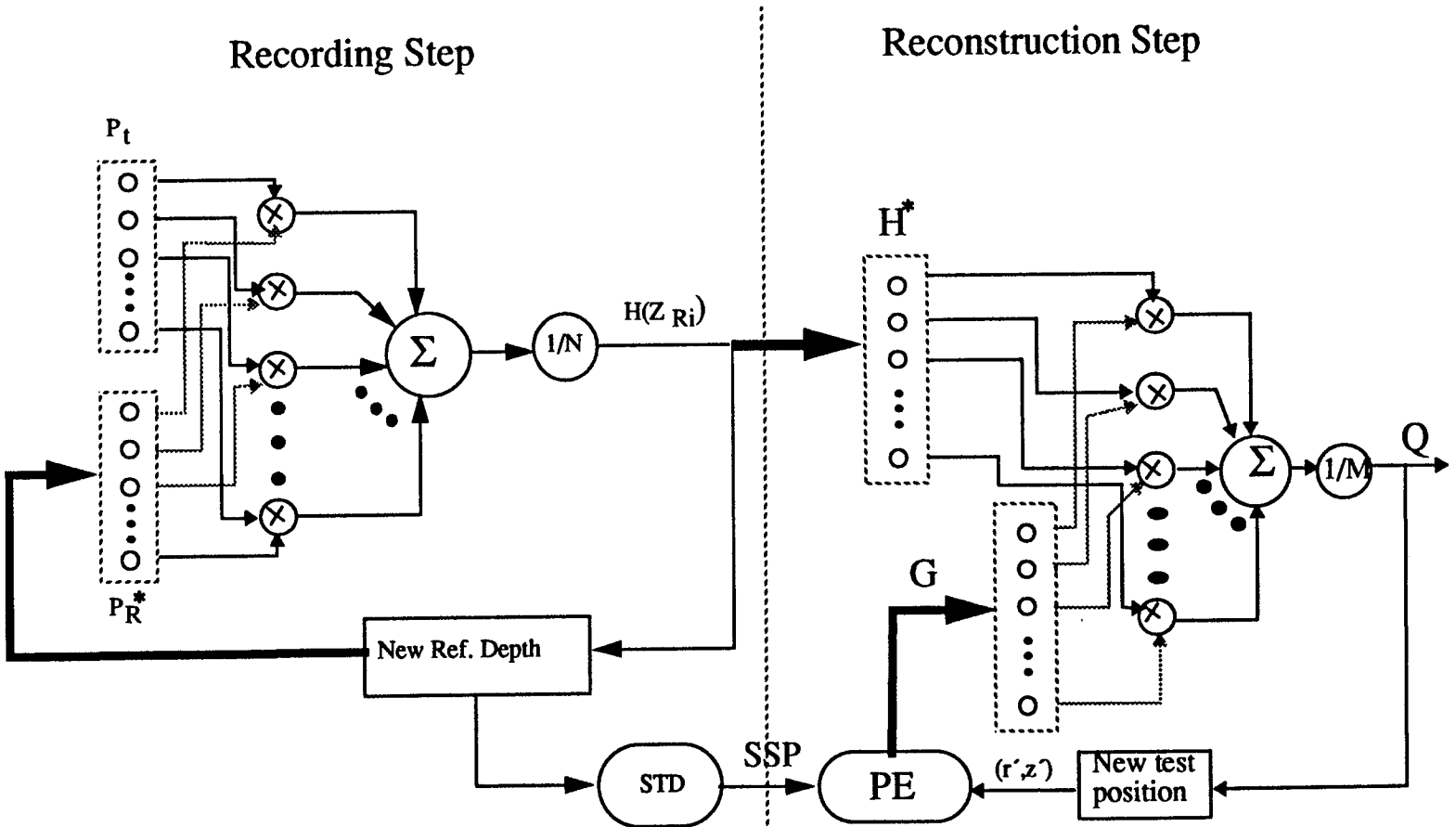

FIGURE 2-13. Detailed block diagram for the HAP algorithm.

2-3.4.3 Focusing Criterion

In our simulation we assumed that the ocean is range independent between the target and the reference array. The estimated eigennumbers $\hat{\xi}_m$ and eigenfunctions $\hat{\psi}_m$ are those of the reference waveguide at the virtual array. Then the pressure field from a test source at location (r´,z´), as calculated at the virtual array, is

$$G(r_R, z_R; r', z') = \left(\frac{2i}{|r' - r_R|\pi}\right)^{1/2} \sum_m \frac{\psi_m(r_R, z_R)\,\hat{\psi}_m(r', z')}{\sqrt{\hat{\xi}_m(r')}} exp\left[-i\int_{r_R}^{r'} \hat{\xi}(r)\,dr\right] \quad . \quad (2\text{-}41)$$

Here we assumed that $r_R < r'$, although a change in sign in the exponential would describe the case where $r_R > r'$.

Since H is an approximation to the field from the target on the virtual array, and G constitutes an approximation to the spatial impulse response (Green's function) of the medium between the target and the virtual array, backpropagating H through this medium, it focuses on the location of the target. Representing Q in the normal mode formalism we get,

$$Q(r', z') = \frac{1}{\sqrt{r_R r_t |r' - r_R|}} \left(\frac{2i}{\pi}\right)^{3/2} \sum_m \frac{\psi_m(r_t, z_t)\,\hat{\psi}_m(r', z')}{\sqrt{\xi_m(r_t)\,\xi_m(r_R)\,\xi_m(r')}} \cdot exp\left[i\int_{r_R}^{r_t} \xi_m(r)\,dr - i\int_{r_R}^{r'} \hat{\xi}_m(r)\,dr\right] \quad . \quad (2\text{-}42)$$

A normalized version of Q is

$$Q_N(r', z') = \sqrt{r_R r_t |r' - r_R|}\left(\frac{2i}{\pi}\right)^{-3/2} Q(r', z') \quad . \quad (2\text{-}43)$$

By assuming that the ocean is range independent on the scale of the separation between the reference and the target, in the region of the source, we can write

$c(z, r_R) \approx c(z, r') \approx c(z, r_t)$. Hence $\psi_m(r', z) \approx \psi_m(r_t, z) \approx \psi_m(r_R, z)$, permitting the weak approximation

$$\lim_{z' \to z_t} \psi_m(r_t, z_t)\, \psi_m(r', z') \approx \lim_{z' \to z_t} \psi_m(r_R, z_t)\, \psi_m(r_R, z') = \psi_m^2(r_R, z_t) \geq 0 \quad . \quad (2\text{-}44)$$

In the limit $z' \to z_t$, $Q_N(r',z')$ reaches a maximal value, since it starts as a sum of terms of varying sign and becomes a sum of positive numbers. By identifying z' and r' which maximize Q_N, we have located a candidate position of the unknown source, without knowing the oceanic variability between the receiving and virtual arrays.

This algorithm eliminates the need to simulate the index of refraction, except in the region of the reference array. Ocean simulation is reduced from basin scales to scales characteristic of the neighborhood of the sources.

CHAPTER 3

Performance Analysis of the Holographic Array Processor

In the following we provide a performance analysis of the Holographic Array Processing (HAP) algorithm in a range dependent ocean. For this purpose, we consider three models of the ocean:

- A hypothetical ocean with range dependent N^2-bilinear Sound Speed Profiles (SSPs).
- A hypothetical ocean with range dependent exponentially stratified (Munk) SSPs.
- A realistic ocean with SSPs from the North Pacific experimental data.

3-1 Theoretical Analysis

This analysis is done for a range dependent ocean with N^2-bilinear SSP which is analytically attractive and representative of a wide variety of regions in the ocean. If the estimated horizontal wavenumber $\hat{\xi}_m(r)$ is very close to the actual $\xi_m(r)$ in the scanning region (between the target and the virtual array), then the phase term in the expression of Q_N

$$\eta_m = \int_{r_R}^{r_t} \xi_m(r)\,dr - \int_{r_R}^{r'} \hat{\xi}_m(r)\,dr \tag{3-1}$$

will be close to zero for all modes as r' approaches r_t, and the summation in Eq. (2-42) includes only positive quantities. Then, Q_N will attain a local maximum, identifying a candidate for the location of the unknown source. Uncertainty of the estimated parameters, for the ocean between the reference array and the target, will lead to source localization errors. The phase, which is a function of the horizontal wavenumber, provides information about the focus in range, while the amplitude (vertical mode functions) provides information about the focus in depth. The following analysis will be centered on the focus error in range. Therefore, we need explicit expressions for the estimated and exact eigennumbers, $\hat{\xi}_m(r)$ and $\xi_m(r)$, pertaining to the scanning region between the target and reference source.

For a range-dependent ocean, the index of refraction varies with distance and depth. We normalize the index of refraction by a reference sound speed. For convenience, the reference sound speed is assumed to be c_{a0}, the sound speed at range r=0 and depth $z=z_a$, where z_a is the depth of the channel axis. Thus

$$N(z,r) = \frac{C_{a0}}{C(z,r)} \tag{3-2}$$

is the normalized index of refraction. Also, we assume that the sound speed at the axis varies linearly with range,

$$c_a(r) = c_{a0} + Sr \tag{3-3}$$

where S is the rate of variation, and is measured in [(m/sec)/100 km].

Consider the following model for the index of refraction N (see Fig. 3-1):

- The vertex of the profile is fixed at depth z_a for all ranges,
- the depth of the ocean z_l is constant,
- the sound speed at the surface and the bottom of the ocean is constant and is c_u and c_l respectively,
- we assume that $c_u = c_l$,
- the N^2-bilinear SSP is

$$N^2(z,r) = N^2(z_a,r) + S_{u(lo)}(z - z_a) \tag{3-4}$$

where $S_{u(lo)}$ is the slope of the upper or lower portion of the N^2-bilinear profile,

$$S_u(r) = -\frac{1}{z_a}\left[\left(\frac{c_{a0}}{c_u}\right)^2 - \left(\frac{c_{a0}}{c_a(r)}\right)^2\right] \tag{3-5}$$

$$S_{lo}(r) = \frac{1}{(z_l - z_a)}\left[\left(\frac{c_{a0}}{c_{lo}}\right)^2 - \left(\frac{c_{a0}}{c_a(r)}\right)^2\right] \quad . \tag{3-6}$$

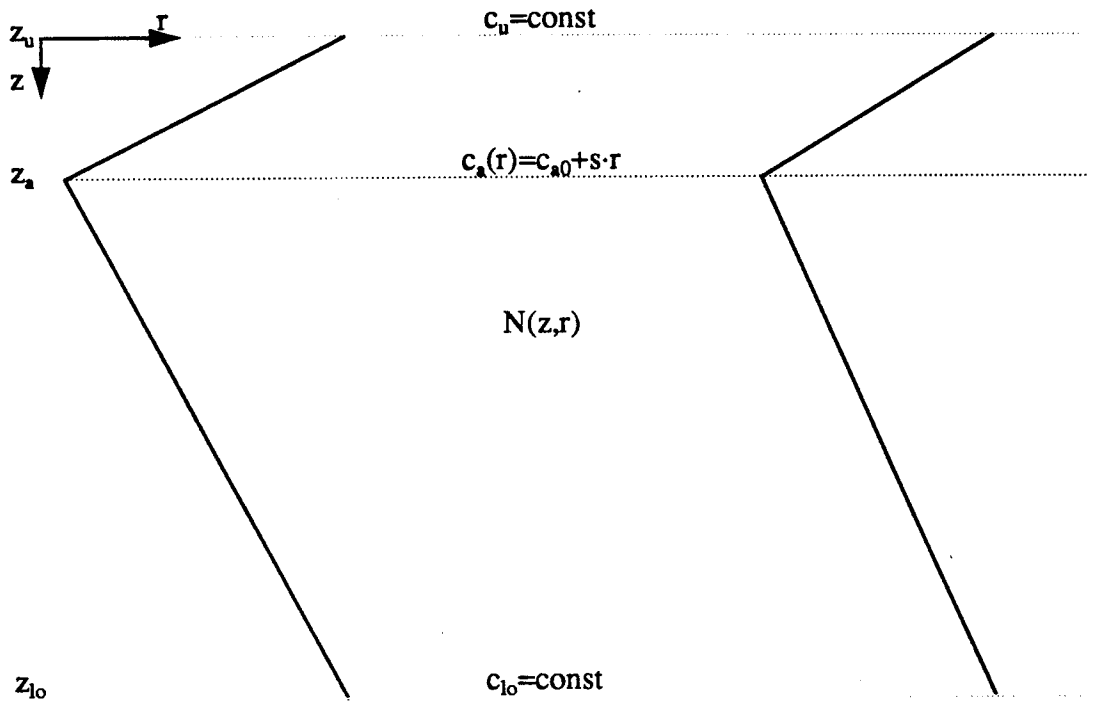

FIGURE 3-1. Model of the ocean with range dependent N^2-bilinear SSP.

We use the WKB approximation, which is valid in the geometric-acoustic limit [15], to calculate an approximation to the eigennumbers ξ_m. Following the procedure presented in appendix I, the vertical wavenumbers have a phase accumulation of

$$\theta(z, z_{utp}) = \frac{\omega}{c_a(r)} \int_{z_{utp}}^{z} \sqrt{\left(\frac{N(z,r)}{N(z_a,r)}\right)^2 - \cos^2\varphi_m}\, dz \tag{3-7}$$

resulting from the upward and downward traveling waves. Since these waves are

out of phase by $\pi/2$ radians upon reflection from the turning points, the resonance condition that isolates the eigenmodes is

$$\theta\,(z_{utp}, z_{ltp}) \;=\; (m+\tfrac{1}{2})\,\pi \tag{3-8}$$

where z_{utp} and z_{ltp} are the upper and lower turning points respectively for each mode. Their dependence on the mode number (m) is suppressed in this notation. These turning points can be found by setting the integrand in Eq. (3-7) to zero which is equivalent to defining the turning points where the vertical wavenumber (γ_m) vanishes; see Fig. 3-2. For the N^2-bilinear profile, we substitute Eq. (3-4) in the integrand of Eq. (3-7) and equate to zero. After some mathematical manipulation, we get

$$z_{ut} \;=\; z_a - z_a N^2\,(z_a, r)\,C\,(r)\,\sin^2\,[\varphi_m\,(r)\,] \tag{3-9}$$

$$z_{lt} \;=\; z_a + (z_l - z_a)\,N^2\,(z_a, r)\,C\,(r)\,\sin^2\,[\varphi_m\,(r)\,] \tag{3-10}$$

where

$$C\,(r) \;=\; \left[\left(\frac{c_{a0}}{c_a\,(r)}\right)^2 - \left(\frac{c_{a0}}{c_u}\right)^2\right]^{-1} . \tag{3-11}$$

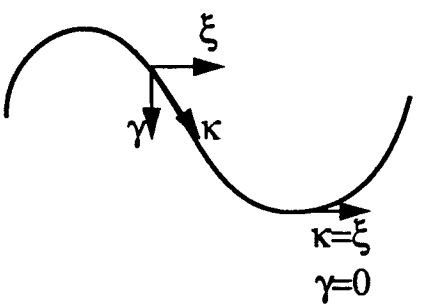

FIGURE 3-2. Variation of the vertical wavenumber between the turning points.

The range dependent mode propagation wavenumber, ξ_m, can be written as

$$\xi_m(r) = \frac{\omega}{c_a(r)} \cos\varphi_m(r) \tag{3-12}$$

where $\varphi_m(r)$ is the range dependent ray exit angle associated with the mode m. Substituting Eq. (3-8) into Eq. (3-7), we get

$$(m+\frac{1}{2})\pi = \frac{\omega}{c_a(r)} \int_{z_{utp}}^{z_a} \sqrt{\left(\frac{N(z,r)}{N(z_a,r)}\right)^2 - \cos^2\varphi_m(r)}\, dz +$$

$$\frac{\omega}{c_a(r)} \int_{z_a}^{z_{ltp}} \sqrt{\left(\frac{N(z,r)}{N(z_a,r)}\right)^2 - \cos^2\varphi_m(r)}\, dz \tag{3-13}$$

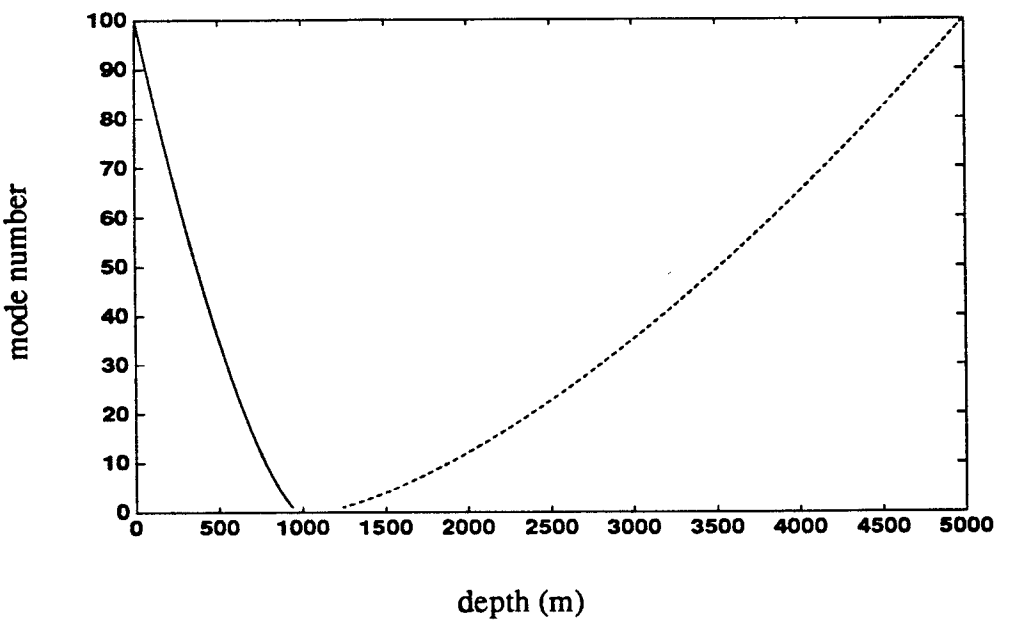

FIGURE 3-3. The upper (solid line) and lower (dotted line) turning point depths as a function of mode number.

After some mathematical manipulation, we find $\cos\varphi_m(r)$ as follows:

$$\cos^2\varphi_m(r) = 1 - \left[\frac{3}{2}(m+\frac{1}{2})\pi \frac{c_a(r)}{z_l \omega N^2(z_a, r)\, C(r)}\right]^{2/3} \tag{3-14}$$

and let

$$\alpha(m) = \left[\frac{\frac{3}{2}(m+\frac{1}{2})\pi}{z_l \omega}\right]^{2/3} \tag{3-15}$$

$$\beta(r) = \left[\frac{c_a(r)}{N^2(z_a, r)\, C(r)}\right]^{2/3} . \tag{3-16}$$

Therefore, we can write

$$\xi_m(r) = \frac{\omega}{c_a(r)} [1 - \alpha(m)\beta(r)]^{1/2} . \tag{3-17}$$

An excellent approximation to Eq. (3-17) can be derived by noting that Snell's law determines the upper limit on the ray exit angle φ_m and, therefore, on the number of propagating modes

$$\cos[\varphi_m^{max}(r)] = \frac{c_{a0}}{c(z_u, r)} = N(z_u, r) \approx 1.0. \tag{3-18}$$

Since N is close to one, φ_m^{max} is small, on the order of 13°. Applying Eq. (3-18) to Eq. (3-14) and Eq. (3-17) we conclude that

$$\alpha(m)\beta(r) \ll 1 . \tag{3-19}$$

We can expand Eq. (3-17) using the binomial series, producing

$$\xi_m(r) = \frac{\omega}{c_a(r)}\left[1-\frac{1}{2}\alpha(m)\beta(r)\right] . \tag{3-20}$$

This approximation is nearly exact (within 10^{-6}) for the ocean parameters we have considered. A linearized version of $\xi_m(r)$ in the vicinity of the virtual array is

$$\xi_m(r) = \xi_m(r_R) + \left[\frac{\partial}{\partial r}\xi_m(r)\,|_{r=r_R}\right](r-r_R) . \tag{3-21}$$

Evaluating these terms, and noting that $k_a(r) = \frac{\omega}{c(z_a, r)}$, we obtain an analytical expression for $\xi_m(r)$.

$$\xi_m(r) \approx k_a(r_R)\left[1-\frac{1}{2}\alpha(m)\beta(r_R)\right]-\frac{k_a(r_R)S}{c_a(r_R)}\bullet$$

$$\left\{1+\alpha(m)\left[\frac{1}{2}\beta(r_R)-\frac{2}{3}\left(\frac{\beta(r_R)}{c_a^2(r_R)}\right)^{-1/2}\right]\right\}(r-r_R) \tag{3-22}$$

Fig. 3-4 compares the WKB expression for the eigennumber, Eq. (3-17), with its approximation, Eq. (3-22), for different modes. From the graphs it is noticeable that the difference between the two expression is at its maximum for the highest mode number at the largest distance, and this is of the order $10^{-4}\,m^{-1}$.

In practice, one can measure $N(z, r_R)$ using a conductivity-temperature-depth (CTD) casts near the reference sources. This information is used in a wave propagation model to calculate Q_N. For our analysis, these data are used to estimate the mode propagation wavenumber, $\hat{\xi}_m(r)$, between the target and the virtual array,

$$\hat{\xi}_m(r) \approx \xi_m(r_R) . \tag{3-23}$$

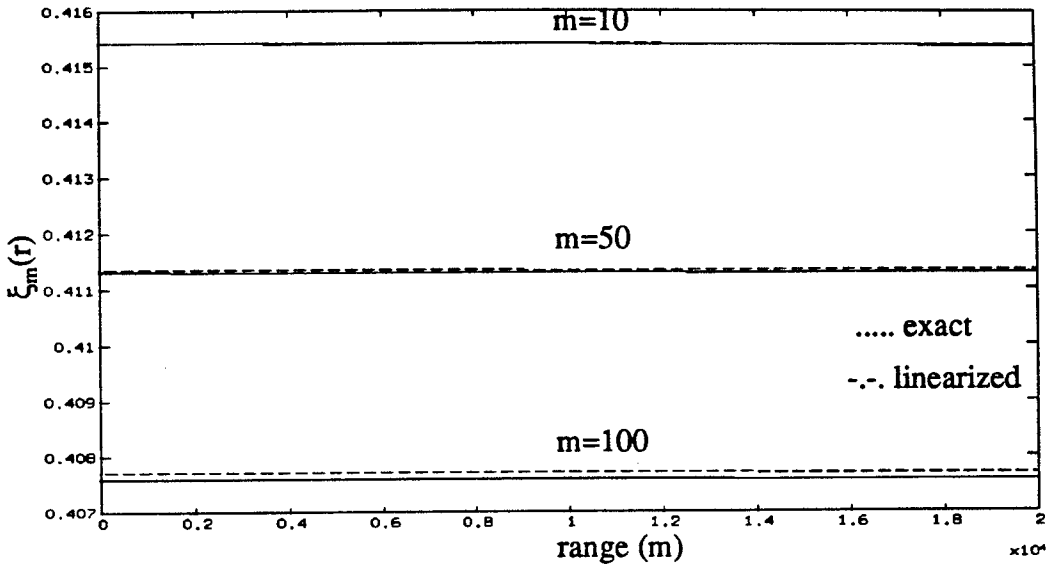

FIGURE 3-4. Comparison between the exact version of the WKB approximation to the modal eigen number and its linearized version.

When numerically evaluating the focusing condition, Eq. (3-1), we use the WKB solution, Eq. (3-17), for ξ_m. The same expression is evaluated at r_R for the estimate $\hat{\xi}_m$. When analytically evaluating Eq. (3-1) we use the linearized expression, Eq. (3-22), for ξ_m and the same expression evaluated at $r = r_R$ for the estimated $\hat{\xi}_m$. Evaluating the integrals in Eq. (3-1), we define $\Delta = r' - r_R$, $\Delta_t = r_t - r_R$, $\delta_\varepsilon = \Delta - \Delta_t$. Then we can transform the condition $\eta_m = 0$ into an expression for the focusing error (in range) of the unknown source as a function of mode number,

$$\delta_\varepsilon(m) = \frac{k_a(r_R)}{\xi_m(r_R)}\{1+\alpha(m)\left[\frac{1}{2}\beta(r_R) - \frac{2}{3}\left(\frac{\beta(r_R)}{c(z_a, r_R)}\right)^{-1/2}\right]\}\frac{S\Delta_t^2}{2} \quad . \qquad (3\text{-}24)$$

3.1.1 Discussion of the Localization Error for a Range of Physical Conditions

Figs. 3-5 through 3-8 show the dependence of the focusing error δ_ε on the mode number for an ocean with the following parameters (see Fig. 3-1): z_1=5

km, c_{a0}=1500 m/sec and c_u=c_{lo}=1540 m/sec, frequency 100 Hz, a variation of target/reference source separations, and a range of horizontal gradient in the sound speed at the sound channel axis. In all of these figures, we considered contributions from propagating modes only.

In all figures where values of the environmental parameters are chosen to represent typical range variations encountered in the ocean, the error $\delta_\varepsilon(r)$ in the estimated range of the unknown source is nearly constant with mode number. In particular, the variation in δ_ε as a function of mode number is a small fraction of the wavelength of the acoustic wave. The entire phase term η_m would only vary a fraction of a radian in these cases, and therefore, there would be a local maximum in the localization estimator Q for the predicted value of range.

It is also true that, with oceanographically motivated environmental parameters, the error in the predicted range of the unknown source is a fraction of a wavelength. For example, Fig. 3-5 shows δ_ε for Δ_t (the distance between the reference array and the unknown source) on the order of 10 and 20 km. The value of the horizontal gradient in sound speed is 10^{-5}sec^{-1}. The error quadruples as the distance between the source and the reference is doubled. However, the actual values of the error in range is still less than ten percent of the 15 m wavelength of the 100 Hz sound, and the same is true for the variation of δ_ε with mode number.

Figs. 3-6 and 3-7 show δ_ε for target-reference separation (Δ_t) of 10 and 20 km respectively, and a range of S, the horizontal gradient in sound speed, from the oceanographically motivated value of 10^{-5} to four times that value. Both cases show that the absolute range error and the variation in error with mode number are small compared with the acoustic wavelength. However, with an increase in S beyond 4×10^{-5}, the variation in range-localization error with the mode number becomes an appreciable fraction of a wavelength. With this much variation, the phase of Q may not be small enough for a substantial number of the propagating modes to add coherently. Therefore, the argument for a local maximum in Q may not apply and the algorithm may fail. Further investigation needs to be done to determine the effect of rapidly varying horizontal sound speed gradients.

Fig. 3-8 shows both numerical and analytical, Eq. (3-24), expressions for δ_ε; the target-reference separation is 20 km, and the series of the horizontal sound speed gradients is the same as in the previous plots. The difference between the analytical and numerical solutions is negligible.

In Fig. 3-9 we show the frequency dependence of the range-localization error, δ_ε, for target-reference separation of 20 km and horizontal sound speed gradient of one meter per second per 100 km. The error approaches zero as frequency decreases for a fixed mode number, because the modes cover a large fraction of a vertical slice of the water column as frequency decreases. In the waveguide that we are considering, the largest change in sound speed with range occurs near the axis of the sound channel, thereby affecting the higher-frequency localization procedure more strongly for a fixed mode number.

Fig. 3-10 shows the phase term η_m for f=100 Hz, Δ_t=20 km, and $S=10^{-5}$ sec^{-1} (a variation in the axial sound speed of 1 meter per second per 100 km). The numerical version of the integrand is used for these calculations. The values of δ_ε shown on the graph translate into different constant values for r' to be put into Eq. (3- 1) for η_m. Note that η_m varies only a fraction of a radian from 0 for the different modes. Therefore, there would be a local maximum in the localization estimator Q_N, which would indicate the predicted range.

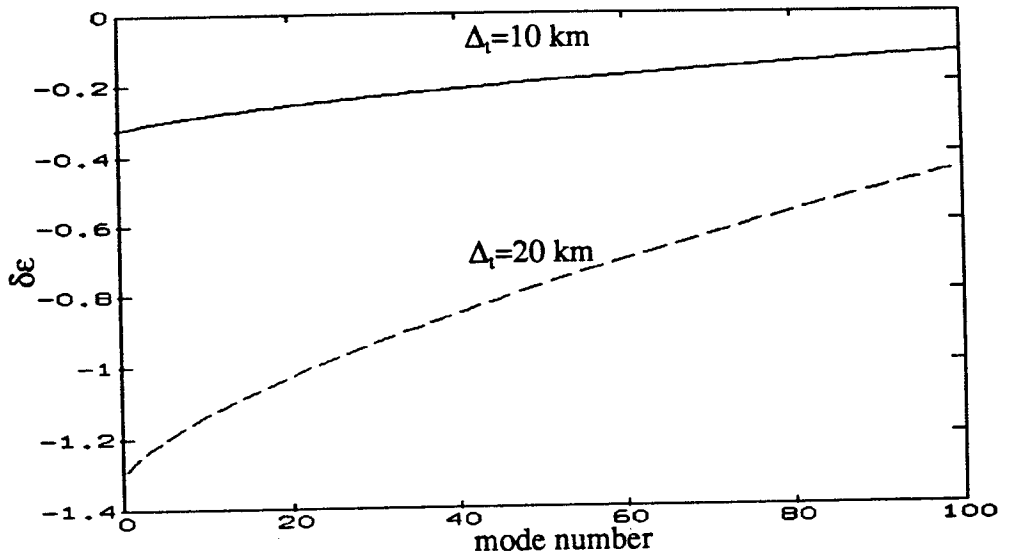

FIGURE 3-5. Focusing error δ_ε (i.e., the difference between the predicted and the actual range of the unknown source) as a function of the mode number for two values of Δ_t, the distance between the unknown source and the reference array.

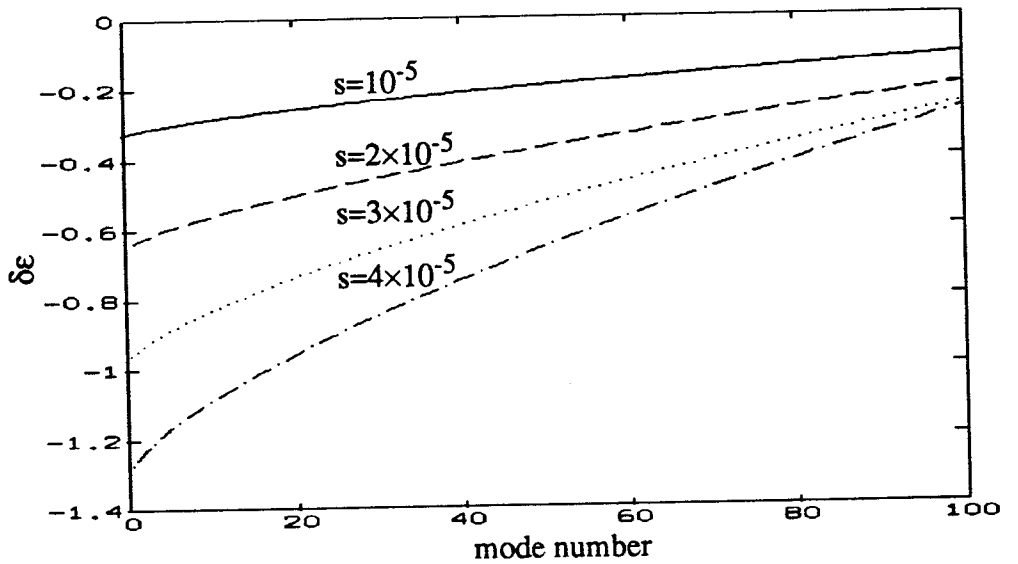

FIGURE 3-6. As in Fig. 3-5, but for Δ_t=10 km and a series of values of s, the horizontal gradients in the channel-axis sound speed.

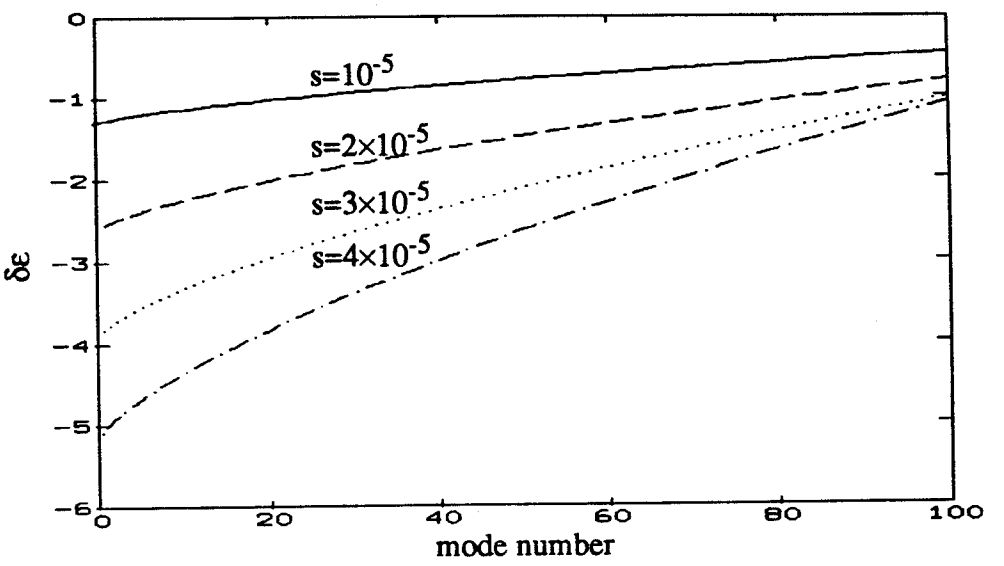

FIGURE 3-7. As in Fig. 3-6, but for Δ_t=20 km.

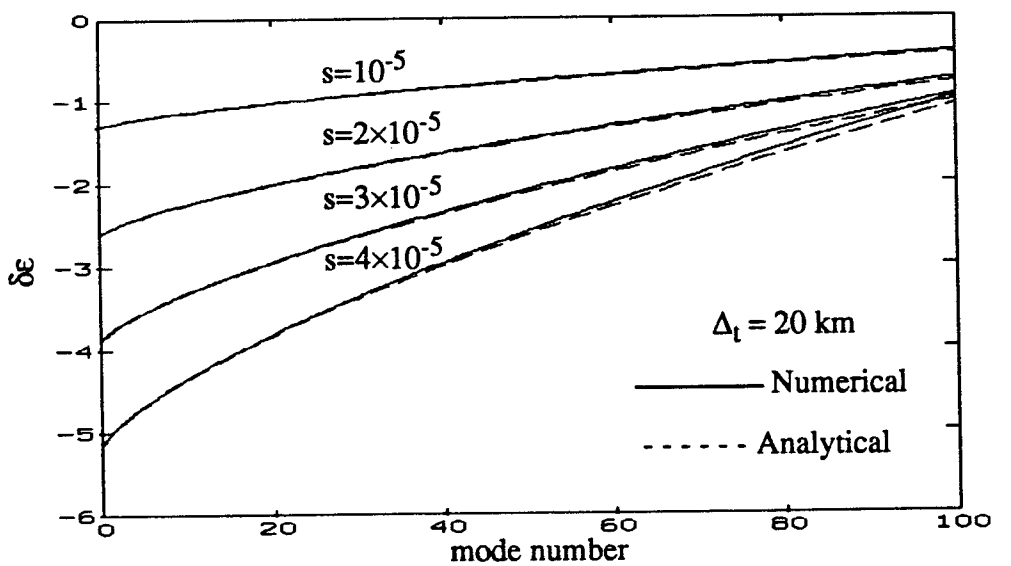

FIGURE 3-8. A comparison of the numerical integration (solid line) of the localization condition $\eta_m = 0$ with the analytical solution, Eq. (3-24).

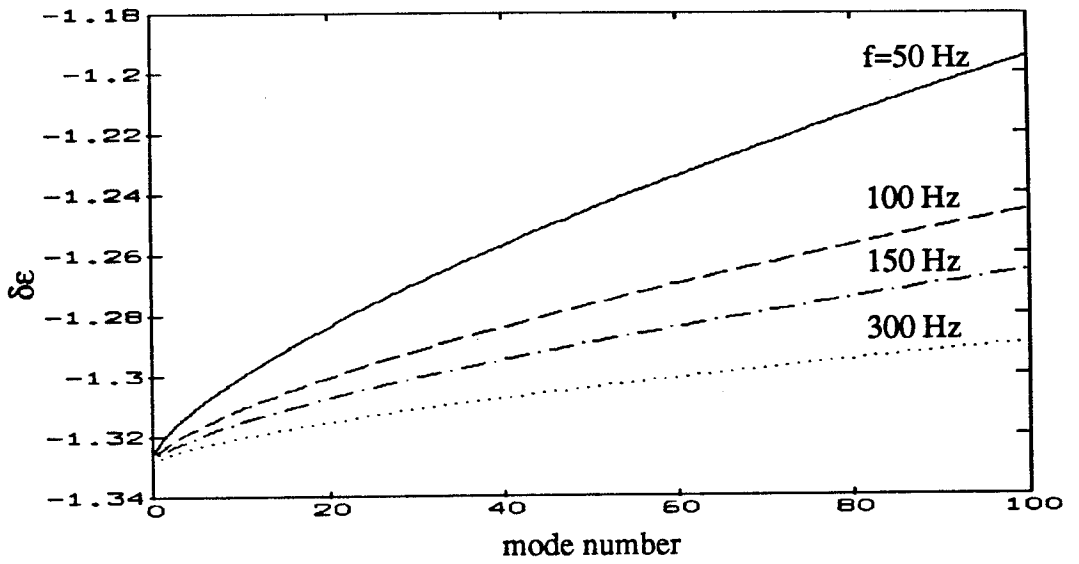

FIGURE 3-9. The frequency dependence of δ_ε as a function of mode number.

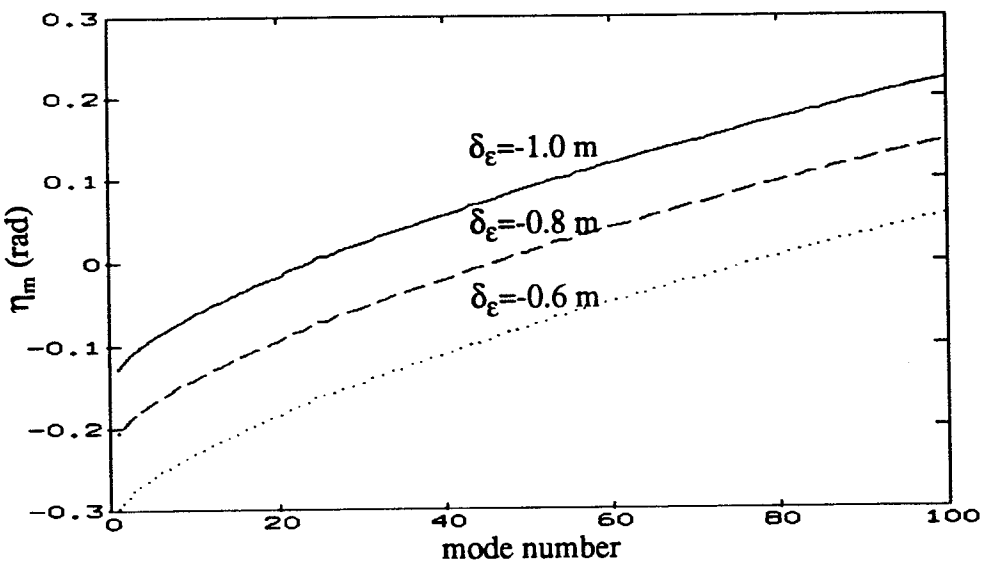

FIGURE 3-10. The phase, η_m, at different values of δ_ε as noted on the graph. This case corresponds to the curve in Fig. 3-7 for $s=10^{-5}$ sec^{-1} and Δ_t=20 km.

3-2 Numerical Simulation

Numerical simulations have been executed with range-dependent, analytical and measured, sound speed profiles. An adiabatic normal mode propagation model has been developed, and a wide angle wave propagation model, FEPE, has been modified for testing the holographic array processing algorithm. Both models produce substantial focusing at the location of the target source. The two methods reveal slight differences for the test positions (r′,z′) away from the target location (r_t,z_t). This is mainly a result of the different approximation methods used to solve the wave equation. While the adiabatic mode propagation model is numerically efficient for a slowly varying ocean, the PE model can handle more severe changes in the medium and account for mode coupling terms that are ignored by the adiabatic mode model.

3-2.1 Exponentially Stratified Sound Speed Profile

Munk [16] [17] developed a widely used mathematical expression for the SSP in the ocean,

$$c(z) = c(z_a)\,[1+\varepsilon(\nu+e^{-\nu}-1)] \tag{3-25}$$

where $\nu = \frac{2}{H_c}(z-z_a)$, z_a is the depth of the channel axis, H_c is the characteristic scale depth, and ε is a dimensionless shape parameter. Three parameters (z_a, ε, and ν) control the behavior of the Munk profile. Fig. 3-11, shows a typical exponentially stratified, Munk, SSP, where the axis depth is taken at 1000 m, H_c is 1000 and ε is 0.057.

The range dependency is introduced by assuming that the sound speed at the axis varies linearly with range,

$$c(z,r) = c(z_a, r_0) + S \cdot r \quad . \tag{3-26}$$

The profiles shown, Fig. 3-11, are separated by 500 km with $S=10^{-5}$ sec^{-1} which corresponds to a change in the axial sound speed of 1 m/sec per 100 km. The

total change, over this range, of the axial sound speed is 5 m/sec. The upper and lower turning points, Fig. 3-12, are found using the WKB approximation.

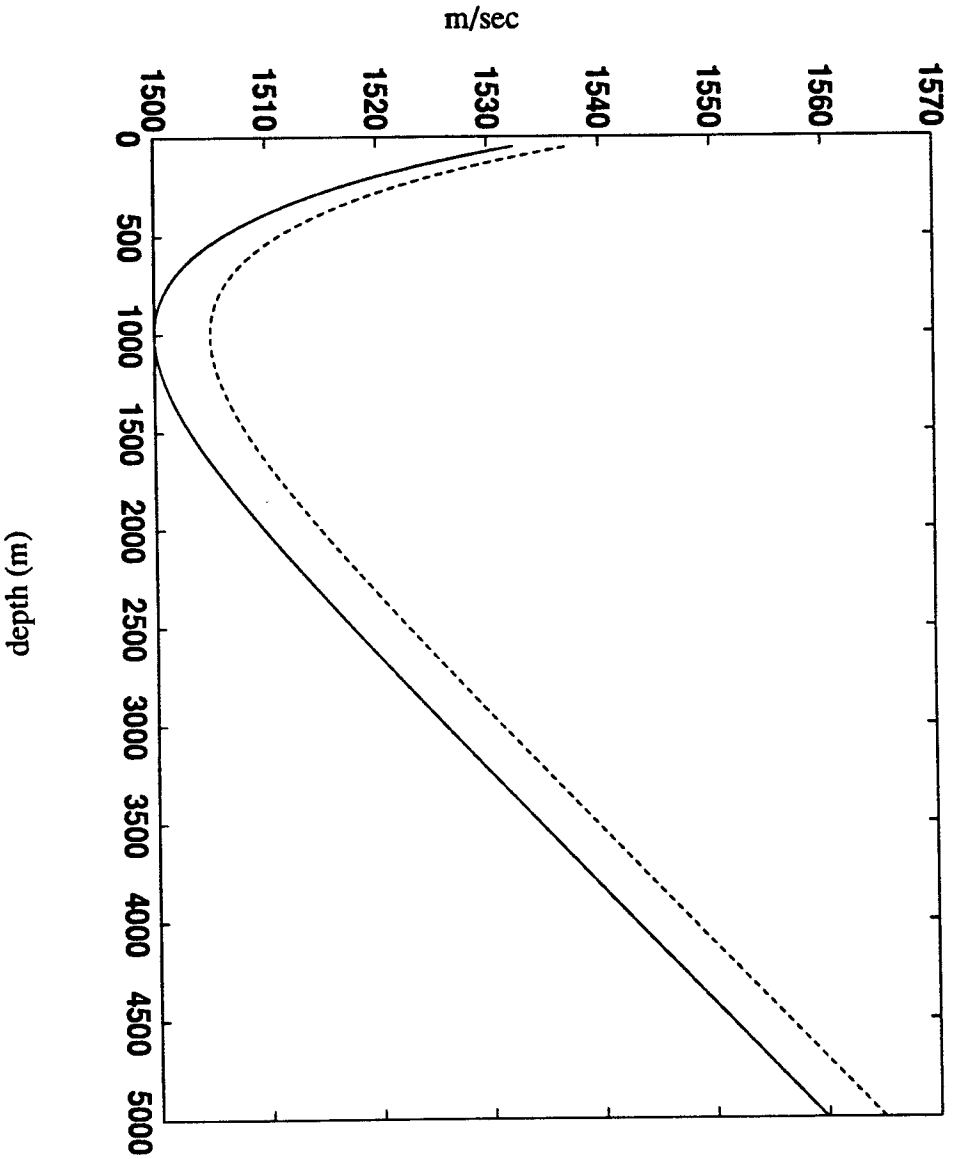

FIGURE 3-11. Range dependent exponentially stratified SSP. The solid line represents the SSP at range zero; the dashed line represents the SSP at range 500 km.

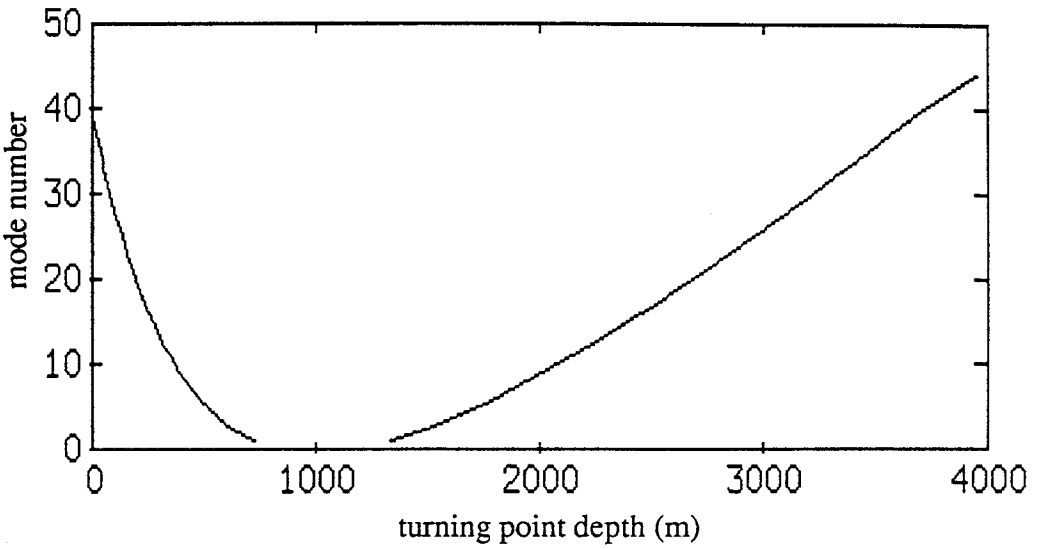

FIGURE 3-12. Upper and lower turning points for the Munk profile in Fig. 3-11 at range zero.

The depth-step at the receiving and virtual arrays is such that there is adequate sampling for all modes, especially the high order modes. The highest order mode has the largest spatial frequency and, therefore, the smallest spatial wavelength. Thus, sufficient sampling of this mode will guarantee adequate sampling for the other (lower order) modes. The largest vertical wavenumber is

$$\gamma^{max} = \frac{2\pi}{\lambda_a} \sin\theta^{max} \tag{3-27}$$

where λ_a is the acoustic wavelength and θ^{max} is the maximum exit angle (corresponds to the highest order mode). The vertical wavenumber can be written in terms of the spatial wave length (λ_s) as

$$\gamma^{max} = \frac{2\pi}{\lambda_s^{min}}. \tag{3-28}$$

Substituting Eq. (3-27) in Eq. (3-28) we get

$$\lambda_s^{min} = \frac{\lambda_a}{\sin\theta^{max}} \quad . \tag{3-29}$$

Therefore, the highest order mode will be adequately sampled if the depth-step is less than or equal to half the minimum spatial wavelength, Eq. (3-29).

Figs. 3-13 and 3-14 show the normalized magnitude square of Q as a function of the scanning-source range. In the case of the PE model, Figs. (b), we assumed an absorbing bottom and an acoustic frequency of 50 Hz, and a mesh setup with increments of 100 m in range and 50 m in depth. The same parameters for the adiabatic model were used, except no bottom model is included, since, only the water borne modes are considered. In both cases we assumed that the target/reference separation is 25 km, so the test source will scan an area of 50 km with the target between the reference array and the farthest searching point. On the plots the virtual array is located at range 0 km, the target at 25 km, and the receiving array (not shown) at -450 km.

A sharp focus of acoustic signal is observed at the correct location of 25 km in Figs. 3-13 and 3-14. The width of the central lobe is about 500 m at the 1/2 power level. The highest sidelobes are more than 10 dB down from the peak. Simulation for the focusing in depth was done; see Fig. 3-15. This plot shows a color image of the normalized Q magnitude, where the color scale is linear with red representing high intensity and blue representing low intensity. This image was obtained for the same parameters as for Figs. 3-13 and 3-14, using the PE propagation model (FEPE). The focus is clearly observed at the exact range and depth of the target. A very sharp focus in depth at the location of the target was found. The explanation for this behavior is as follows. When we are at the target range, the phase of each mode is zero, and what remains in the expression for Q are the eigenfunctions, which are oscillatory functions. When we are at the right depth and the right range, $(r', z') \Rightarrow (r_t, z_t)$, as it was explained in the previous chapter, the terms in the summation are positive. When z' is different from z_t, the summation tends to zero.

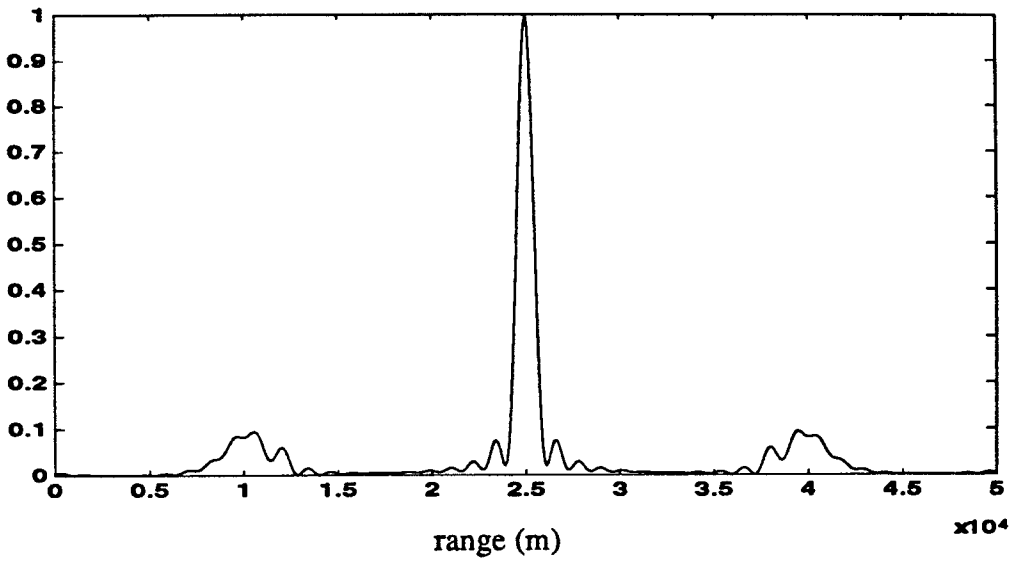

(a)

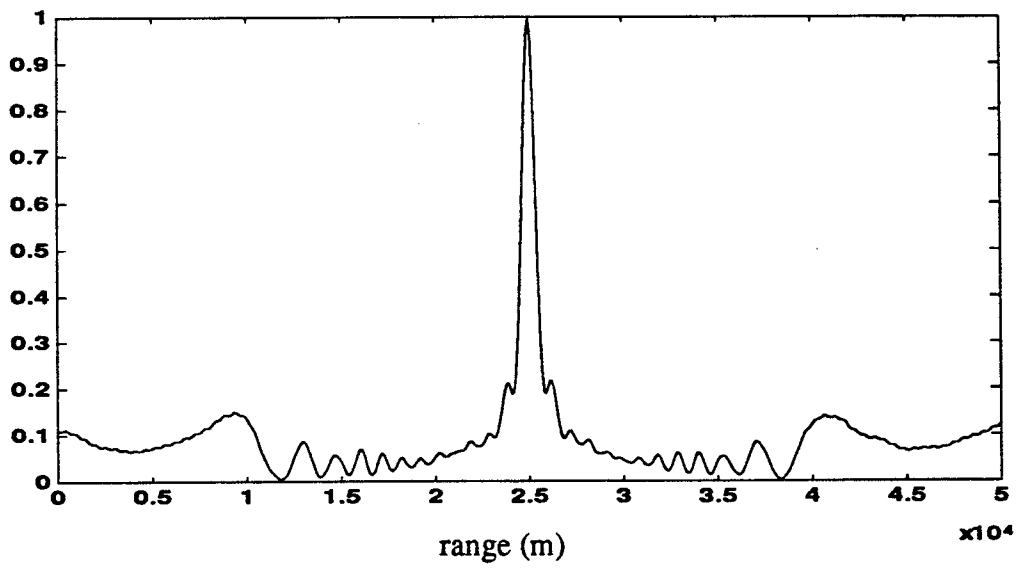

(b)

FIGURE 3-13. The magnitude of the normalized Q squared.(a) Using the adiabatic mode propagation model, (b) using the wide angle PE wave propagation model (FEPE).

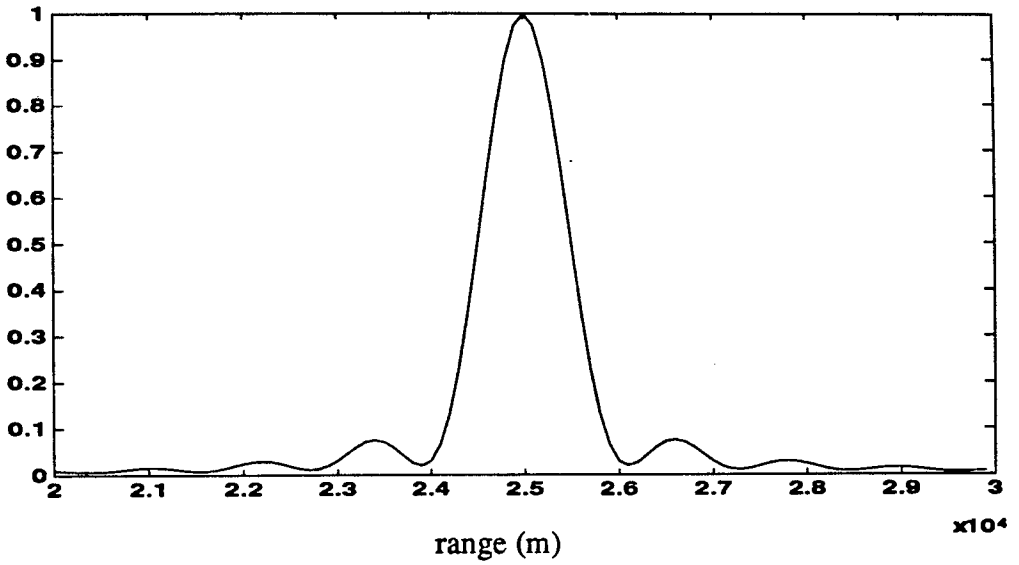

(a)

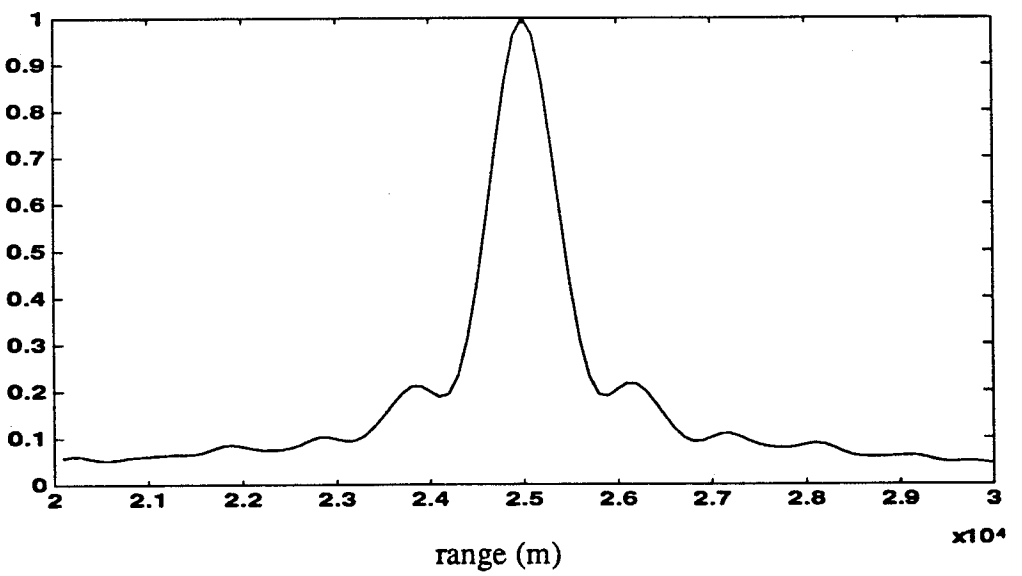

(b)

FIGURE 3-14. Same as Fig. 3-13, but zoomed-in on the target; (a) Adiabatic, (b) FEPE

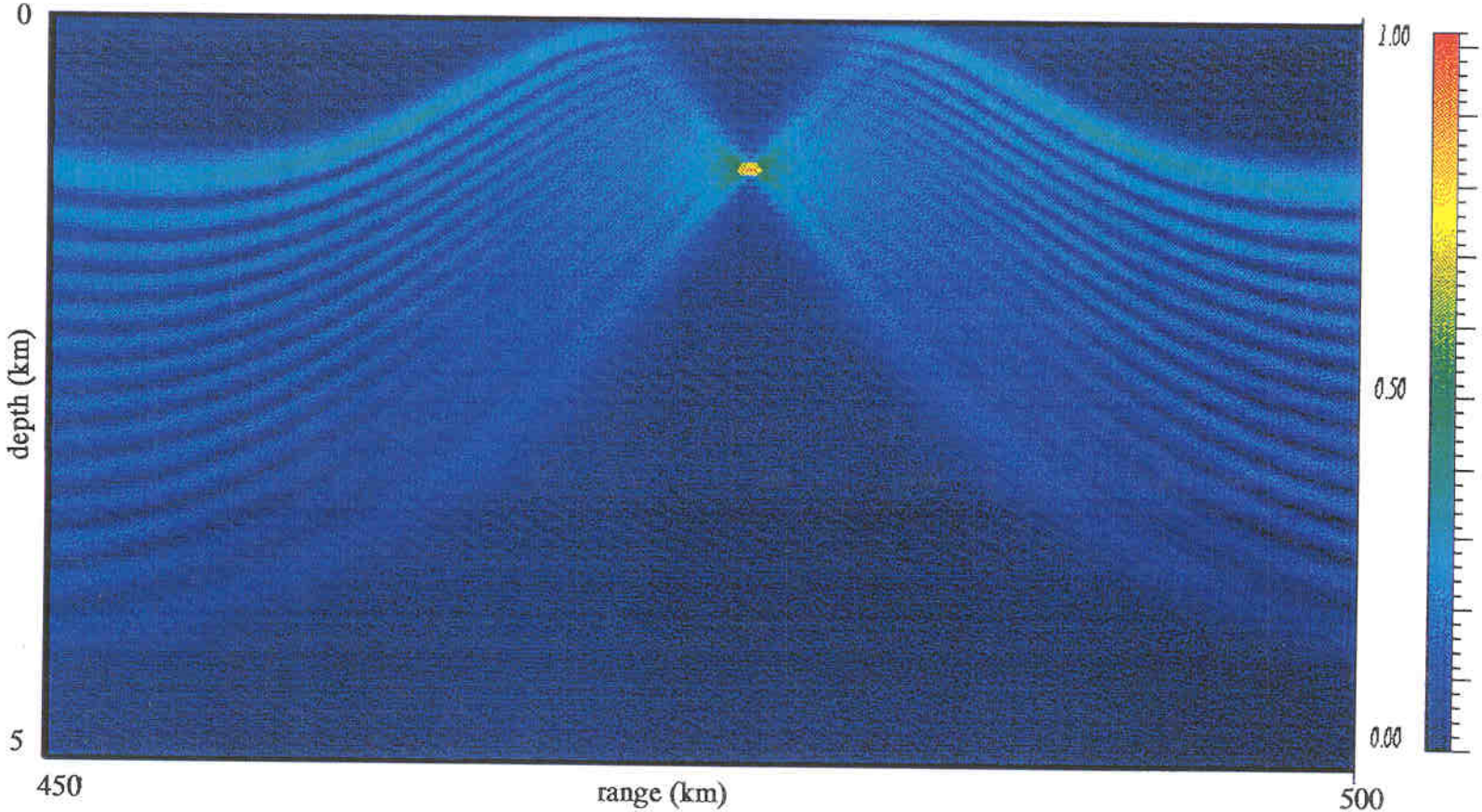

FIGURE 3-15. Color image of the reconstructed field using HAP with a range dependent Munk SSP.

3-2.2 Measured Sound Speed Profile

Real, measured SSP can provide a more challenging test of the HAP method than the Munk profile. Fig. 3-16(a) shows the region of the North Pacific where the experiment SLICE 89 was conducted. Real data where collected along the three legs of the triangle shown on the picture [18][19]. One set of data was collect during deployment in May 89, and another set of data was collected during recovery in September 89. This will give six sets of data with geographical and seasonal variations. In testing the holographic processor we used the data collected in May, along leg 1-2 (North-South). The length of this leg is 950 km and a profile was taken every 10 km.

Three representative profiles are shown in Fig. 3-16(b), taken from the May data set: The beginning of the path "1" (the solid line), the middle of the path (the dashed line), and 500 km south of point "1" (the doted line). We have a total of 50 profiles. We used FEPE with these profiles and assumed a target located at 475 km south of point "1", and a virtual array at 450 km south of point "1", as previously for the Munk profile. Fig. 3-17 shows strong focusing of the HAP, similar to what we have with the Munk profile. The 1/2 power width is still less than 1 km, and the sidelobes are more than 10 dB below the focal point level. The focal region is strongly asymmetric, reflecting the strong irregular range dependency of the SSP.

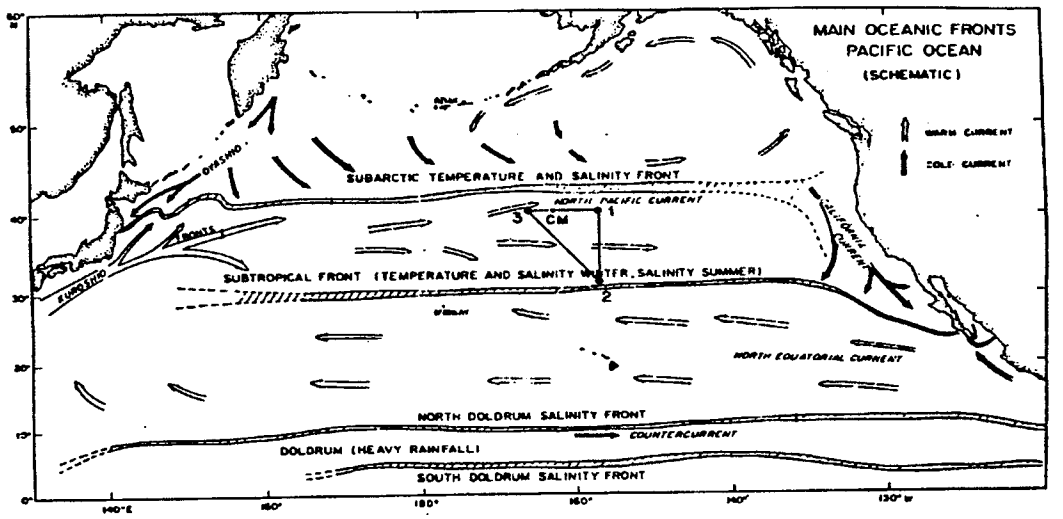

(a)

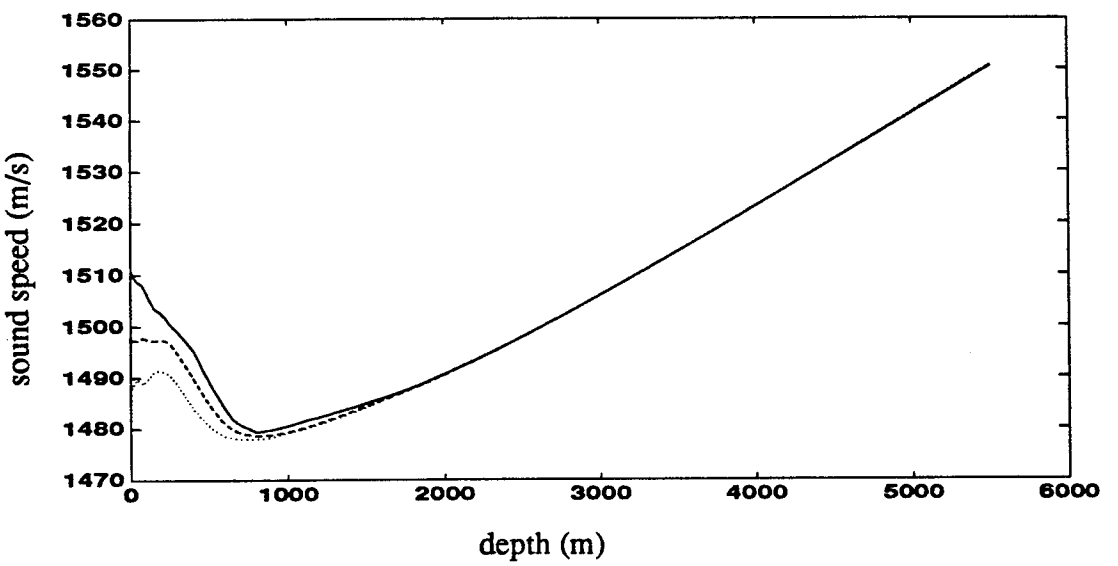

(b)

FIGURE 3-16. (a) SLICE 89 experiment course (triangle). (b) Representative SSP along the North - South leg from the May data, over a range of 500 km: the solid line represents the SSP at point 1, the dashed line represents the SSP at 250 km south of point 1, and the doted line represents the SSP at 500 km south of point 1.

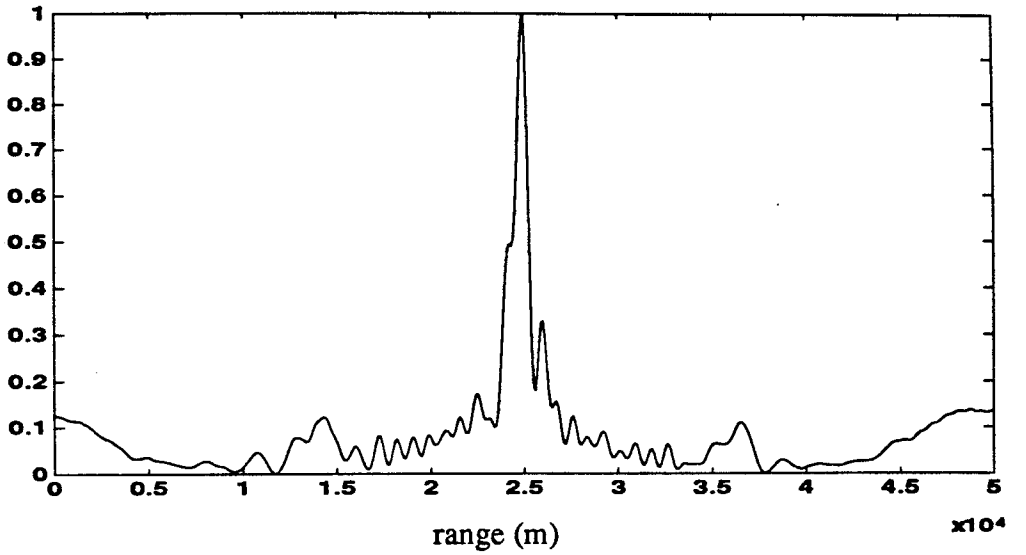

(a)

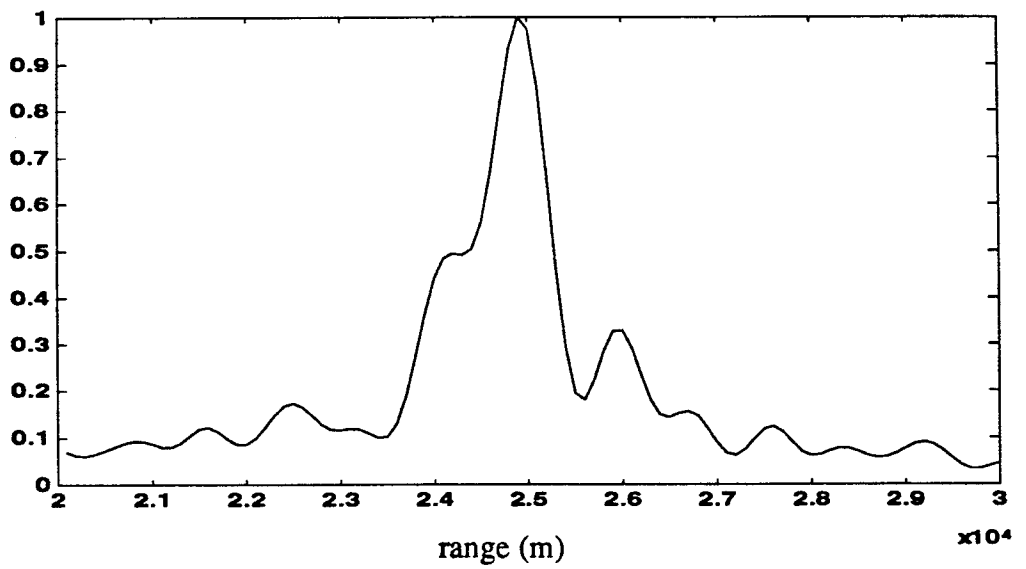

(b)

FIGURE 3-17. The reconstructed field as a function of range at the target's depth, using the HAP algorithm with measured sound speed data from the North Pacific ocean.

CHAPTER 4

Truncated Array

In deep water, the ideal situation of having a receiving array and reference source that span the water column may not be practical. We may have to deal with a receiving array that extends from the surface, or just below the surface, to a certain depth, usually much shallower than the depth of the ocean. Similarly, we may have to deal with a reference source that cannot be deployed very deep.

In this chapter we analyze how truncating both the receiving and the reference source array affects the performance of the holographic array processing algorithm.

4-1 Theoretical Analyses

Assume that the receiving array extends from the surface to a certain depth, $\hat{h}$, where $\hat{h} \leq h$, and h is the total depth of the water column, as illustrated in Fig. 4-1. Also, we assume that the reference source spans the water column from the surface to a certain depth, $\hat{h}_R$, where $\hat{h}_R \leq h_R$ and h_R is the total depth of the water column where the reference source is deployed.

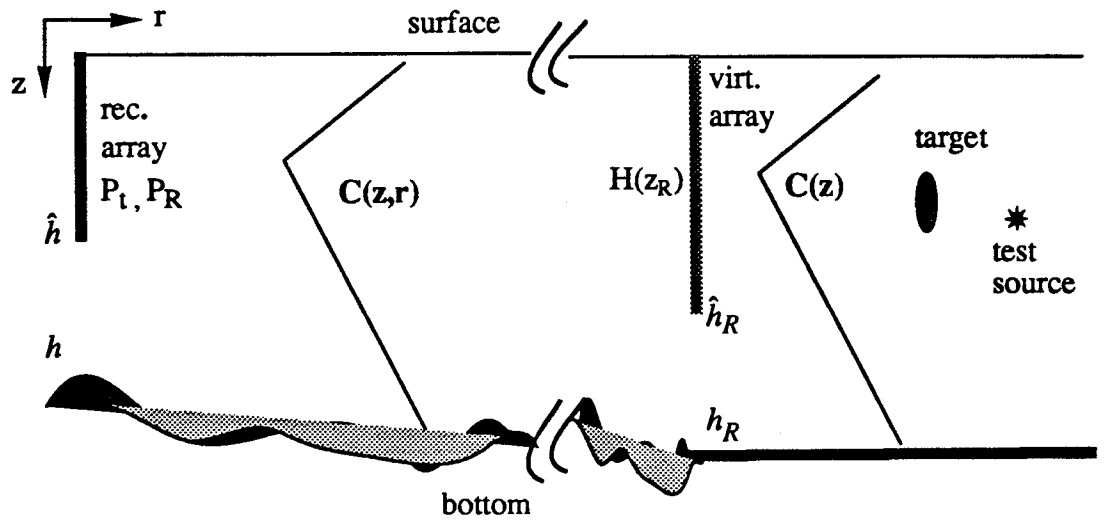

FIGURE 4-1. Sketch of the ocean model with truncated receiving and virtual arrays.

Using these definitions, the holographic image at the virtual array is

$$\hat{H}(z_R) = \int_0^{\hat{h}} P_t(z;r_t, z_t) P_R^*(z;r_R, z_R)\, dz \tag{4-1}$$

where $P_t(z;r_t, z_t)$ is the pressure at the receiving array from the target located at distance r_t and depth z_t, and $P_R^*(z;r_R, z_R)$ is the complex conjugate of the received pressure from a reference source at range r_R and depth z_R. The holographic image can be rewritten in terms of the ocean depth h as,

$$\hat{H}(z_R) = \int_0^{h} P_t(z;r_t, z_t) P_R^*(z;r_R, z_R)\, dz - \int_{\hat{h}}^{h} P_t(z;r_t, z_t) P_R^*(z;r_R, z_R)\, dz \quad . \tag{4-2}$$

The first term represents the holographic image $H(r_R, z_R)$, in the case of a full length receiving array that spans the water column from surface to bottom, $\hat{h} = h$. Thus, Eq. (4-2) can be written as

$$\hat{H}(z_R) = H(r_R, z_R) - \int_{\hat{h}}^{h} P_t(z;r_t, z_t) P_R^*(z;r_R, z_R)\, dz \quad . \tag{4-3}$$

The reconstructed image, as a result of weighting the holographic image by the pressure from a test point source at range r' and depth z', $P(r_R, z_R;r', z')$, and averaging over the truncated virtual array, is

$$\hat{Q}(r', z') = \int_0^{\hat{h}_R} P(r_R, z_R;r', z') \hat{H}^*(r_R, z_R)\, dz_R \tag{4-4}$$

where $\hat{h}_R$ is the truncated depth of the virtual array. In terms of the ocean depth at the reference location, h_R, the reconstructed image is

$$\hat{Q}(r', z') = \int_0^{h_R} P(r_R, z_R; r', z') \hat{H}^*(z_R)\, dz_R - \int_{\hat{h}_R}^{h_R} P(r_R, z_R; r', z') \hat{H}^*(z_R)\, dz_R \quad . \quad (4\text{-}5)$$

Substituting Eq. (4-3) into Eq. (4-5) we get

$$\begin{aligned}
\hat{Q}(r', z') = & \int_0^{h_R} P(r_R, z_R; r', z') H^*(r_R, z_R)\, dz_R \\
& - \int_0^{h_R} dz_R \int_{\hat{h}}^{h} dz P(r_R, z_R; r', z') P_t^*(z; r_t, z_t) P_R(z; r_R, z_R) \\
& - \int_{\hat{h}_R}^{h_R} P(r_R, z_R; r', z') H^*(z_R)\, dz_R \\
& + \int_{\hat{h}_R}^{h_R} dz_R \int_{\hat{h}}^{h} dz P(r_R, z_R; r', z') P_t^*(z; r_t, z_t) P_R(z; r_R, z_R) \quad .
\end{aligned} \quad (4\text{-}6)$$

The first term in Eq. (4-6) is the original definition of the reconstructed image when neither the receiving array nor the virtual array is truncated, and it is equal to $Q(r', z')$. The second term gives the effect of truncating the receiving array, the third term gives the effect of truncating the virtual array, and the fourth term gives the effect of truncating both the receiving and virtual arrays.

Letting $\hat{h} = h$, thus truncating the virtual array only, the second and fourth terms are zero, and the reconstructed image will be

$$\hat{Q}(r', z') = Q(r', z') - \int_{\hat{h}_R}^{h_R} P(r_R, z_R; r', z') H^*(z_R)\, dz_R \quad . \quad (4\text{-}7)$$

While, letting $\hat{h}_R = h_R$, thus truncating the receiving array only, the third and fourth terms will be zero, and the reconstructed image will be

$$\hat{Q}(r', z') = Q(r', z') - \int_0^{h_R} dz_R \int_{\hat{h}}^{h} dz P(r_R, z_R; r', z') P_t^*(z; r_t, z_t) P_R(z; r_R, z_R) \quad . \quad (4\text{-}8)$$

The second term in Eq. (4-7) and Eq. (4-8) represents the disturbance (error) factor due to the two truncation scenarios. A clearer quantitative analysis can be achieved using the normal mode representation.

4-1.1 Normal Mode Representation

At the receiving array we measure the pressure fields from the target and the reference source as the latter is deployed to various depths; while at the virtual array we compare the calculated pressure field from a test source with the holographic image. Therefore, the reconstructed field depends mainly on the fidelity of the holographic image, and the fidelity of the field from the test source as calculated along the virtual array.

We assume that the virtual array is very long and adequately sampled and that the receiving array, Fig. 4-2, is long enough to adequately measure most of the modes, especially the lower order modes. Then the holographic image is accurately estimated along the full length virtual array, and the field from the test source is adequately sampled by the long virtual array. As a result we expect no major degradation in the reconstructed image. Thus, we will be able to reconstruct the wavefront from the limited information in the original hologram (receiving array) almost perfectly, because the full length virtual array cancels out the media effects for all the measured paths, as shown in Fig. 4-3. As the receiving array becomes very short, the lower order modes are poorly resolved, adversely affecting the resolution of the reconstructed image.

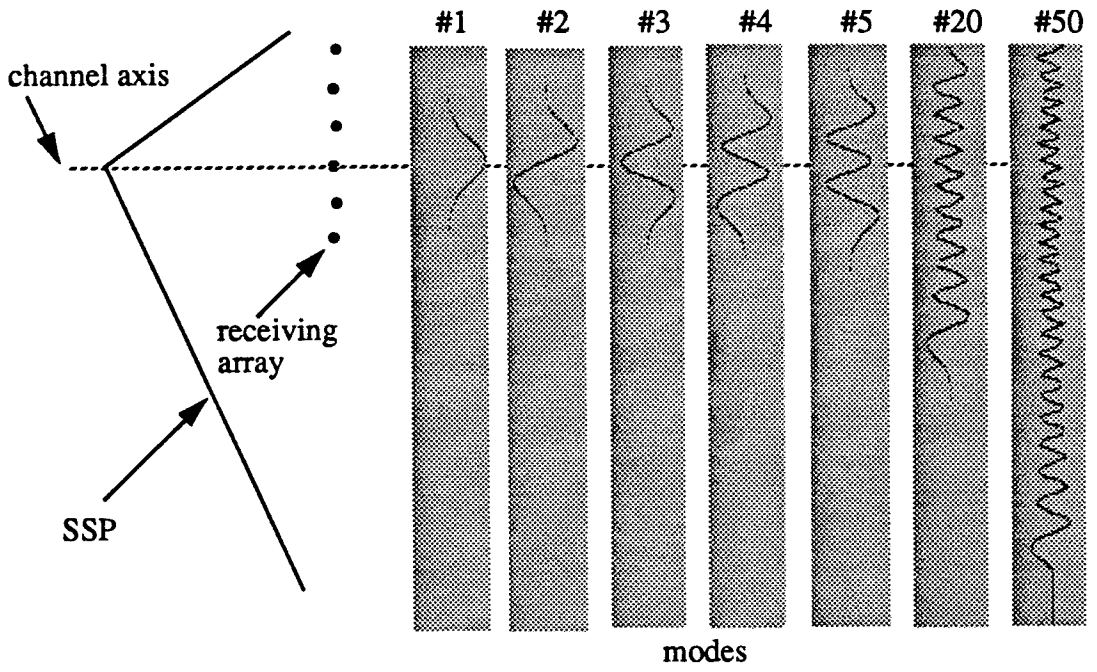

FIGURE 4-2. Diagram of the different modes as measured by a truncated receiving array.

Shortening the virtual array will result in a limited cancellation of the medium effects for the measured paths. In Fig. 4-4, paths 1 and 2 from the target are completely phase compensated by corresponding paths from the reference array. Paths 3 and 4 are partially phase compensated by corresponding paths from the reference array, path 3 propagates over a range x_1 from the reference array with no phase compensation, and path 4 propagates over range x_2 with no phase compensation. Finally path 5 is not phase compensated. Since the effect of the noncompensated, or partially compensated paths, can be quite large for long range propagation, virtual array truncation may result in a holographic image with distorted phase. Also, the shorter virtual array will poorly resolve the lower order modes which carry quite a bit of information. Thus the combination of not phase compensating certain paths and poorly resolving certain modes will result in a severe degradation of the reconstructed image even if the receiving array spans the whole water column.

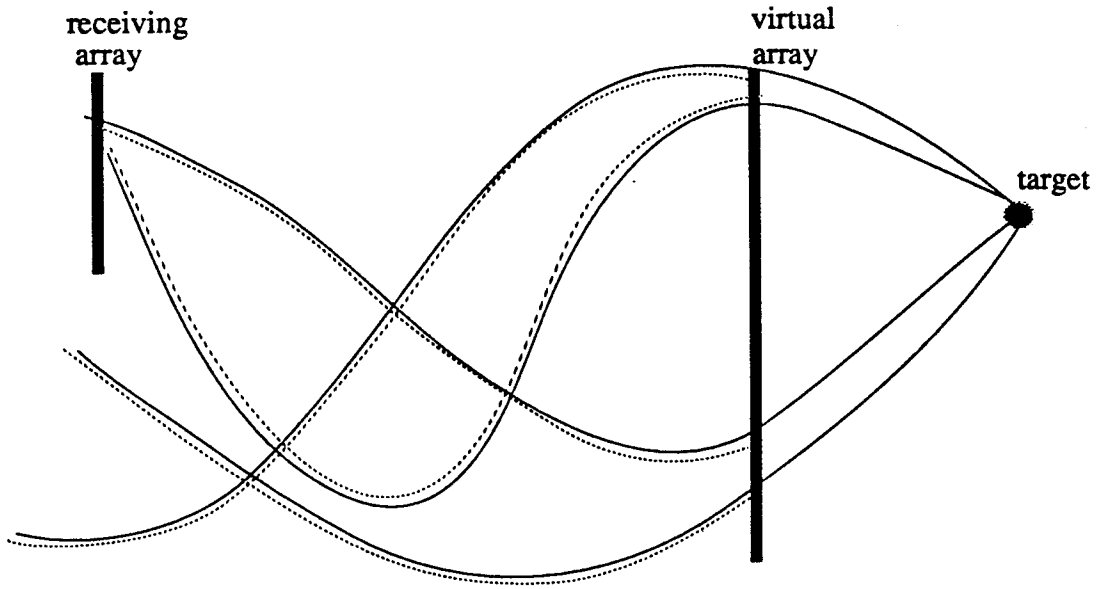

FIGURE 4-3. Schematic representation of the HAP algorithm with a truncated receiving array. All the paths from the target are calibrated by the virtual array.

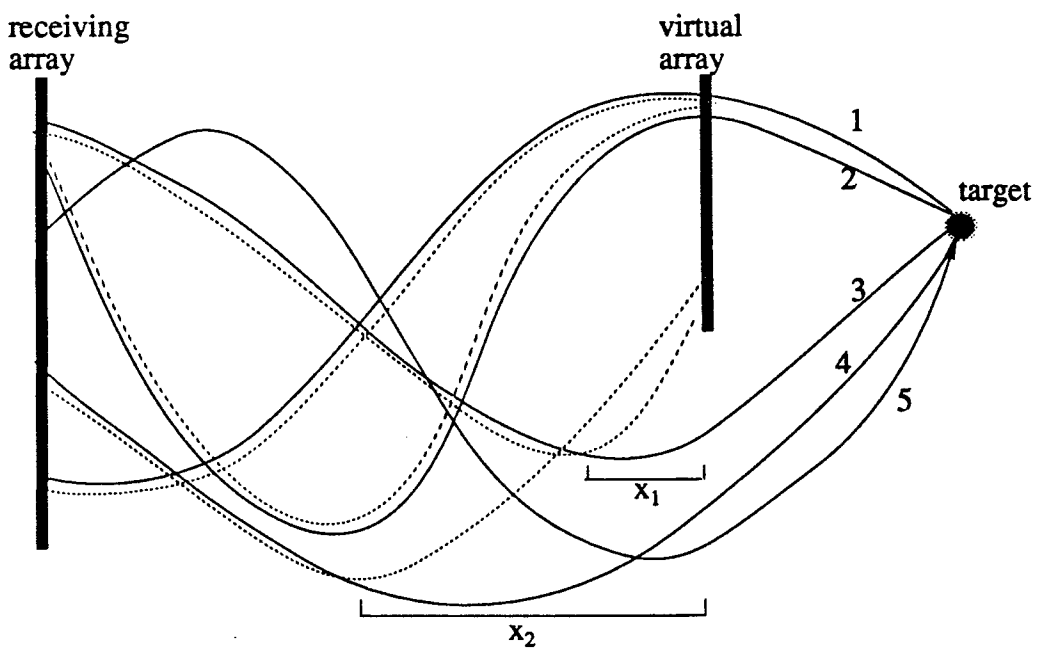

FIGURE 4-4. Schematic representation of the HAP algorithm with a truncated virtual array. Some paths from the target are not completely calibrated by the virtual array.

Normal mode theory yields additional understanding of the different roles that the truncated receiving and virtual arrays play in degrading the reconstructed image. Comparing the measured and estimated (calculated) modes associated with both the receiving and virtual arrays will lead to a quantitative and qualitative evaluation of the degradation due to the different schemes of array truncation.

Eq. (2-32) shows the pressure at range r and depth z from a point source at range r_s and depth z_s in a range dependent adiabatic medium, and is repeated here for convenience:

$$P(r, z; r_s, z_s) = \left(\frac{2}{\pi r}\right)^{1/2} e^{-i\pi/4} \sum_m \psi_m(r, z)\, \psi_m^*(r_s, z_s)\, [\xi_m(r)]^{-1/2} \times exp\left[-i \int_0^r \xi_m(\tilde{r})\, d\tilde{r}\right] \tag{4-9}$$

where $\psi_m(r,z)$ is the eigenfunction of the m^{th} mode at range r and depth z, and ξ_m is the horizontal eigennumber of the m^{th} mode. Substituting Eq. (4-9) into Eq. (4-3) we get the modal representation of the depth dependent holographic image,

$$\hat{H}(r_R, z_R) = H(r_R, z_R) - \frac{2}{\pi \sqrt{r_t r_R}} \sum_m \sum_n \psi_m^*(r_t, z_t)\, \psi_n(r_R, z_R) \times \frac{exp\left[-i \int_0^{r_t} \xi_m(\tilde{r})\, d\tilde{r} - i \int_0^{r_R} \xi_n(\tilde{r})\, d\tilde{r}\right]}{\sqrt{\xi_m(r_t)\, \xi_n(r_R)}} \int_{\hat{h}}^{h} \psi_m(r_0, z)\, \psi_n^*(r_0, z)\, dz \ . \tag{4-10}$$

When $\hat{h} = h$ the second term, Eq. (4-10), will be zero and $\hat{H}(z_R) = H(z_R)$. The other scenario is when $0 < \hat{h} < h$; then the second term, Eq. (4-10), represents a degradation factor subtracted from the original (nonperturbed) holographic image.

The normal mode representation of the reconstructed image, Eq. (4-6), is

$$\hat{Q}(r', z') = Q(r', z') - A\sum_m\sum_n\sum_l \frac{exp\left[-i\left\{\int_0^{r_t}\xi_m(\tilde{r})\,d\tilde{r} - \int_0^{r_R}\xi_n(\tilde{r})\,d\tilde{r} - \hat{\xi}_l(r'-r_R)\right\}\right]}{\sqrt{\xi_m(r_t)\,\xi_n(r_R)\,\hat{\xi}_l}}$$

$$\times \psi_m(r_t, z_t)\,\hat{\psi}_l^*(r', z')$$

$$\times \left\{ \begin{array}{l} \delta_{nl}\int_{\hat{h}}^{h}\psi_m(r_0, z)\,\psi_n^*(r_0, z)\,dz + \delta_{mn}\int_{\hat{h}_R}^{h_R}\psi_n^*(r_R, z_R)\,\hat{\psi}_l(r_R, z_R)\,dz_R \\ -\int_{\hat{h}}^{h}\psi_m(r_0, z)\,\psi_n^*(r_0, z)\,dz\int_{\hat{h}_R}^{h_R}\psi_n^*(r_R, z_R)\,\hat{\psi}_l(r_R, z_R)\,dz_R \end{array} \right\} \tag{4-11}$$

where $A = \dfrac{(2/\pi)^{3/2}}{\sqrt{r_t r_R |r' - r_R|}} e^{-i\pi/4}$,

$$\delta_{nl} \equiv \int_0^{h_R}\psi_n^*(r_R, z_R)\,\hat{\psi}_l(r_R, z_R)\,dz_R \ , \tag{4-12}$$

and

$$\delta_{mn} = \int_0^{h}\psi_m(r_0, z)\,\psi_n^*(r_0, z)\,dz \ . \tag{4-12a}$$

δ_{mn} is the Kronecker delta function, and, if we assume that the measured and calculated (estimated) eigenfunctions along the virtual array are the same, then Eq. (4-12) approximates δ_{nl}. This representation, Eq. (4-11), leads us to analyze three cases:

I. No Truncation

Both the receiving and reference array span the ocean column from surface to bottom, $\hat{h} = h$ and $\hat{h}_R = h_R$; then the three terms in brackets, Eq. (4-11), will be zero, and no truncation effect is in place.

II. Truncated Receiving Array

The receiving array stretches from the surface of the ocean to a certain depth while the reference array spans the water column from surface to bottom, $\hat{h} < h$ and $\hat{h}_R = h_R$; see Fig. 4-3. Then both the second and third terms in brackets, Eq. (4-11), are equal to zero, and assuming that $\hat{\xi}_n = \xi_n(r_R)$, the reconstructed image is

$$\hat{Q}(r', z') = Q(r', z') - A \sum_m \sum_l \frac{exp\left[-i\left\{\int_0^{r_t} \xi_m(\tilde{r})\, d\tilde{r} - \int_0^{r_R} \xi_l(\tilde{r})\, d\tilde{r} - \hat{\xi}_l(r' - r_R)\right\}\right]}{\sqrt{\xi_m(r_t)\, \xi_l(r_R)\, \hat{\xi}_l}}$$

$$\times \psi_m(r_t, z_t)\, \hat{\psi}_l^*(r', z') \int_{\hat{h}}^{h} \psi_m(r_0, z)\, \psi_l^*(r_0, z)\, dz \ . \tag{4-13}$$

For an appropriately sampled long receiving array we may have an almost complete set of measured modes, and as a result the eigenfunctions under the integral in Eq. (4-13) are quasi-orthonormal; this means that

$$\int_0^{\hat{h}} \psi_m(z)\, \hat{\psi}_l^*(z)\, dz \equiv \begin{cases} 1+\varepsilon & for \quad m = l \\ \varepsilon_{ml} & for \quad m = l \pm L \\ 0 & else \end{cases} \tag{4-14}$$

where ε is a small number, and L is a series of integers, $L = \{1, 2, 3, \ldots\}$. The length of L depends on the size of the array, as illustrated in Fig. 4-5, which shows the correlation of the 10th mode with the other modes for various array lengths.

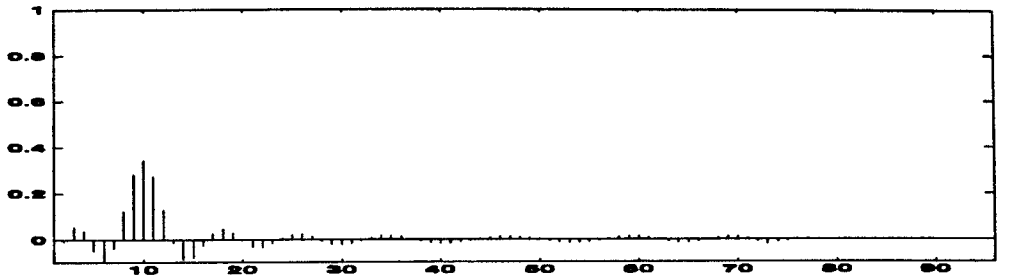

(a)

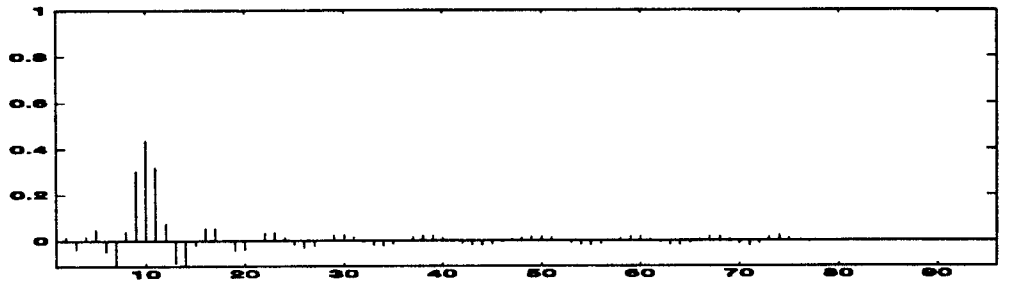

(b)

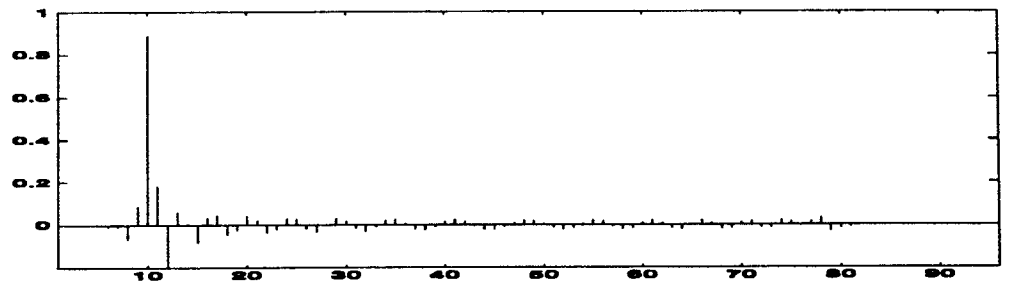

(c)

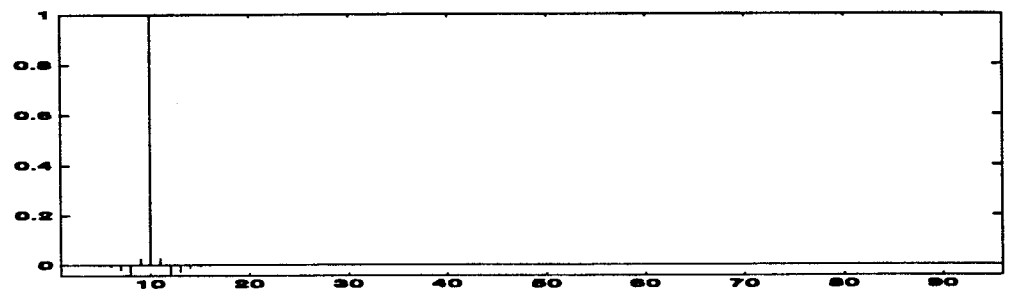

(d)

FIGURE 4-5. The correlation of the 10 th mode with the other modes over a truncated array. The truncated array length is: (a) 1000 m, (b) 1500 m, (c) 2000 m, (d) 2500 m.

For a sufficiently long array, only the diagonal, sub-diagonal, and super-diagonal elements of the eigenfunctions correlation matrix have significant values. Therefore, the residual integral in Eq. (4-13) is

$$\int_{\hat{h}}^{h} \psi_m(z)\,\hat{\psi}_l^*(z)\,dz \equiv \begin{cases} \varepsilon & \text{for } m = l \\ \varepsilon_{ml} & \text{for } m = l \pm 1 \\ 0 & \text{else} \end{cases} \tag{4-15}$$

where we assume that the eigenfunctions are orthonormal over the full water column. Thus, the residual integral in Eq. (4-13) is very small. The phase of the error term, at ranges comparable with the target range, is

$$\varphi_{ml} = \int_0^{r_t} \xi_m(\tilde{r})\,d\tilde{r} - \int_0^{r_R} \xi_l(\tilde{r})\,d\tilde{r} - \hat{\xi}_l(r' - r_R) \quad . \tag{4-16}$$

Assuming that $r_t > r_R$ then

$$\begin{aligned} \varphi_{ml} &= \int_0^{r_R} \xi_m(\tilde{r})\,d\tilde{r} + \int_{r_R}^{r_t} \xi_m(\tilde{r})\,d\tilde{r} - \int_0^{r_R} \xi_l(\tilde{r})\,d\tilde{r} - \hat{\xi}_l(r' - r_R) \\ &= \int_0^{r_R} [\xi_m(\tilde{r}) - \xi_l(\tilde{r})]\,d\tilde{r} + \int_{r_R}^{r_t} \xi_m(\tilde{r})\,d\tilde{r} - \hat{\xi}_l(r' - r_R) \quad . \end{aligned} \tag{4-17}$$

Introducing the mean modal value

$$\overline{\xi_m} = \frac{1}{|r_1 - r_2|} \int_{r_1}^{r_2} \xi_m(\tilde{r})\,d\tilde{r} \tag{4-18}$$

Eq. (4-17) can be written as

$$\varphi_{ml} = \int_0^{r_R} [\xi_m(\tilde{r}) - \xi_l(\tilde{r})]\,d\tilde{r} + \overline{\xi_m}(r_t - r_R) - \hat{\xi}_l(r' - r_R) \quad . \tag{4-19}$$

Scanning in the neighborhood of the target, where $r' = r_t \pm \Delta r$, and Δr is very small range, then the phase of the error term is

$$\varphi_{ml} = \int_0^{r_R} [\xi_m(\tilde{r}) - \xi_l(\tilde{r})]\, d\tilde{r} + \overline{\xi_m}(r_t - r_R) - \hat{\xi}_l[(r_t + \Delta r) - r_R]$$
$$= \int_0^{r_R} [\xi_m(\tilde{r}) - \xi_l(\tilde{r})]\, d\tilde{r} + (\overline{\xi_m} - \hat{\xi}_l)(r_t - r_R) + \hat{\xi}_l \Delta r \quad . \tag{4-20}$$

In the limit, as Δr shrinks to zero, the phase of the error term becomes

$$\varphi_{ml} \approx \int_0^{r_R} [\xi_m(\tilde{r}) - \xi_l(\tilde{r})]\, d\tilde{r} + (\overline{\xi_m} - \hat{\xi}_l)(r_t - r_R) \quad . \tag{4-21}$$

From the above, we conclude that the coupling of the neighboring modes contributes to the error term in Eq. (4-13) with a scaled modal amplitude ε_{ml} and phase φ_{ml}. Thus, the error term is

$$E^{TR}(r', z') = A \sum_m \sum_l \frac{e^{-i\varphi_{ml}}}{\sqrt{\xi_m \xi_l \hat{\xi}_l}} \psi_m(r_t, z_t)\, \hat{\psi}_l^*(r', z')\, \varepsilon_{ml} \quad . \tag{4-22}$$

For widely separated modes, the mode coupling integral is very small, $\varepsilon_{ml} \approx 0$, see Fig. 4-5; therefore, the error term is negligible, $E^{TR} \approx 0$. For the neighboring modes, the difference between the modal horizontal wavenumbers, $\xi_m - \xi_l$, is very small, on the order[1] of 10^{-4} to 10^{-6} (the closer the modes are, the smaller the modal difference is); see Fig. 3-4. Assuming that $\hat{\xi}_m \equiv \overline{\xi_m}$ between r_t and r_R, then the main contribution to the phase fluctuation, when $r' \approx r_t$, is from the first term in Eq. (4-21). The modal difference in the first term is integrated along the receiver/reference separation, which is on the order of hundreds of kilometers, while in the second term, the modal difference is integrated over the target/reference separation, which is on the order[2] of tens of kilometers. Therefore, a small change in the difference in horizontal wavenumbers produces a significant

1. These values are taken from the adiabatic ocean model that is presented in chapter 3.

fluctuation in the phase, and the error terms become oscillatory, resulting in a noncoherent summation over all modes. Therefore, the total error term tends to zero and the image degradation effect will be reduced.

An excessively short receiving array will result in poorly resolved lower order modes which propagate close to the sound speed channel, Fig. 4-2. Only the higher order modes will be adequately sampled and well represented by the measurements. Also, for a receiving array much shorter than the depth of the channel axis, the quasi-orthonormal property of the eigenfunctions will not be satisfied over the receiving array, but it will be sustained over the complementary depth of the receiving array, $\hat{h}$ to h,

$$\int_{\hat{h}}^{h} \psi_m(z)\,\hat{\psi}_l^*(z)\,dz = \begin{cases} 1+\varepsilon & \text{for } m = l \\ \varepsilon_{ml} & \text{for } m = l \pm L \\ 0 & \text{else} \end{cases} . \tag{4-23}$$

Thus the error term in Eq. (4-13) will be

$$E^{TR}(r', z') = A \sum_m \sum_l \frac{e^{-i\varphi_{ml}}}{\sqrt{\xi_m(r_t)\,\xi_l(r_R)\,\hat{\xi}_l}} \psi_m(r_t, z_t)\,\hat{\psi}_l^*(r', z')\,(\delta_{ml} + \varepsilon_{ml}) \tag{4-24}$$

where δ_{ml} is the Kronecker delta. Considering Eq. (4-17), the error term becomes

2. For the ocean model considered in the previous chapter, $r_R \sim 500$ km and $r_t - r_R \sim 20$ km. Assuming an average wavenumber difference on the order of 10^{-5}, then, the first term in Eq. (4-21) is on the order of 5 rad, and the second term is on the order of 0.2 rad.

$$E^{TR}(r',z') = A\sum_m \psi_m(r_t,z_t)\,\hat{\psi}_m^{*}(r',z')\left[\xi_m(r_t)\,\xi_m(r_R)\,\hat{\xi}_m\right]^{-1/2}\times$$

$$exp\left[-i\left\{\int_{r_R}^{r_t}\xi_m(\tilde{r})\,d\tilde{r}-\hat{\xi}_m(r'-r_R)\right\}\right]$$

$$+A\sum_m\sum_l \frac{exp\,[-i\varphi_{ml}]}{\sqrt{\xi_m(r_t)\,\xi_l(r_R)\,\hat{\xi}_l}}\psi_m(r_t,z_t)\,\hat{\psi}_l^{*}(r',z')\,\varepsilon_{ml} \quad . \tag{4-25}$$

Because the first term is equal to $Q(r',z')$ we can write

$$E^{TR}(r',z') = Q(r',z') + A\sum_m\sum_l \psi_m(r_t,z_t)\,\hat{\psi}_l^{*}(r',z')\times$$

$$\left[\xi_m(r_t)\,\xi_l(r_R)\,\hat{\xi}_l\right]^{-1/2} exp\,[-i\varphi_{ml}]\,\varepsilon_{ml} \; . \tag{4-26}$$

Substituting Eq. (4-26) in Eq. (4-13) we get

$$\hat{Q}(r',z') = -A\sum_m\sum_l \psi_m(r_t,z_t)\,\hat{\psi}_l^{*}(r',z')\left[\xi_m(r_t)\,\xi_l(r_R)\,\hat{\xi}_l\right]^{-1/2}\times$$

$$exp\,[-i\varphi_{ml}]\,\varepsilon_{ml} \; . \tag{4-27}$$

Therefore, when the receiving array is excessively short, the quasi-orthogonality property does not hold, and the reconstructed image has large error; therefore, the algorithm will fail.

III. Truncated Virtual Array

The receiving array spans the water column of the ocean from surface to bottom, $\hat{h} = h$, while the reference source is deployed from surface to a certain depth in the water creating a limited length virtual array, $\hat{h}_R < h_R$ (see Fig. 4-4). The first and third terms in brackets, Eq. (4-11), are equal to zero and the reconstructed image is

$$\hat{Q}(r', z') = Q(r', z') - A \sum_m \sum_l \frac{exp\left[-i \int_0^{r_t} \xi_m(\tilde{r})\, d\tilde{r} - i \int_0^{r_R} \xi_m(\tilde{r})\, d\tilde{r} - \hat{\xi}_l (r' - r_R) \right]}{\sqrt{\xi_m(r_t)\, \xi_m(r_R)\, \hat{\xi}_l}} \times$$

$$\psi_m(r_t, z_t)\, \hat{\psi}_l^*(r', z') \int_{\hat{h}_R}^{h_R} \psi_m^*(r_R, z_R)\, \hat{\psi}_l(r_R, z_R)\, dz_R \,. \tag{4-28}$$

A similar argument as in the previous case, regarding the quasi-orthonormal property of the eigenfunctions over a truncated array, is valid. Comparing Eq. (4-28) with Eq. (4-13) and assuming that the water column at the virtual array is of the same depth as that at the receiving array, $h_R = h$, and the truncated virtual array is of the same length as the truncated receiving array, $\hat{h}_R = \hat{h}$, then Eq. (4-28) is similar to Eq. (4-13), except for the phase term and the eigenfunction correlation matrix. In Eq. (4-13) the eigenfunction correlation matrix is found for the measured eigenfunctions along the receiving array; however, in Eq. (4-28) the cross correlation matrix between the measured and the calculated (estimated) eigenfunctions is found. The measured eigenfunctions, $\psi_m(r_R, z_R)$, can be found from the modal decomposition of the measured pressure field, from the reference source at (r_R,z_R), along the receiving array. The estimated eigenfunctions, $\hat{\psi}_l(r_R, z_R)$, are found using the assumed sound speed profile at the reference location.

Assuming an agreement between the measured and estimated eigenfunctions, $\psi_m(r_R, z_R) = \hat{\psi}_m(r_R, z_R)$, the correlation matrices in Eqs. (4-13) and (4-28) are the same and the algorithm performance with depth in both cases will be equivalent. Otherwise, a poor estimate of the eigenfunctions along the virtual array will result in performance degradation in the vertical (defocusing with depth).

The difference in the phase term for the two truncation scenarios is an indication of different algorithm behavior (focusing) in range. The phase of the error term in Eq. (4-28) is

$$\varphi_{ml} = \int_0^{r_t} \xi_m(\tilde{r})\, d\tilde{r} - \int_0^{r_R} \xi_m(\tilde{r})\, d\tilde{r} - \hat{\xi}_l (r' - r_R) \tag{4-29}$$

assuming that $r_t > r_R$; then the phase of the error term can be written as

$$\begin{aligned} \varphi_{ml} &= \left[\int_0^{r_R} \xi_m(\tilde{r})\, d\tilde{r} + \int_{r_R}^{r_t} \xi_m(\tilde{r})\, d\tilde{r} \right] - \int_0^{r_R} \xi_m(\tilde{r})\, d\tilde{r} - \hat{\xi}_l (r' - r_R) \\ &= \int_{r_R}^{r_t} \xi_m(\tilde{r})\, d\tilde{r} - \hat{\xi}_l (r' - r_R) \quad . \end{aligned} \tag{4-30}$$

Scanning in the neighborhood of the target, where $r' = r_t \pm \Delta r$, and Δr is very small range, and using the modal mean value, Eq. (4-18), then Eq. (4-30) can be written as

$$\varphi_{ml} = \overline{\xi_m} (r_t - r_R) - \hat{\xi}_l [r_t + \Delta r - r_R] \quad . \tag{4-31}$$

In the limit as Δr shrinks to zero, the phase of the error term becomes

$$\varphi_{ml} = (\overline{\xi_m} - \hat{\xi}_l)\, (r_t - r_R) \quad . \tag{4-32}$$

From the above, we conclude that the coupling of the neighboring modes contributes to the error term in Eq. (4-28) with a scaled modal amplitude ε_{ml} and phase φ_{ml}. Therefore, the error term can be written as

$$E^{TV}(r', z') = A \sum_m \sum_l \frac{e^{-i\varphi_{ml}}}{\sqrt{\xi_m \xi_l \hat{\xi}_l}} \psi_m(z_t)\, \hat{\psi}_l^*(z')\, \varepsilon_{ml} \quad . \tag{4-33}$$

Notice that the phase of the error term is a function of the target/reference separation only. For the far apart modes, the scaled modal amplitude is very small, $\varepsilon_{ml} \approx 0$, and as a result the error term is negligible, $E^{TV} \approx 0$. For neighboring modes, and assuming $\hat{\xi}_m \cong \overline{\xi_m}$, then $\xi_m - \xi_l$ is very small, on the order of 10^{-4} to 10^{-6}. Therefore, small changes in the horizontal wavenumber difference, $\overline{\xi_m} - \hat{\xi}_l$, will not result in drastic fluctuations in the phase, since these changes

are integrated over the target/reference separation which is on the order of 10 km. This will lead to a coherent summation of most of the terms in Eq. (4-33), and as a consequence the total error can be significant, leading to severe degradation (defocusing) of the reconstructed image.

Normalizing the magnitude of the truncation error term by the magnitude of the truncation-free reconstructed field, we get

$$\left|E_N^{TR}(r', z')\right| = \frac{\left|E^{TR}(r', z')\right|}{\left|Q(r', z')\right|} \tag{4-34}$$

for the truncated receiving array, and

$$\left|E_N^{TV}(r', z')\right| = \frac{\left|E^{TV}(r', z')\right|}{\left|Q(r', z')\right|} \tag{4-35}$$

for the truncated virtual array. E^{TR} is the error due to truncating the receiving array, Eq. (4-22), and E^{TV} is the error due to truncating the virtual array, Eq. (4-33).

Fig. 4-6 shows the normalized magnitude of the error terms as a function of range, $r' - r_t$. The truncated receiving array and the truncated virtual array are of the same length (1500 m); see Fig. 4-5 for the residual integrals in the error terms for this array length. The ocean model is the same as that used in chapter 3 with exponentially stratified SSP. For all ranges considered (0 to 5000 meters from the target), we notice that the truncated virtual array has a larger error term (solid line) than a comparable truncated receiving array (doted line). Also, the truncated virtual array is more susceptible to changes in Δr, see Eq. (4-31), which is evident from the oscillatory behavior of the solid line.

It can be concluded that the length of the virtual array is more important than the length of the receiving array to the algorithm's performance and the quality of the reconstructed image.

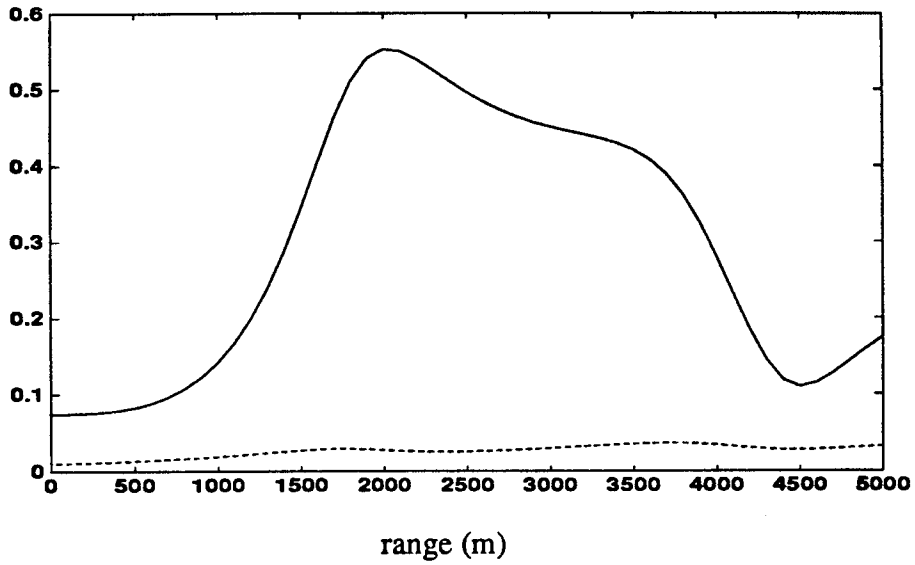

FIGURE 4-6. The magnitude of the normalized error term for truncated receiving array (Eq. 4-22) (doted line), and that for truncated virtual array (Eq. 4-33) (solid line). The horizontal scale shows the range of the test source from the target.

4-2 Simulation Results

The effect of truncating the receiving array, virtual array, or both on the performance of the HAP algorithm is evaluated using a high order PE code, FEPE, in a range dependent ocean with exponentially stratified sound speed profile, Munk profile, where the axis depth is 1000 meters and the range dependency is modeled as a linear variation of the axial sound speed with range. The slope of this variation is taken to be one meter per second per 100 km.

Under ideal conditions, full length receiving array and full length virtual array, we showed that the holographic array processor produces a tight focus at the target location with relatively low level side lobes, Fig. 3-15.

4-2.1 Truncated Receiving Array Simulation

We assume that the length of the receiving array is limited. It extends from the surface of the ocean to a certain depth less than the total depth of the water

column; at the same time, the reference source spans the whole water column, creating a full length virtual array, as illustrated in Fig. 4-7. The target is located at 25 km from the virtual array which in turn is located at 450 km from the receiving array.

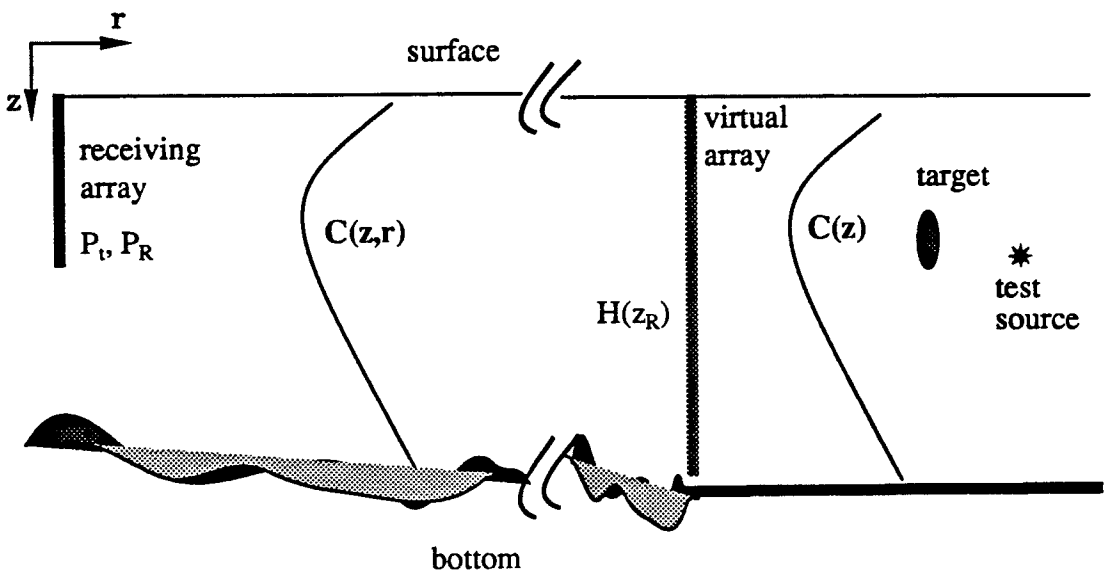

FIGURE 4-7. Schematic diagram of the ocean model with range dependent Munk SSP and truncated receiving array.

Fig. (4-9) shows color images of the magnitude of the reconstructed fields, $\hat{Q}(r', z')$, for various receiving array lengths. The effect of truncating the receiving array on the performance of the HAP algorithm is evident. Fig. 4-10 shows horizontal slices, at the target's depth, of the normalized power of the reconstructed images, $\hat{Q}(r', z_t)$, for various receiving array lengths. It gives a clear picture of the effect of truncating the receiving array on the width of the main lobe (focus) and the level of the side lobes (ambiguity). We see that when the receiving array covers the upper half of the water column, 2500 meters, the algorithm does not suffer from any major degradation; it produces a sharp focus on the target with negligible rise in the side lobes' levels. As we reduce the length of the receiving array down to a depth comparable to the depth of the channel axis, 1000 meters for this ocean model, the major effect on the algo-

rithm performance is a relatively slight increase in the side lobes, but the focus is still sharp at the target. When we implement a receiving array that extends from the surface to a depth shallower than the depth of the channel axis, the algorithm fails to produce a sharp focus and the side lobes rise to high levels, comparable to the main lobe's level.

4-2.2 Truncated Virtual Array Simulation

The receiving array spans the water column of the ocean. The reference source is deployed to a certain depth, less than the total depth of water column at the reference site, creating a truncated virtual array. The ocean model and the separations between the target, virtual array, and receiving array are the same as in the previous section; see Fig. 4-8.

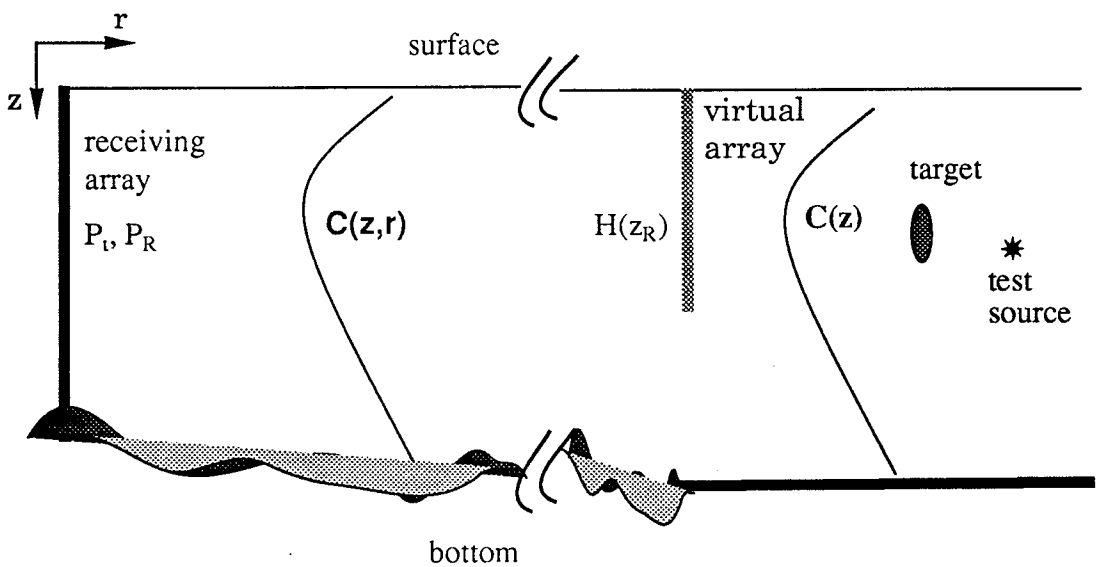

FIGURE 4-8. Schematic diagram of the ocean model with Munk SSP and truncated virtual array.

Fig. 4-11 shows color images of the magnitude of the reconstructed fields, $\hat{Q}(r', z_t)$, for various virtual array lengths. The effect of the virtual array length on the performance of the HAP algorithm is clear. Fig. 4-12 shows horizontal slices, at the target's depth, of the normalized power of the reconstructed

images, $\hat{Q}(r', z_t)$, for various virtual array lengths. As in Fig. 4-10, this plot gives a clear picture of the effect of truncating the virtual array on the width of the main lobe (focus) and the level of the side lobes (ambiguity). Deploying the reference source down to half the water column will create a virtual array of length 2500 meters; in this case the algorithm does not suffer from any major degradation, and a sharp focus at the target is produced with low level side lobes. As we deploy the reference source to shallower depths, we notice widening in the main lobe (defocusing) and a rise in the side lobes (ambiguity). This degradation gets worse and worse with decreasing size of the virtual array, down to a point where the size of the virtual array is comparable to the depth of the channel axis; then the main lobe becomes very fat (smeared focus) and the side lobes rise to or exceed the level of the main lobe (strong ambiguity).

4-2.3 Conclusion

The results of the numerical simulation agree with the theoretical findings which were presented in the previous section. As a measure of comparison between the effect of truncating the receiving array and the virtual array on the performance of the algorithm, we plot the range band width of the half power level of the main lobe as a function of the array length, Fig. 4-13; the array length is measured in terms of the acoustic wave length. It is evident from this plot that the length of the virtual array is crucial to the performance of the algorithm and, therefore, to the quality of the reconstructed image.

The simulation was done for an acoustic frequency of 50 Hz (acoustic wave length 30 meters). We see that as the length of the virtual array becomes close to the depth of the channel axis (1000 meters), the width of the main lobe becomes a significant portion of the target/ reference separation, rendering the algorithm ineffective. For example, when the virtual array extends from the surface to a depth of 1500 meters, the half power range band width is about 4 km; this is equivalent to 16% of the target/reference separation. If we deploy the reference to a yet shallower depth, such as 1250 meters, then the half power range bandwidth is about 9 km which is equivalent to 36% of the target/reference separation. This drastic variation in the algorithm performance is not present with a

change in length of the receiving array, where the half power range band-width is less than 1 km which constitutes about 4% of the target/reference separation.

It is noticeable from the plots that the level of the side lobes is more susceptible to the length of the virtual array than to the length of the receiving array. Therefore, we conclude that the length of the virtual array is more crucial to the focusing and ambiguity performance of the HAP algorithm.

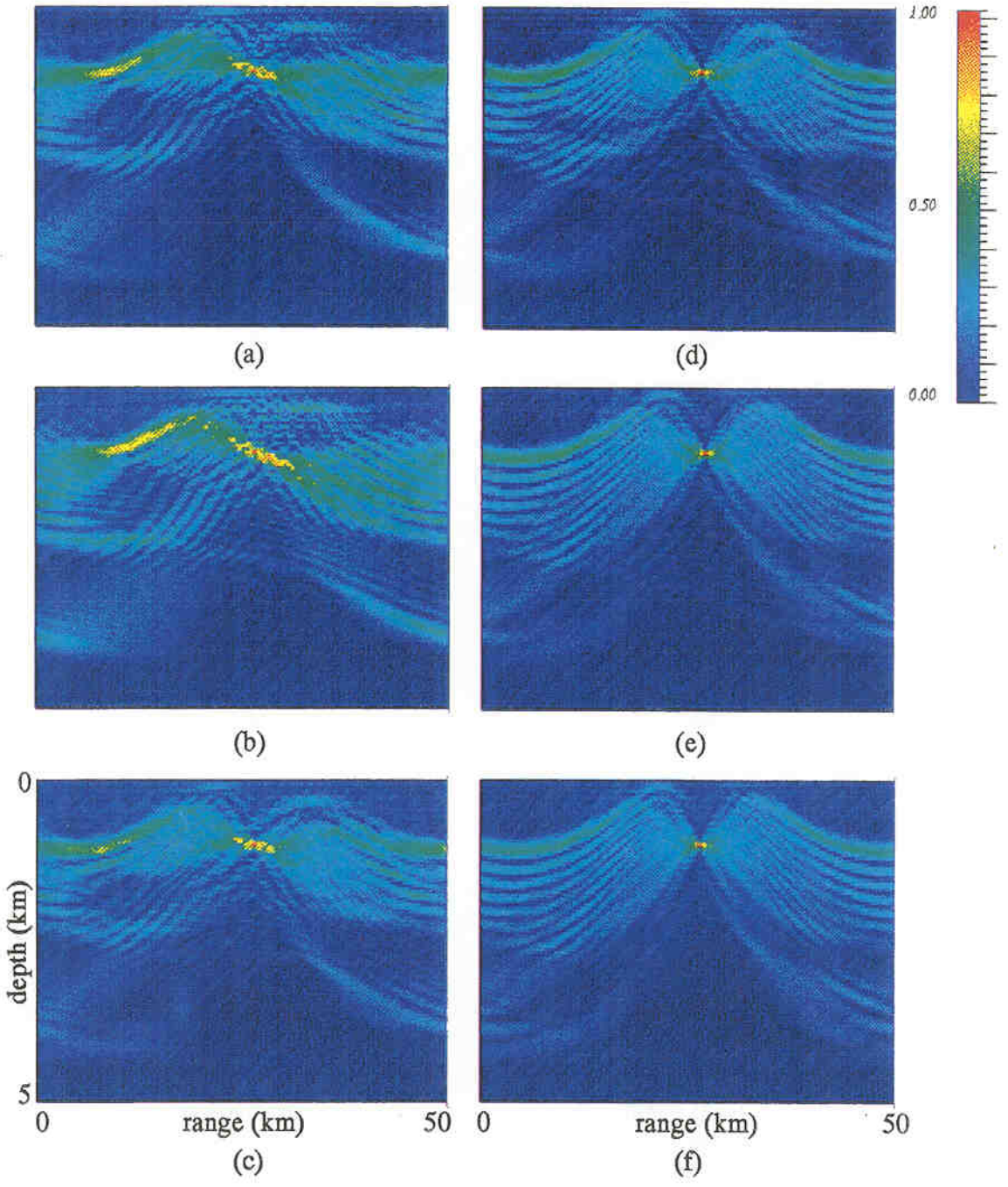

FIGURE 4-9. Magnitude of Q as a function of range and depth where the receiving array length varies: (a) 1000 m, (b) 1250 m, (c) 1500 m, (d) 1750 m, (e) 2000 m, (f) 2500 m.

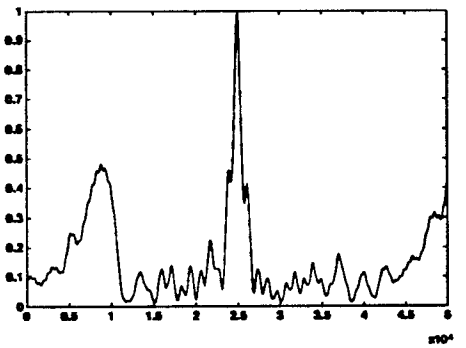

(a)

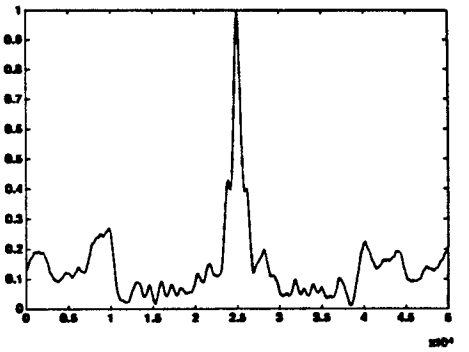

(d)

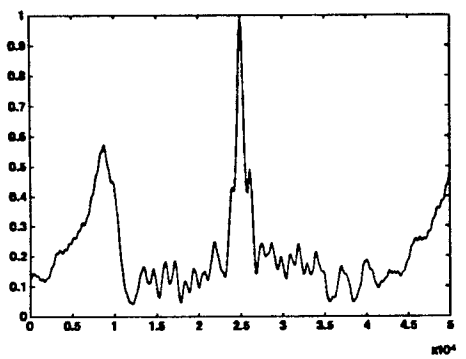

(b)

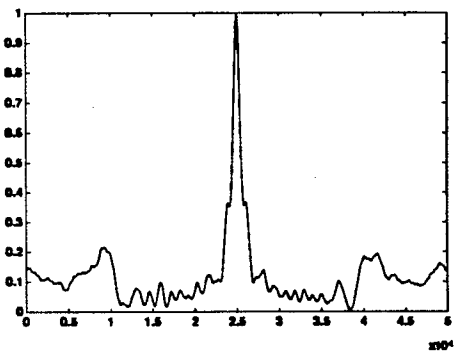

(e)

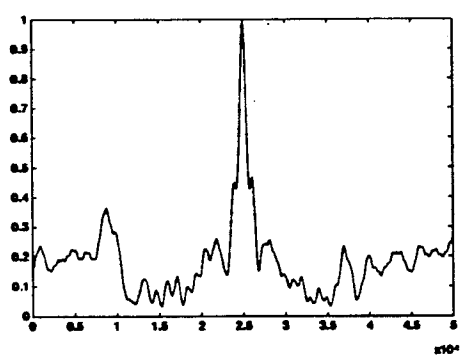

(c)

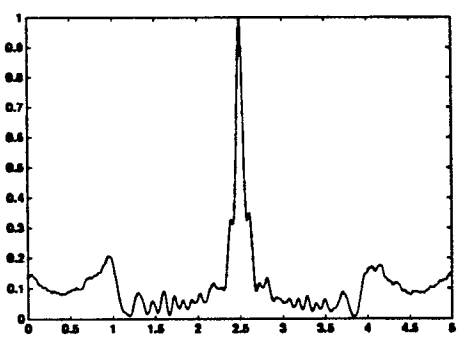

(f)

FIGURE 4-10. Power level of Q as a function of range where the receiving array length varies: (a) 1000 m, (b) 1250 m, (c) 1500 m, (d) 1750 m, (e) 2000 m, (f) 2500 m.

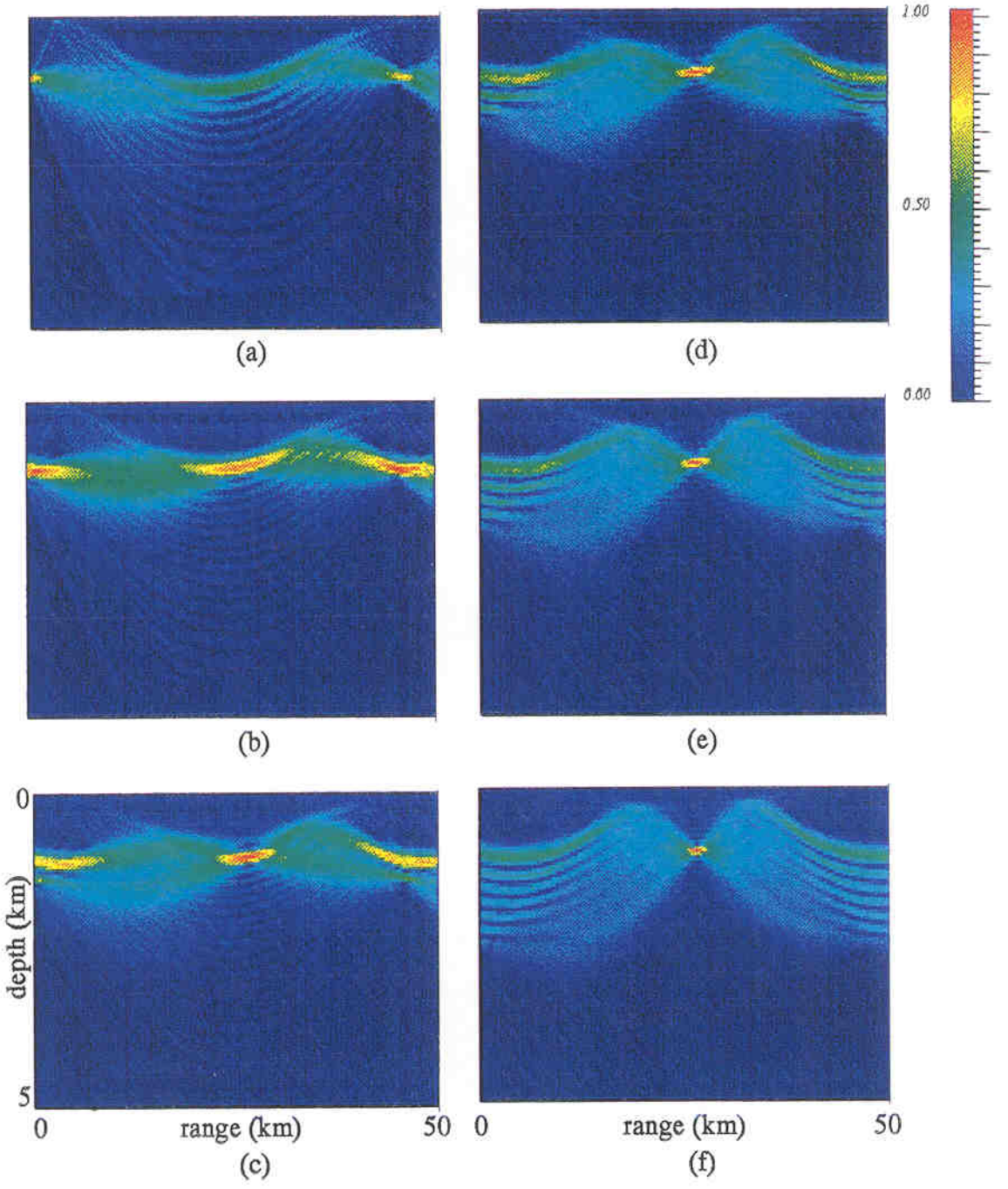

FIGURE 4-11. Magnitude of Q as a function of range and depth where the virtual array length varies: (a) 1000 m, (b) 1250 m, (c) 1500 m, (d) 1750 m, (e) 2000 m, (f) 2500 m.

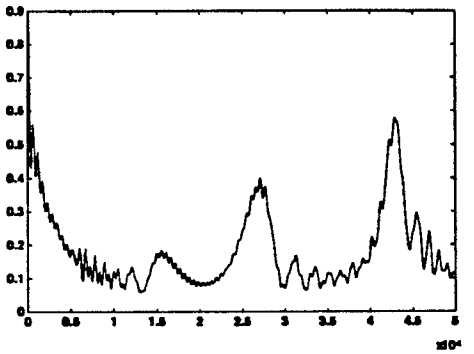

(a)

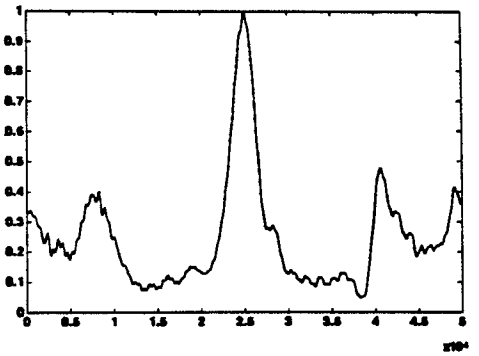

(d)

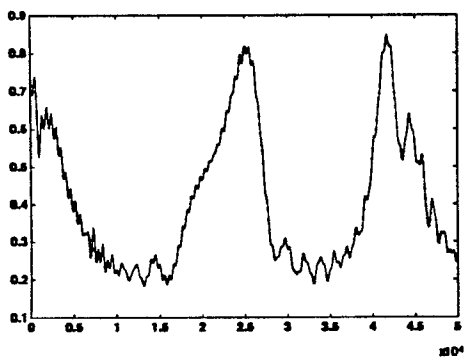

(b)

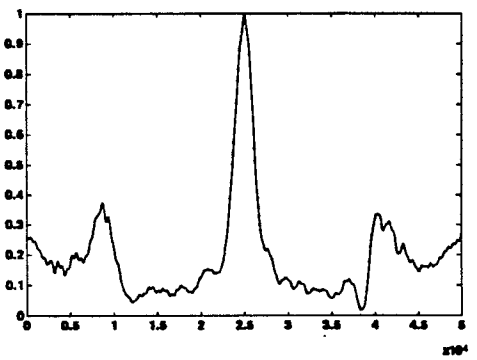

(e)

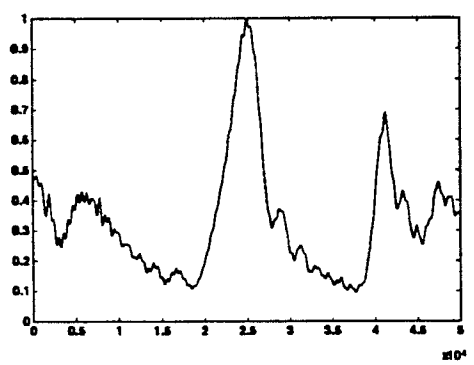

(c)

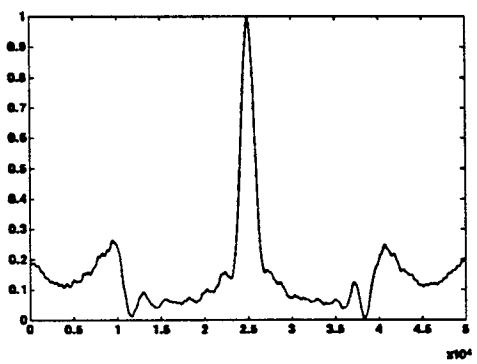

(f)

FIGURE 4-12. Power level of Q as a function of range where the virtual array length varies: (a) 1000 m, (b) 1250 m, (c) 1500 m, (d) 1750 m, (e) 2000 m, (f) 2500 m.

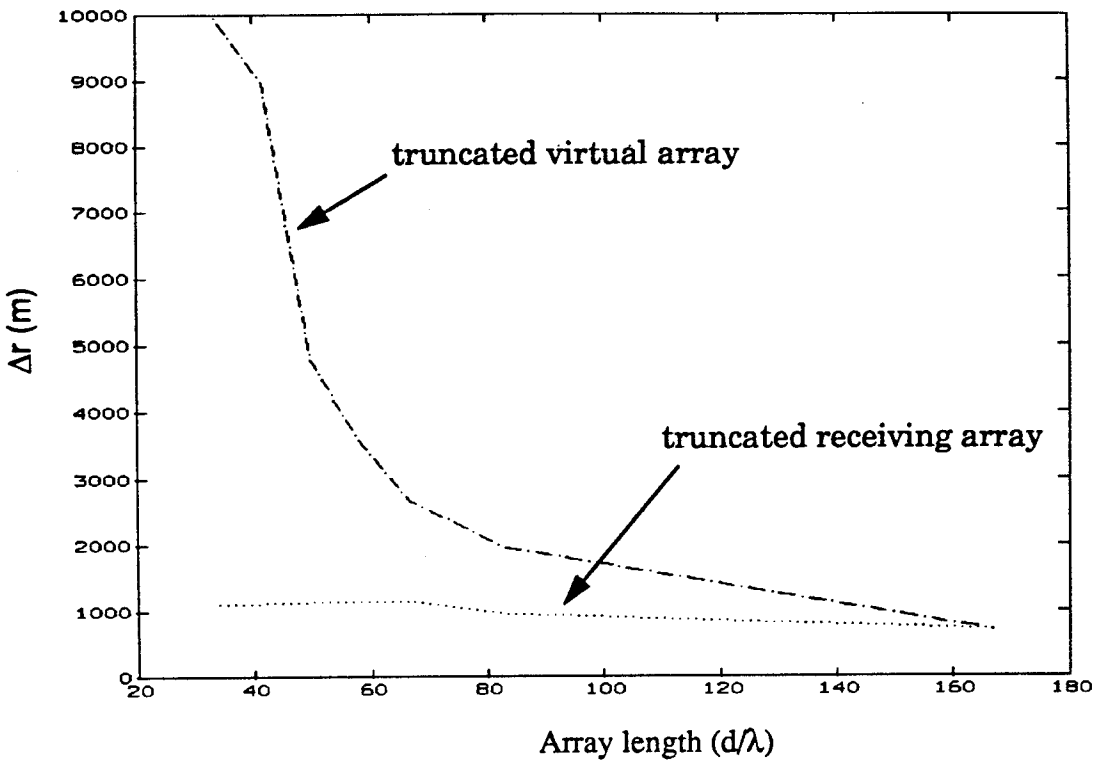

FIGURE 4-13. The half power range band-width as a function of the array length.

CHAPTER 5

Ambient Noise

The performance of the HAP algorithm in the presence of a noise field can be analyzed through the knowledge of the time-space statistics of the field across the receiving array.

The background acoustic noise, or ambient noise, establishes a lower limit on the intensity of useful acoustic signals. Many useful signals in the ocean are noise-like in character. For instance, the presence of many ships, randomly distributed over the ocean surface, results in a component of ambient noise ascribed to "distance shipping" or "ship traffic". However, the noise produced by a single nearby ship is easily identified and localized and is therefore treated as an acoustic signal rather than as part of ambient noise.

5-1 Sources of Ambient Noise

Ambient noise can be divided into three categories; natural, biological, and human-made sources. Each noise source, Fig. 5-1, exhibits different directional (spatial) and spectral (temporal) characteristics. Among the natural sources of noise are seismic disturbances, agitation of the sea surface by wind, and thermal activity of the water molecules. Biological sources include whales, snapping shrimp, croakers, dolphins, and various other fish and ocean mammals. The principal human-made component of ambient noise is the sound generated by distant (over hundreds of nautical miles) shipping, and off-shore drilling.

It is evident that ambient noise levels are highly dependent on geographic location, acoustic transmission characteristics, season of the year, and weather. Even political events, such as the closing or opening of a major canal or port and opening or closing of trade and tourism between different countries, have a measurable effect on the ambient noise through their influence on global shipping patterns.

Table (5-1) shows the dominant noise sources in the different spectrum bands. The very low frequency ambient noise (f < 10 Hz) is generally not of great interest in the design of underwater acoustic systems.

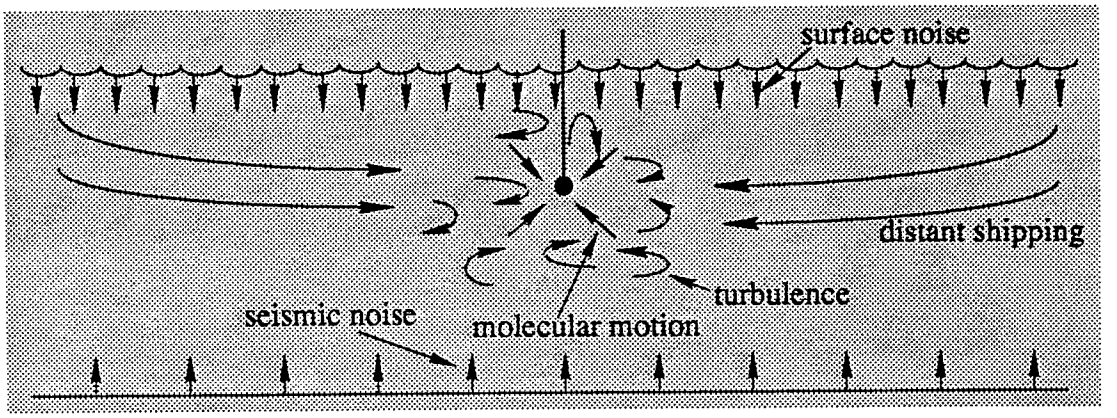

FIGURE 5-1. Conceptual diagram showing some of the sources of deep-water ambient noise as measured at a hydrophone.

Table 5-1: The dominant noise sources in the different spectrum bands

frequency	dominant sources	comment
f < 10 Hz	seismic and ocean turbulent pressure fluctuations	Very low frequency.
10 < f < 100 Hz	distant shipping and offshore drilling	Low frequency. Broad peak around 30 Hz.
100 < f < 1000 Hz	wind	Mid frequency. Broad peak around 500 Hz
f > 50 kHz	thermal agitation of the water molecules	High frequency. Increases at a rate of 6 dB/octave as frequency increases

The low-frequency ambient noise arriving from great distances depends primarily on refraction in the ocean sound channel. Paths requiring multiple bottom reflections endure large attenuation and therefore do not propagate very far. Hence, high ambient noise levels in the low frequency region generally occur in

regions where water depths and sound speed profiles support convergence zone transmission. For typical sound speed profiles in the deep ocean, the vertical angle of arrival at a receiving hydrophone, for acoustic rays that do not intersect either the ocean surface or bottom, is limited approximately to $\pm 15^{o}$ relative to the horizontal. Fig. 5-2 shows a typical angular noise level distribution in the vertical plane for the low-frequency band. The intensity level is in dB with respect to one μPa in a one Hz band per steradian solid angle.

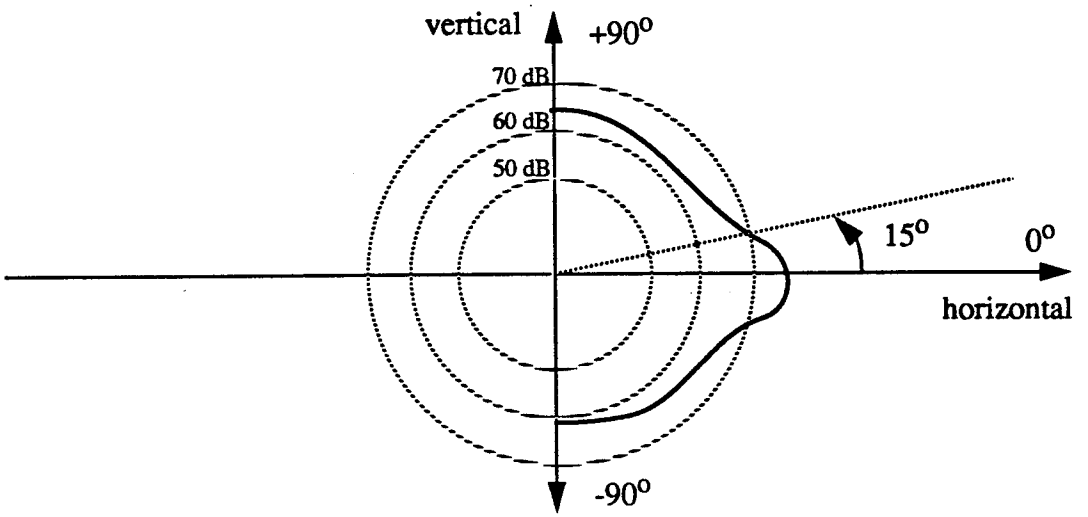

FIGURE 5-2. A typical angular noise level distribution in the vertical plane.

In the midfrequency band, ambient noise is dominated by the effects of wind activity on the sea surface. In very approximate terms [20], the ambient noise level in this band increases about 5 dB for every doubling of wind speed with a wide spectral peak around 500 Hz and decreases at a rate of -5 to -6 dB per octave at higher frequencies. Because of the propagation and geometric properties of the surface generated ambient noise, the intensity level of this noise tends to be higher in the vertical direction than in the horizontal direction.

Average representative ambient noise spectra for different conditions are adequate for qualitative characterization. Fig. 5-3 shows the Wenz curves [21] for different conditions of shipping and wind speed.

When more than one source of noise is present, the effective noise background is obtained by summing the intensities of the contributing sources. When using noise levels (specified in units of spectrum level, dB relative to 1 μPa), this summation process is easily accomplished using the 'power summation' operator, denoted by the symbol ⊕, and defined as

$$\oplus \quad = 10\log \sum_{i=1}^{n} 10^{L_i/10} \tag{5-1}$$

where L_i is the level of i-th noise source in dB and n is the number of contributing noise sources. This operation effectively converts the noise level (L_i) to units of intensity, sums the intensities, and then converts the sum back to units of dB.

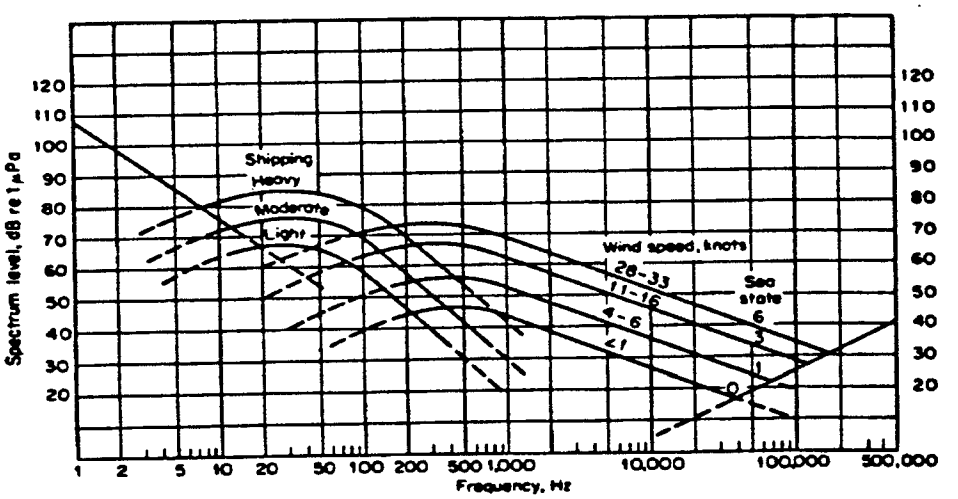

FIGURE 5-3. Average deep-water ambient-noise spectra (Wenz curves).

For example, in Fig. 5-3 at frequency 100 Hz under conditions of moderate shipping and sea state 6, one would obtain noise levels of about 69 dB and 71 dB, respectively. The noise level is obtained from Eq. (5-1) as

$$69dB \oplus 71dB \; = \; 10\log\left[10^{6.9} + 10^{7.1}\right] \; = \; 73dB \tag{5-2}$$

which is 2 dB higher than the noise level due to surface weather alone.

5-2 Depth Dependence

The ambient noise intensity is a very weak function of the receiver depth when operating in the low frequency band, f < 500 Hz. For higher frequencies the depth dependence becomes significant due to absorption.

Measurements of the depth dependence of low-frequency ambient noise were made by Morris (1978) [22] in the Northeastern Pacific Ocean. Hydrophones were suspended from the research platform FLIP (Floating Instrument Platform). Fig. 5-4 shows the sound speed profile, hydrophone depths and average noise profiles in one-third-octave bands for this experiment. There is a decrease of noise level with depth at low frequencies, with a smaller decrease with depth at 500 Hz as wind noise overcomes the dominance of shipping noise. Below the critical depth, where the sound speed equals that at the surface, the fall-off with depth is steeper as the bottom is approached. This is the result of the loss of refracted sound energy. A hydrophone below the critical depth receives energy only through reflection from the surface, the bottom, or both, therefore the received energy from a distant source, at these depths, will be highly attenuated due to interaction with the surface, the bottom, or both.

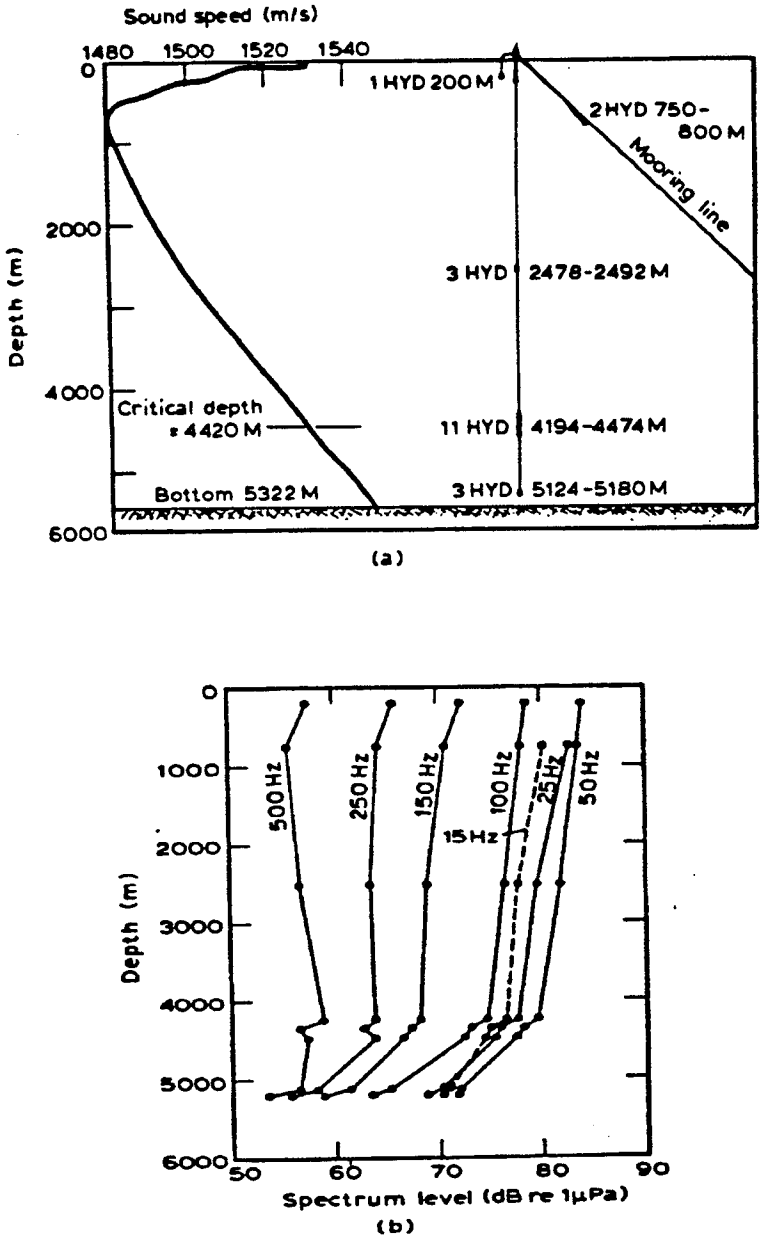

FIGURE 5-4. (a) SSP and hydrophone distribution in the water column. (b) Variation of ambient-noise level with depth at the 1978 experiment in the Northeast Pacific Ocean.

5-3 Directionality

As a first order approximation, the noise field in the ocean might be considered to be isotropic in nature, that is, uniform in all directions, both horizontal and vertical. This approximation is not accurate yet it is useful for qualitative analysis.

Measurements have shown that the ambient noise, in general, is not isotropic. The vertical directionality of ambient noise was measured [23] at frequencies of 112 and 1414 Hz using a 300 ft. long 40 element vertical array, located south of Bermuda. Fig. 5-5 presents polar plots of the ambient noise intensity per unit solid angle $N(\theta)$ arriving at a bottomed hydrophone as a function of vertical angle θ. At 112 Hz, more noise appears to arrive at the hydrophone from the horizontal than from the vertical; this difference diminishes with increasing wind speed. At 1414 Hz the opposite is true in that more noise arrives from the overhead than horizontally; this effect increases with increasing wind speed.

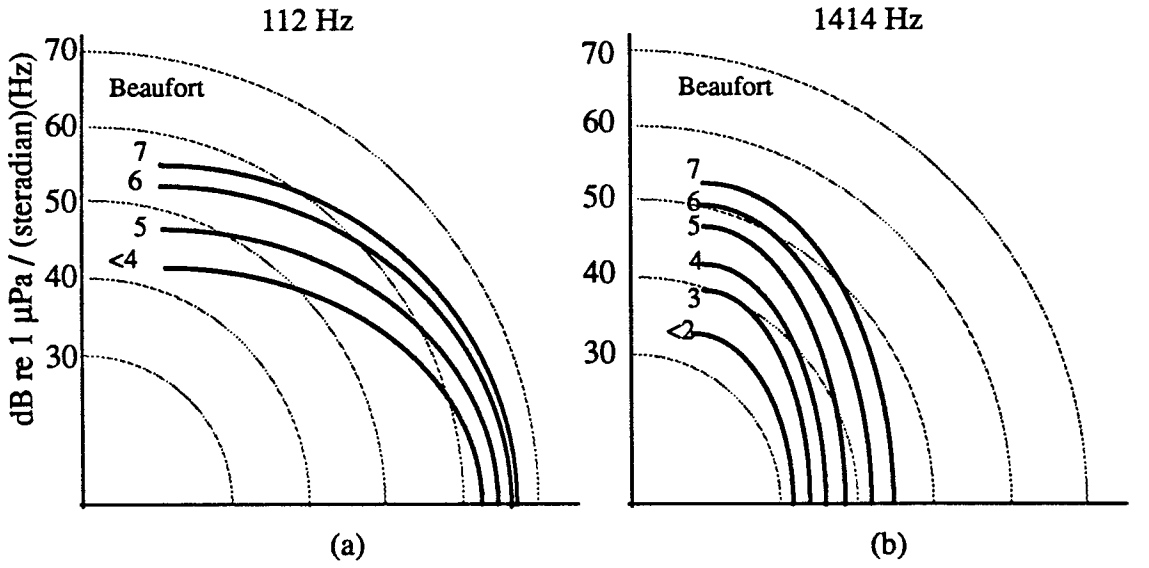

FIGURE 5-5. Distribution of ambient noise intensity in the vertical plane at a bottomed hydrophone (a) at 112 Hz, and (b) at 1414 Hz.

This directional behavior is consistent with the view that low-frequency noise originates at great distances and arrives at the measurement hydrophone via horizontal paths, suffering little attenuation, whereas high frequency noise originates locally at the sea surface more nearly overhead.

The horizontal or azimuthal directionality of ambient noise can be highly variable, particularly at low frequencies. Shipping traffic is the dominant source of noise at low frequencies, and the temporal and spatial variations in shipping densities explain much of the observed azimuthal variation.

5-4 Mathematical Models

Mathematical models of noise in the ocean predict the level and directionality (vertical and horizontal) of noise as a function of frequency, depth, geographic location and time of year.

Noise models can be segregated into two categories; ambient noise models and beam-noise statistics models. Ambient noise models predict the mean levels sensed by an acoustical receiver when the noise sources include surface weather, biology, and commercial activities such as shipping and drilling. Beam-noise statistics models predict the properties of low frequency shipping noise for application to large-aperture, narrow -beam passive sonar systems. The latter models use either analytic or simulation techniques to generate statistical descriptions of the beam noise. In this context, beam noise is defined as the convolution of the receiver beam pattern with the sum of the intensities from the various noise sources. The analytical models calculate statistical properties directly from the components (e.g. source level, propagation loss), while the simulation models use Monte Carlo techniques.

Regardless of type, noise models consist of two components: a transmission loss component, and a noise level and directionality component. In principle, the transmission loss can be computed internal to the noise model or it can be input externally from other (stand-alone) model predictions or from field measurements.

5-4.1 Ambient Noise Models

Ambient noise models consider variable densities of noise sources distributed over large areas. This presents a fair approximation to the generation of wind noise as well as distant shipping noise. Consequently, the transmission loss calculation can be range averaged, as opposed to a point-to-point estimate. This greatly relaxes the accuracy to which transmission loss must be known.

A simple model of ambient noise in the ocean consists of an infinite layer of uniform water with a plane surface along which the noise sources are distributed and the noise level is essentially independent of depth. A more realistic model, however, would include volume absorption and the effect of refraction and boundary reflections over long-range paths.

The low-frequency component of noise due to distant shipping can be computed from knowledge of the density of shipping as a function of azimuth and range from the receiver [24], the source level for the radiated noise of each generic type of merchant ship, and the transmission loss as a function of range between the near surface sources and the depth of the receiver. Then, contributions from successive range rings centered about the receiver can be summed to obtain the level of shipping noise as a function of azimuth at the receiver.

The high-frequency component of noise due to surface weather is usually computed under the assumption that it is locally generated and isotropic. Thus, only the weather conditions (sea state or wind speed) prevailing in the immediate vicinity need to be considered in addition to any localized rain showers or biologic activity.

Modeling of the vertical directionality of deep-water ambient noise can be approached by means of a simple model [2]. Consider a bottomless, uniform ocean, without refraction or attenuation, having a surface covered with a dense, uniform distribution of noise sources. Furthermore, let each unit area of the surface radiate with an intensity $I(\theta)$ at one meter. Then, at point P, in Fig. 5-6 (a), the incremental intensity dI produced by a small circular annulus of area dA at horizontal range r is

$$dI = \frac{I(\theta)\,dA}{l^2} = \frac{I(\theta)\,2\pi r dr}{l^2} \quad . \tag{5-3}$$

But $r = h\tan(\theta)$, so that $dr = h\sec^2(\theta)\,d\theta$. Also, $l = h\sec(\theta)$. Substituting and rearranging, Eq.(5-3) becomes

$$dI = 2\pi I(\theta)\tan(\theta)\,d\theta \quad . \tag{5-4}$$

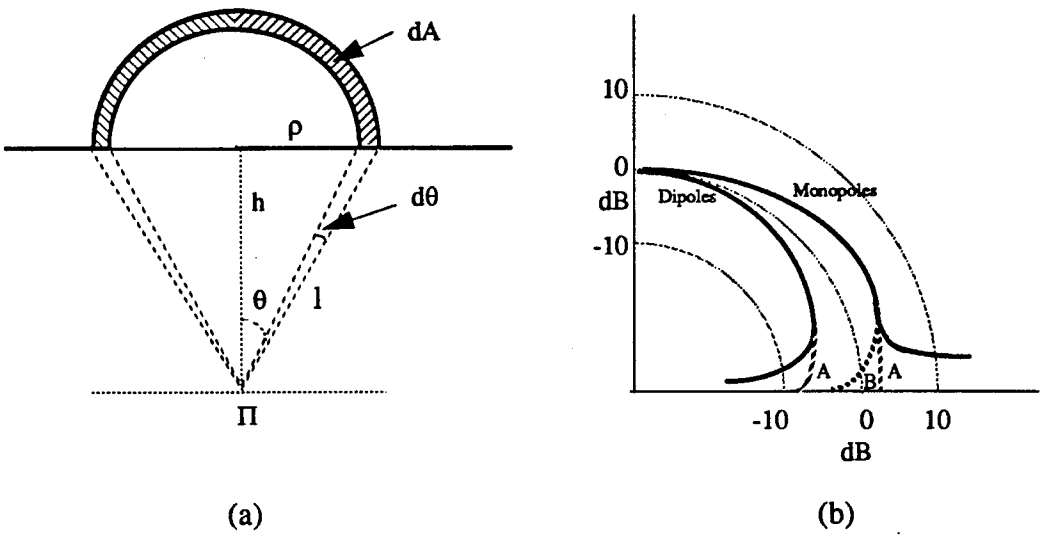

FIGURE 5-6. Simple model for the vertical directionality of ambient noise; (a)geometry with straight-line propagation paths; (b) directional patterns for surface distribution of monopoles and dipoles. The dashed segments near the horizontal show the effect of attenuation and refraction near the sea floor (A) and near the deep sound channel axis (B).

If Ω is a solid angle, then $d\Omega = 2\pi\sin(\theta)\,d\theta$, so that the noise intensity per solid angle, N(θ), becomes

$$N(\theta) = \frac{dI}{d\Omega} = I(\theta)\sec(\theta) \quad . \tag{5-5}$$

When $I(\theta) = I_0$, then Eq.(5-5) yields

$$N(\theta) = I_0\sec(\theta) \tag{5-6}$$

which is the ambient noise intensity per solid angle for a surface distribution of monopole sources. Using distribution of dipole sources (formed by the actual source and its image in the sea surface), the intensity radiated at an angle θ is $I(\theta) = I_0 \cos^2(\theta)$, and the beam pattern of the noise received at a depth below the surface is

$$N(\theta) = I_0 \cos(\theta) \quad . \tag{5-7}$$

At angles near the horizontal ($\theta = 90^o$) the effects of attenuation, refraction and boundary multipath prevent the intensity, for the monopole and the dipole models, from going to either infinity or zero.

Using this simple model, a receiver located within the deep sound channel would not be expected to receive noise arriving along paths near the horizontal since range-independent ray tracing would show that such ray paths do not exist. The beam pattern of the noise from monopole sources would therefore have a maximum at an angle above and below the horizontal (typically $\pm 10^o$ to $\pm 15^o$). This conceptual picture is not always valid in realistic environments; specifically, more sophisticated models would consider the effects of range-dependent refraction, bottom reflection and multipath arrivals.

For low-frequency noise sources ($f < 500$ Hz), the agreement between available observations, Fig. 5-5, and the findings of this simple model, Fig. 5-6, further suggests that a distribution of monopoles ($I(\theta) = I_0$) adequately models the distant shipping noise.

5-5 The Correlation Function for Ambient Noise

The performance of an array of sensors in a noise field depends on the cross-correlation function or equivalently the cross-spectral density function which describes the second-order statistical relationships between all pairs of sensors in the array. This function in turn depends on the directional and temporal properties of the noise field and the geometry of the array. A common model for the ambient noise assumes the noise to be generated from different independent sources in the far field, so the noise at a hydrophone can be considered as the summation of a large number of uncorrelated plane waves propagating from var-

ious directions. Such a field is usually described by a directional density function which indicates the amount of noise power coming from each direction. This model can be simulated by many statistically independent point sources randomly distributed on the surface of a very large sphere with the omnidirectional hydrophones located at the center of the sphere.

Assume the noise field to be an ergodic, wide sense stationary stochastic process, and the noise fields at different frequencies to be statistically independent. Then, take two omnidirectional hydrophones separated by a distance d with the origin located at the midpoint between the sensors, Fig. 5-7. Then, by Parseval's theorem, the directional average noise intensity arriving at the origin from an elemental spherical surface is

$$E\left[\left|n_0(t,\theta,\phi)\right|^2\right] = \int_{-\infty}^{\infty} \overline{\left|N_0(f,\theta,\phi)\right|^2} df \quad , \tag{5-8}$$

and the total average noise intensity at the origin is

$$E\left[\left|n_0(t)\right|^2\right] = \int_{4\pi}\int_{-\infty}^{\infty} \overline{\left|N_0(f,\theta,\phi)\right|^2} df d\Omega \quad , \tag{5-9}$$

where E stands for the expected value, over bar stands for average value, and $d\Omega$ is elemental solid angle.

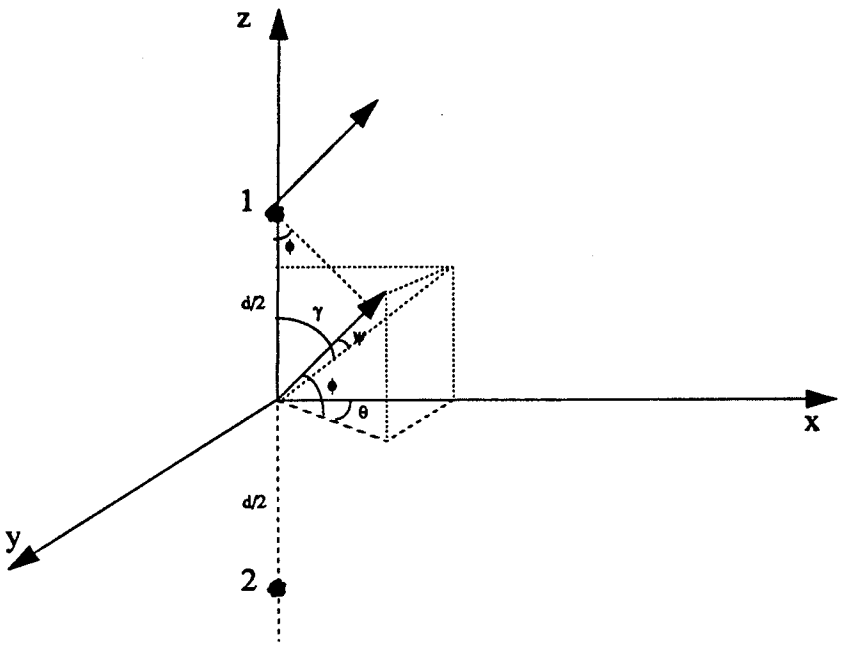

FIGURE 5-7. Polar coordinate system used in noise field description.

Let $\mathbf{x}_1$ and $\mathbf{x}_2$ be the position vectors (r,θ,ϕ) describing the location of the first and second sensors, respectively, and let $\mathbf{u}$ be a unit vector in the direction opposite to that in which the plane wave is propagating. Then if a plane wave propagates past the sensors, the output of the second sensor is a delayed version of the output of the first sensor. That is,

$$n_1(t,\theta,\phi) = n_0(t+\tau,\theta,\phi) \tag{5-10}$$

$$n_2(t,\theta,\phi) = n_0(t-\tau,\theta,\phi) \tag{5-11}$$

where

$$\tau = \frac{1}{2}\boldsymbol{u}\cdot(\boldsymbol{x}_1-\boldsymbol{x}_2)/c \ . \tag{5-12}$$

The directional cross correlation between the two sensors is

$$R_{12}(2\tau, \theta, \phi) = E[n_0(t, \theta, \phi)\, n_0^*(t+2\tau, \theta, \phi)] \quad . \tag{5-13}$$

Since the noise is a wide sense stationary random process, then the noise signal can be presented via Fourier-Stieltjes integral [25] [26]

$$n_0(t, \theta, \phi) = \int_{-\infty}^{\infty} e^{-j2\pi ft} d\eta(f, \theta, \phi) \tag{5-14}$$

where $d\eta(f)$ is called the random amplitude. Since the noise is a zero mean random process, then

$$\langle d\eta(f) \rangle = 0 \quad . \tag{5-15}$$

Eq. (5-13) can be written as

$$E[n_0(t, \theta, \phi)\, n_0^*(t+2\tau, \theta, \phi)] = \int_{-\infty}^{\infty}\int_{-\infty}^{\infty} \langle d\eta(f)\, d\eta^*(\hat{f}) \rangle \times exp[-j2\pi(f-\hat{f})t + j2\pi\hat{f}(2\tau)] \quad . \tag{5-16}$$

Since Eq. (5-16) must be a function of τ only (the process is WSS), then

$$\langle d\eta(f)\, d\eta^*(\hat{f}) \rangle = S(f)\, \delta(f-\hat{f})\, df d\hat{f} \quad ; \tag{5-17}$$

the spectra $d\eta(f)$ at different frequencies must be uncorrelated.

$S(f))$ is the spectral density of the random noise and represents the amount of "power density" at different frequencies

$$S(f) = \overline{|N_0(f, \theta, \phi)|^2} \quad . \tag{5-18}$$

Therefore, Eq. (5-13) can be written as

$$R_{12}(2\tau, \theta, \phi) = \int_{-\infty}^{\infty} \overline{|N_0(f, \theta, \phi)|^2} e^{j2\pi f(2\tau)} df \quad , \tag{5-19}$$

and substituting for τ from Eq. (5-12), we get

$$R_{12}(2\tau, \theta, \phi) = \int_{-\infty}^{\infty} \overline{|N_0(f, \theta, \phi)|^2} e^{j2\pi f(\boldsymbol{u} \cdot (\boldsymbol{x}_1 - \boldsymbol{x}_2)/c)} df \quad . \tag{5-20}$$

Integrating over all possible directions of noise arrival, we get

$$R_{12}(2\tau) = \int_{4\pi} \int_{-\infty}^{\infty} \overline{|N_0(f, \theta, \phi)|^2} e^{j2\pi f(\boldsymbol{u} \cdot (\boldsymbol{x}_1 - \boldsymbol{x}_2)/c)} df d\Omega \quad . \tag{5-21}$$

Interchanging the order of integration, we get

$$R_{12}(2\tau) = \int_{-\infty}^{\infty} \left[\int_{4\pi} \overline{|N_0(f, \theta, \phi)|^2} e^{j2\pi f(\boldsymbol{u} \cdot (\boldsymbol{x}_1 - \boldsymbol{x}_2)/c)} d\Omega \right] df \quad . \tag{5-22}$$

Notice that R_{12} depends on the separation of the sensors and the orientation of the sensors relative to the direction from which the wave is propagating but not the absolute position of the sensors. A field with these properties is spatially homogeneous. Fields composed of a superposition of uncorrelated plane waves are spatially homogeneous: the cross correlation is invariant under translation but not, in general, under rotation of the position of the sensors.

The inner integral in Eq.(5-22) is in the form of a Fourier transform of the noise angular spectral density at frequency f to the linear domain of separation d along the array. Thus, the single frequency spatial cross-correlation for the signals at points 1 and 2 is

$$G_{12}(\boldsymbol{d}, f) = \int_{4\pi} \overline{|N_0(f, \theta, \phi)|^2} e^{j2\pi f(\boldsymbol{u} \cdot \boldsymbol{d}/c)} d\Omega \tag{5-23}$$

where $\boldsymbol{d} = \boldsymbol{x}_1 - \boldsymbol{x}_2$, and $\boldsymbol{u} \cdot \boldsymbol{d} = d\sin\phi$, where ϕ is the elevation angle, Fig. 5-7. Then

$$G_{12}(d,f) = \int_{-\pi}^{\pi}\int_{-\pi/2}^{\pi/2} |N_0(\theta,\phi,f)|^2 e^{j2\pi f\frac{d\sin\phi}{c}} \cos\phi d\phi d\theta \quad . \tag{5-24}$$

$G_{12}(d,f)$ is called the spatial cross-spectral density function.

Thus, the time-space correlation function of the ambient noise is

$$R_{12}(d,\tilde{\tau}) = \int_{-\infty}^{\infty} G_{12}(d,f)\, e^{j2\pi f\tilde{\tau}} df \tag{5-25}$$

which represents the Fourier transform of the spatial cross-spectral density function.

5-6 HAP in the Presence of Ambient Noise

The presence of ambient noise will affect the performance of the HAP algorithm. It will dictate a lower limit on the strength of the detectable target with a given signal-to-noise ratio. We proceed in analyzing the effect of the ambient noise on the HAP algorithm using the following assumptions:

- The noise is a spatially homogeneous, temporally wide sense stationary and ergodic random process;
- The noise is a Gaussian random process with zero mean and temporal-spatial cross-correlation $R_{ij}(d,\tau)$, where i and j designate the i-th and the j-th sensors and d is the separation length between them.

5-6.1 Target Contaminated with Noise

As a first step in evaluating the effect of ambient noise on the performance of the holographic array processor we assume that only the target signal is contaminated with additive, spatially correlated ambient noise with mean equal to zero and strength equal to σ_{nt}^2. Thus the holographic image at reference depth z_{Ri} is

$$\tilde{H}(z_{Ri}) = \int_0^h [P_t(z, r_0; z_t, r_t) + n_t(z)]\, P_{Ri}^*(z, r_0; z_{Ri}, r_R)\, dz \tag{5-26}$$

Since the noise is an ergodic zero-mean normal process, the average holographic image is equal to the holographic image in the absence of the noise

$$\langle \tilde{H}(z_{Ri}) \rangle = H(z_{Ri}) \tag{5-27}$$

and the cross-correlation between the holographic image at depths z_{Ri} and z_{Rj} is

$$\langle \tilde{H}(z_{Ri}) \tilde{H}^*(z_{Rj}) \rangle = H(z_{Ri}) H^*(z_{Rj}) + \int_0^h \int_0^h R_{nt}(|z-\tilde{z}|) P_{Ri}(z) P_{Rj}^*(\tilde{z}) \, dz d\tilde{z} \tag{5-28}$$

where, R_{nt} is the spatial correlation function of target noise, and P_{Ri} and P_{Rj} are the pressure fields from reference sources at depth z_{Ri} and z_{Rj} as measured at the receiving array.

The reconstructed target field is

$$\tilde{Q}(z', r') = \int_0^{h_R} G(z_R; z', r') \tilde{H}^*(z_R) \, dz_R \tag{5-29}$$

where, $G(z_R; z', r')$ is the pressure field from a point test source at location (r', z') as measured (estimated) at the virtual array, and we assume that it is noise-free. Taking the average of Eq. (5-29),we find that the reconstructed field has a mean value equal to that without noise,

$$\langle \tilde{Q}(z', r') \rangle = Q(z', r') . \tag{5-30}$$

The second moment of the reconstructed field is

$$\begin{aligned} \langle \tilde{Q}(\hat{a}_i) \tilde{Q}^*(\hat{a}_j) \rangle &= \langle \int_0^{h_R} G(z_R; \hat{a}_i) \tilde{H}^*(z_R) \, dz_R \int_0^{h_R} G^*(\tilde{z}_R; \hat{a}_j) \tilde{H}(\tilde{z}_R) \, d\tilde{z}_R \rangle \\ &= \int_0^{h_R} \int_0^{h_R} G(z_R; \hat{a}_i) \langle \tilde{H}^*(z_R) \tilde{H}(\tilde{z}_R) \rangle G^*(\tilde{z}_R; \hat{a}_j) \, dz_R d\tilde{z}_R \end{aligned} \tag{5-31}$$

where $\hat{a}_i = (r_i', z_i')$, the i-th location of the scanning test source. Substituting Eq. (5-28) for the cross-correlation of the holographic image, the second moment of the reconstructed field, Eq. (5-31), becomes

$$\langle \tilde{Q}(\hat{a}_i)\tilde{Q}^*(\hat{a}_j)\rangle = \int_0^{h_R}\int_0^{h_R} dz_R d\tilde{z}_R G(z_R;\hat{a}_i)\,G^*(\tilde{z}_R;\hat{a}_j)$$

$$\times\left(H^*(z_R)H(\tilde{z}_R) + \int_0^{h}\int_0^{h} R_{nt}(|z-\tilde{z}|)\,P_R{}^*(z;z_R)\,P_R(\tilde{z};\tilde{z}_R)\,dz d\tilde{z}\right). \tag{5-32}$$

The first term is equal to the reconstructed field in the absence of noise. Therefore, Eq. (5-32) can be written as

$$\langle \tilde{Q}(\hat{a}_i)\tilde{Q}^*(\hat{a}_j)\rangle = Q(\hat{a}_i)Q^*(\hat{a}_j) + \int_0^{h_R}\int_0^{h_R} G(z_R;\hat{a}_i)\,\nu(z_R,\tilde{z}_R)\,G^*(\tilde{z}_R;\hat{a}_j)\,dz_R d\tilde{z}_R \tag{5-33}$$

where

$$\nu(z_R,\tilde{z}_R) = \int_0^{h}\int_0^{h} R_{nt}(|z-\tilde{z}|)\,P_R{}^*(z;z_R)\,P_R(\tilde{z},\tilde{z}_R)\,dz d\tilde{z} \quad . \tag{5-34}$$

Assuming the target strength is σ_t^2, the reference source strength is σ_R^2, and the noise strength is σ_{nt}^2, then

$$\langle \tilde{Q}(z',r')\rangle = (\sigma_t^2\sigma_R^2)^{1/2} Q(z',r') \tag{5-35}$$

and

$$\langle \tilde{Q}(\hat{a}_i)\tilde{Q}^*(\hat{a}_j)\rangle = (\sigma_t^2\sigma_R^2)\,Q(\hat{a}_i)Q^*(\hat{a}_j) +$$

$$\sigma_{nt}^2\sigma_R^2\int_0^{h_R}\int_0^{h_R} G(z_R;\hat{a}_i)\,\nu(z_R,\tilde{z}_R)\,G^*(\tilde{z}_R;\hat{a}_j)\,dz_R d\tilde{z}_R \quad . \tag{5-36}$$

Thus the variance of the reconstructed image field is

$$\sigma_Q^2 = \langle |\tilde{Q}(\hat{a}) - Q(\hat{a})|^2\rangle$$

$$= \sigma_{nt}^2\sigma_R^2\int_0^{h_R}\int_0^{h_R} G(z_R;\hat{a})\,\nu(z_R,\tilde{z}_R)\,G^*(\tilde{z}_R;\hat{a})\,dz_R d\tilde{z}_R \quad , \tag{5-37}$$

and the signal-to-noise ratio at the output of the processor is

$$SNR_Q = \frac{(\sigma_t^2 \sigma_R^2)\,|Q(\hat{a})|^2}{\sigma_{nt}^2 \sigma_R^2 \int_{h_R} \int_{h_R} G(z_R;\hat{a})\, v(z_R, \tilde{z}_R)\, G^*(\tilde{z}_R;\hat{a})\, dz_R d\tilde{z}_R} \quad . \tag{5-38}$$

We notice that the SNR_Q is a function of the target to noise strength; the magnitude of the reference source power, σ_R^2, has no effect on the SNR at the output of the processor. In essence, the second moment of the reconstructed image can be normalized by the strength of the reference source with no other consequence.

5-6.2 Target and Reference are Contaminated with Noise

The target and the reference signals are contaminated with additive, spatially correlated ambient noise. Thus the holographic image is

$$\tilde{H}(z_{Ri}) = \int_0^h \{ [P_t(z, r_0; z_t, r_t; t_1) + n_t(z;t_1)] \times [P_{Ri}(z, r_0; z_{Ri}, r_R; t_2) + n_{Ri}(z;t_2)]^* \}\, dz \tag{5-39}$$

where n_t is the ambient noise associated with the measurement of the target signal at the receiving array, n_{Ri} is the ambient noise associated with the signal from the reference source at reference depth z_{Ri} as measured at the receiving array, and t_1 and t_2 are the times at which we measure the target and reference signals respectively.

Assume the two signals are measured with a time interval greater than the temporal correlation length for the ambient noise. (This correlation length depends on the band width of the input filter at the receiver; see Eq. (5-25).) Therefore, the noise associated with the target is uncorrelated with the noise associated with any reference source. Also, the noise associated with one reference source (reference depth) is uncorrelated with the noise associated with a different reference source (different reference depth), since the measurements

from different reference sources are taken with a time interval greater than the temporal correlation length of the noise. Taking this into account, and assuming that the noise signal is zero-mean, the first moment of the holographic image is

$$\langle \tilde{H}(z_{Ri}) \rangle = \int_0^h [P_t(z, r_0; z_t, r_t) P_{Ri}^*(z, r_0; z_{Ri}, r_R) + P_t(z, r_0; z_t, r_t) \langle n_{Ri}(z) \rangle + P_{Ri}^*(z, r_0; z_{Ri}, r_R) \langle n_t(z) \rangle + \langle n_t(z) n_{Ri}(z) \rangle] dz \tag{5-40}$$

where the average values in the integrand are equal to zero. Therefore, the mean value of the holographic image is

$$\langle \tilde{H}(z_{Ri}) \rangle = H(z_{Ri}) \tag{5-41}$$

which is equal to the holographic image in the absence of ambient noise.

The second moment of the holographic image is

$$\langle \tilde{H}(z_{Ri}) \tilde{H}^*(z_{Rj}) \rangle = \int_0^h \int_0^h \{ [P_t(z;z_t) + n_t(z)] [P_{Ri}(z;z_{Ri}) + n_{Ri}(z)]^* \} \times \{ [P_t(\tilde{z};z_t) + n_t(\tilde{z})] [P_{Rj}(\tilde{z};z_{Rj}) + n_{Rj}(\tilde{z})]^* \}^* dz d\tilde{z} \tag{5-42}$$

where the dependence of the pressure fields on the corresponding ranges is dropped out, merely for compact presentation. After multiplication, and some simplification using the noise properties, we get

$$\langle \tilde{H}(z_{Ri}) \tilde{H}^*(z_{Rj}) \rangle = H(z_{Ri}) H^*(z_{Rj}) + \int_0^h \int_0^h \{ (P_t(z) P_t^*(\tilde{z}) \langle n_{Ri}(z) n_{Rj}(\tilde{z}) \rangle + P_{Ri}^*(z;z_{Ri}) P_{Rj}(\tilde{z};z_{Rj}) \langle n_t(z) n_t(\tilde{z}) \rangle + \langle n_t(z) n_t(\tilde{z}) n_{Ri}(z) n_{Rj}(\tilde{z}) \rangle \} dz d\tilde{z} \quad . \tag{5-43}$$

Note that $\langle n_t(z) n_t(\tilde{z}) \rangle = R_{nt}(|z - \tilde{z}|)$ is the cross-correlation function of the noise associated with the target signal as measured at the receiving array. The

cross-correlation function of the noise associated with the reference sources as measured at the receiving array is

$$\langle n_{Ri}(z)\, n_{Rj}(\tilde{z})\rangle = \begin{cases} R_{nR}(|z-\tilde{z}|) & ;\ i=j \\ 0 & ;\ i\neq j \end{cases} . \tag{5-44}$$

Since the ambient noise is a zero mean Gaussian process, then

$$\begin{aligned}\langle n_t(z)\, n_t(\tilde{z})\, n_{Ri}(z)\, n_{Rj}(\tilde{z})\rangle = {} & \langle n_t(z)\, n_t(\tilde{z})\rangle\langle n_{Ri}(z)\, n_{Rj}(\tilde{z})\rangle + \\ & \langle n_t(z)\, n_{Ri}(z)\rangle\langle n_t(\tilde{z})\, n_{Rj}(\tilde{z})\rangle + \\ & \langle n_t(z)\, n_{Rj}(\tilde{z})\rangle\langle n_t(\tilde{z})\, n_{Ri}(z)\rangle \ . \end{aligned} \tag{5-45}$$

Thus, Eq. (5-43) can be written as

$$\begin{aligned}\langle \tilde{H}(z_{Ri})\, \tilde{H}^{*}(z_{Rj})\rangle = {} & H(z_{Ri})\, H^{*}(z_{Rj}) \\ & + \begin{cases} \int_0^{hh}\!\!\int [P_t(z)\, P_t^{*}(\tilde{z})\, R_{nR}(|z-\tilde{z}|) + \\ \quad R_{nt}(|z-\tilde{z}|)\, P_{Ri}^{*}(z;z_{Ri})\, P_{Rj}(\tilde{z};z_{Rj}) + \\ \quad R_{nt}(|z-\tilde{z}|)\, R_{nR}(|z-\tilde{z}|)\ ]\, dz d\tilde{z} & i=j \\ \int_0^{hh}\!\!\int R_{nt}(|z-\tilde{z}|)\, P_{Ri}^{*}(z;z_{Ri})\, P_{Rj}(\tilde{z};z_{Rj})\, dz d\tilde{z} & i\neq j \end{cases} . \end{aligned} \tag{5-46}$$

Scanning the volume of the ocean in the vicinity of the target with a test point source, and weighting the holographic image at the virtual array by the estimated pressure from the test source, we get the reconstructed image field

$$\tilde{Q}(z', r') = \int_0^{h_R} G(z_R; z', r')\, \tilde{H}^{*}(z_R)\, dz_R \ . \tag{5-47}$$

The first moment of the reconstructed field is

$$\langle \tilde{Q}(z',r') \rangle = \int_0^{h_R} G(z_R;z',r') \langle \tilde{H}^*(z_R) \rangle dz_R = Q(z',r') \tag{5-48}$$

which is the same as in the previous section. The mean value of the reconstructed field is equal to the noise-free reconstructed field. The second moment of the reconstructed field image is

$$\langle \tilde{Q}(\hat{a}_i) \tilde{Q}^*(\hat{a}_j) \rangle = \int_0^{h_R}\int_0^{h_R} G(z_R;\hat{a}_i) \langle \tilde{H}^*(z_R) \tilde{H}(\tilde{z}_R) \rangle G^*(\tilde{z}_R;\hat{a}_j)\, dz_R d\tilde{z}_R \quad . \tag{5-49}$$

Substituting for the second moment of the holographic image, Eq. (5-46), we get

$$\langle \tilde{Q}(\hat{a}_i) \tilde{Q}^*(\hat{a}_j) \rangle = Q(\hat{a}_i) Q^*(\hat{a}_j) + \int_0^{h_R}\int_0^{h_R} G(z_R;\hat{a}_i)\, \nu(z_R,\tilde{z}_R)\, G^*(\tilde{z}_R;\hat{a}_j)\, dz_R d\tilde{z}_R \tag{5-50}$$

where

$$\nu(z_R,\tilde{z}_R) = \begin{cases} \displaystyle\int_0^{h}\int_0^{h} [P_t(z) P_t^*(\tilde{z}) R_{nR}(|z-\tilde{z}|) + \\ R_{nt}(|z-\tilde{z}|) P_R^*(z;z_R) P_R(\tilde{z};\tilde{z}_R) + \\ R_{nt}(|z-\tilde{z}|) R_{nR}(|z-\tilde{z}|)\ ]\, dz d\tilde{z} & i = j \\ \displaystyle\int_0^{h}\int_0^{h} R_{nt}(|z-\tilde{z}|) P_R^*(z;z_R) P_R(\tilde{z};\tilde{z}_R)\, dz d\tilde{z} & i \neq j \quad . \end{cases} \tag{5-51}$$

In comparison with Eq.(5-46), we substituted $P_{Ri}(z;z_{Ri})$ by $P_R(z;z_R)$, and $P_{Rj}(\tilde{z};z_{Rj})$ by $P_R(\tilde{z};\tilde{z}_R)$. The variance of the reconstructed field, Q, is

$$\sigma_Q^2(\hat{a}) = \langle |\tilde{Q}(\hat{a}) - Q(\hat{a})|^2 \rangle \tag{5-52}$$

where we used Eq. (5-48) for the $\langle \tilde{Q}(\hat{a}) \rangle$; therefore, Eq. (5-52) can be written as

$$\sigma_Q^2(\hat{a}) = \langle \tilde{Q}(\hat{a}) \tilde{Q}^*(\hat{a}) \rangle - Q(\hat{a}) Q^*(\hat{a}) \quad . \tag{5-53}$$

Substituting Eq. (5-50) in Eq. (5-53), we get

$$\sigma_Q^2(\hat{a}) = \int_0^{h_R}\int_0^{h_R} G(z_R;\hat{a})\,\nu(z_R,\tilde{z}_R)\,G^*(\tilde{z}_R;\hat{a})\,dz_R d\tilde{z}_R \tag{5-54}$$

where $\nu(z_R, \tilde{z}_R)$ is defined in Eq. (5-51).

Given the temporal-spatial correlation function of the ambient noise, one can find the cross-correlation matrix of the reconstructed field using Eqs. (5-50) and (5-51). The variance of the reconstructed field can be found by subtracting the mean square of the reconstructed field from the diagonal of the cross-correlation matrix, Eq. (5-53).

5-6.3 Isotropic Ambient Noise Model

It is sufficient to assume an isotropic model, which is the least complex mathematically, and yet of practical interest. In the mid-band frequency, 50 Hz to 500 Hz, where the distant shipping and the surface effects are the dominating sources of noise, the total ambient noise at an omnidirectional hydrophone has a nearly isotropic angular distribution.

Fig. 5-8 (a) shows the angular intensity of an isotropic ambient noise model at frequency f as would be measured by an omnidirectional hydrophone, while Fig. 3-8 (b) shows the spatial cross-spectral density function for this model. Notice that when the separation between the sensors is a multiple of $\lambda/2$, the cross spectral density is equal to zero, and, as a consequence, the noise signals measured at these sensors are statistically independent.

Assuming a constant angular intensity, $\overline{|(N_o(\theta,\phi,f))|^2} = \overline{|(N_o(f))|^2}$, the total spectral noise intensity at frequency f is

$$\begin{aligned} I_n(f) &= \int_{4\pi} \overline{|(N_o(f))|^2}\,d\Omega \\ &= 4\pi \overline{|(N_o(f))|^2} \end{aligned} \tag{5-55}$$

The cross spectral density, Eq. (5-24), becomes

$$G_{12}(d,f) = \int_{-\pi}^{\pi}\int_{-\pi/2}^{\pi/2} \overline{|N_0(f)|^2} e^{j2\pi f \frac{d\sin\phi}{c}} \cos\phi d\phi d\theta \ . \tag{5-56}$$

Changing variables, Eq. (5-56) can be written as

$$G_{12}(d,f) = \int_{-\pi}^{\pi}\int_{-1/\lambda}^{1/\lambda} \overline{|N_0(f)|^2} e^{j2\pi\zeta d} \lambda d\zeta d\theta \tag{5-57}$$

where $\zeta = \frac{\sin(\phi)}{\lambda}$, and $\lambda = \frac{c}{f}$. Carrying out the integration we get

$$G_{12}(d,f) = 4\pi\overline{|N_0(f)|^2}\frac{\sin(2\pi d/\lambda)}{2\pi d/\lambda} \quad , \tag{5-58}$$

therefore

$$G_{12}(d,f) = 4\pi\overline{|N_0(f)|^2}\,\mathrm{sinc}(2d/\lambda) \ . \tag{5-59}$$

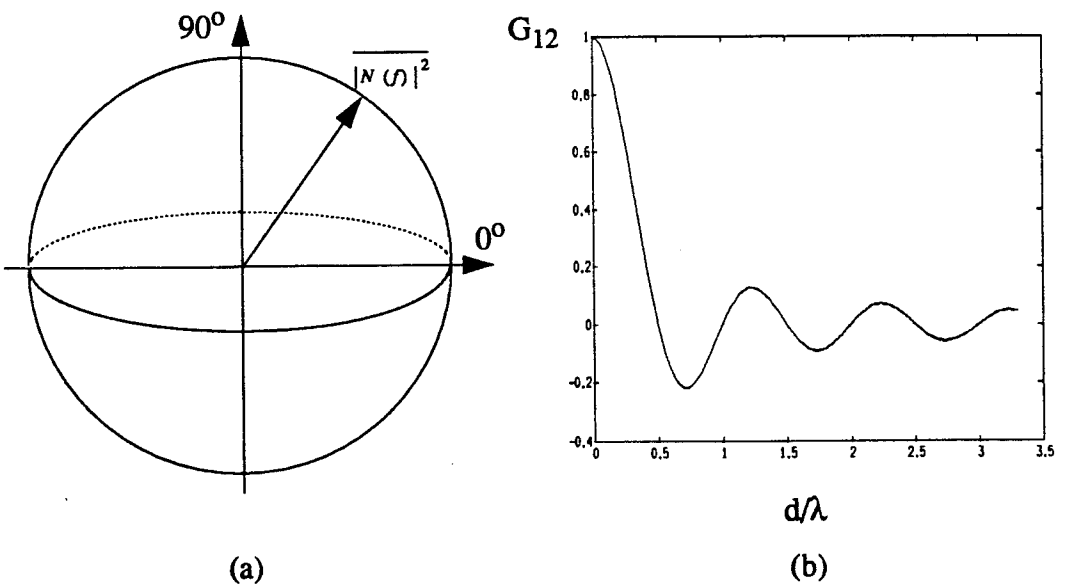

FIGURE 5-8. (a) Angular intensity distribution of the isotropic ambient noise; (b) Normalized cross-spectral density for the isotropic ambient noise.

Thus the time-space cross correlation function for band limited noise is

$$R_{12}(d,\tau) = \int_{-\infty}^{\infty} 4\pi \overline{|N_0(f)|^2} \operatorname{sinc}(2d/\lambda)\, W(f)\, e^{j2\pi f\tau} df \tag{5-60}$$

where W(f) is a weighting window characterizing the frequency band of interest. Assuming that the spectral density is constant over the band of interest, $\overline{|N_0(f)|^2} = A$, and the weighting window is

$$W(f) = \begin{cases} 1 & \text{for } f_{min} \le f \le f_{max} \\ 0 & \text{else} \end{cases}, \tag{5-61}$$

then

$$R_{12}(d,\tau) = \int_{f_{min}}^{f_{max}} 4\pi A \operatorname{sinc}(2d/\lambda)\, e^{j2\pi f\tau} df \ . \tag{5-62}$$

For a time delay $\tau = 0$, the spatial correlation function is

$$R_{12}(d,0) = 4\pi A \int_{f_{min}}^{f_{max}} \operatorname{sinc}(2d/\lambda)\, df$$

$$= \frac{4\pi A}{2d}\left[Si\left(\frac{2df_{max}}{c}\right) - Si\left(\frac{2df_{min}}{c}\right)\right] \tag{5-63}$$

where the special function, sin integral [27], is

$$Si(z) = \int_0^z \frac{\sin(x)}{x} dx \ . \tag{5-64}$$

For more detail about this function see appendix II.

5-6.4 Simulation Results

Figs. 5-9, 5-10, and 5-11 show the magnitude of the normalized mean of $\tilde{Q}$, solid lines, and the effect of adding one standard deviation to the mean value,

dotted lines, for various normalized (transmission loss is not included) target strength. The ambient noise is considered to be isotropic with average intensity of 70 dB. Fig. 5-9 presents these plots for a normalized reference source power of 100 dB, and the normalized target power varies from 90 dB to 160 dB. Fig. 5-10 shows the same plots for a normalized reference source power of 110 dB, and the normalized target power varies from 90 dB to 160 dB. Fig. 5-11 shows the same plots for a normalized reference source power of 120 dB, and the normalized target power varies from 90 dB to 160 dB. In all cases we notice that increasing the target power beyond a certain point, close to the reference source power, will not improve the performance (the focus and ambiguity) of the algorithm. The standard deviation saturates; it becomes a constant as a function of target strength. When the target power is below the reference source power, the algorithm is very dependent on the target strength; the standard deviation gets smaller, the focus gets sharper, and the ambiguity (side lobes) gets weaker with increasing target strength.

A convenient measure of system performance is the signal-to-noise power ratio

$$SNR_Q = \frac{\langle |S_Q|^2 \rangle}{\langle |N_Q|^2 \rangle} \tag{5-65}$$

where S_Q is the noise-free reconstructed image signal, and N_Q is noise associated with the reconstructed image signal.

$$\langle |S_Q|^2 \rangle = QQ^* \tag{5-66}$$

$$\langle |N_Q|^2 \rangle = \int_0^{h_R} \int_0^{h_R} G(z_R;\hat{a}_i)\, \nu(z_R, \tilde{z}_R)\, G^*(\tilde{z}_R;\hat{a}_j)\, dz_R d\tilde{z}_R \ . \tag{5-67}$$

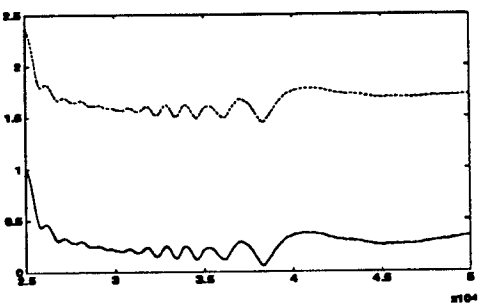

(a)

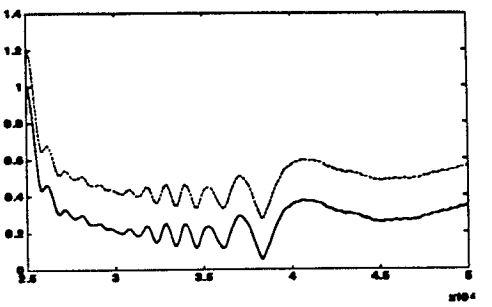

(d)

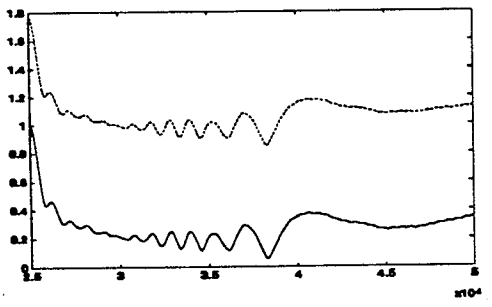

(b)

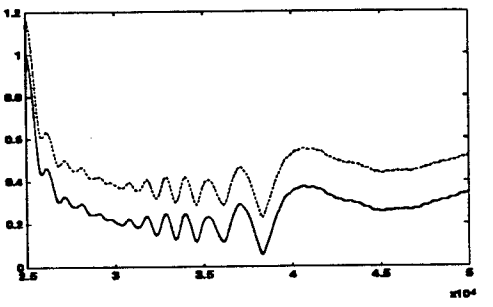

(e)

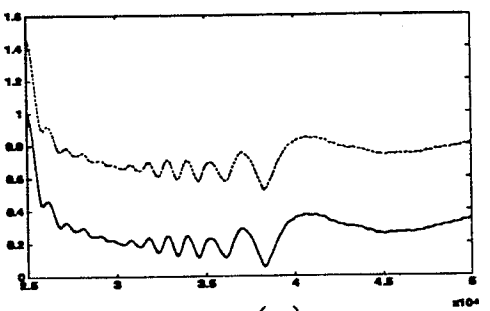

range (m)

(c)

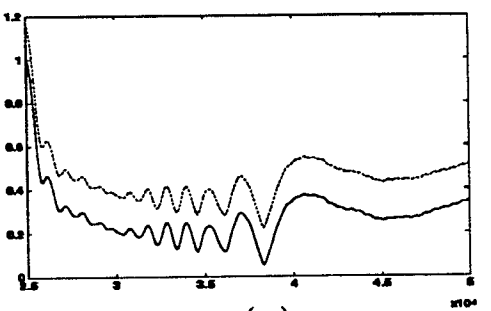

range (m)

(f)

FIGURE 5-9. The mean magnitude of the reconstructed field (solid line) and the mean magnitude plus one standard deviation of the reconstructed field (dotted line). The normalized reference strength is 100 dB, the ambient noise intensity is 70 dB, and the normalized target strength varies: (a) 90 dB; (b) 95 dB; (c) 100 dB; (d) 110 dB; (e) 120 dB; (f) 160 dB.

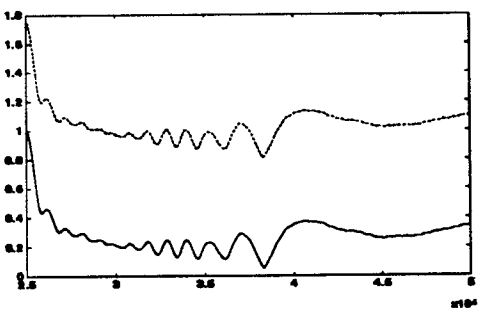

(a)

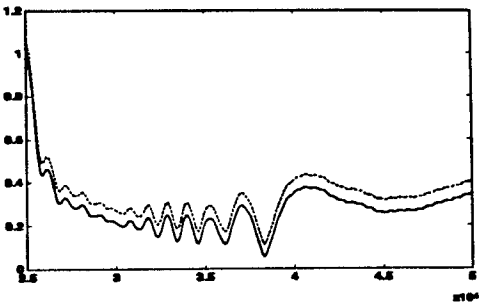

(d)

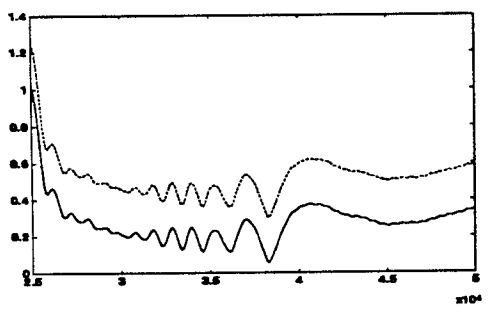

(b)

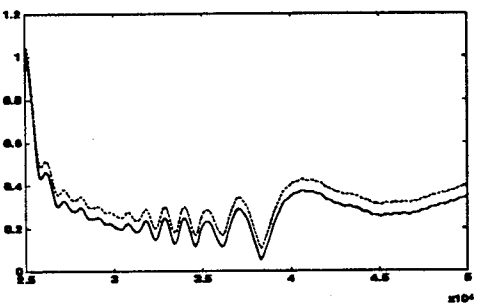

(e)

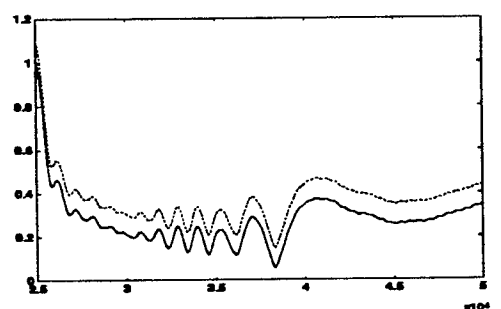

range (m)

(c)

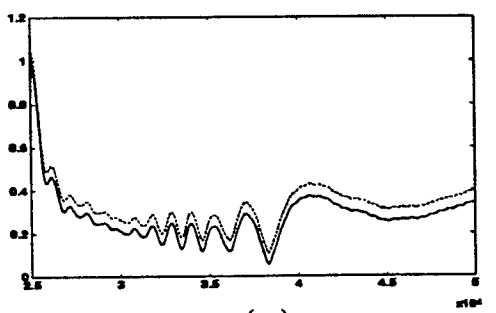

range (m)

(f)

FIGURE 5-10. The mean magnitude of the reconstructed field (solid line) and the mean magnitude plus one standard deviation of the reconstructed field (dotted line). The normalized reference strength is 110 dB, the ambient noise intensity is 70 dB, and the normalized target strength varies: (a) 90 dB; (b) 100 dB; (c) 110 dB; (d) 120 dB; (e) 140 dB; (f) 160 dB.

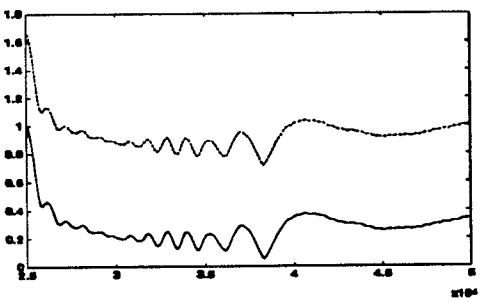

(a)

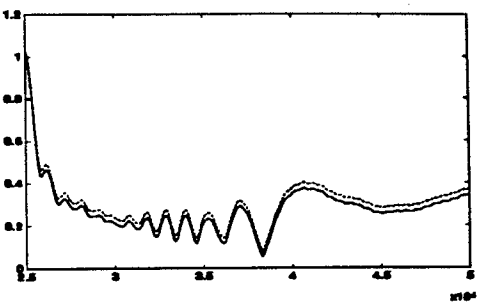

(d)

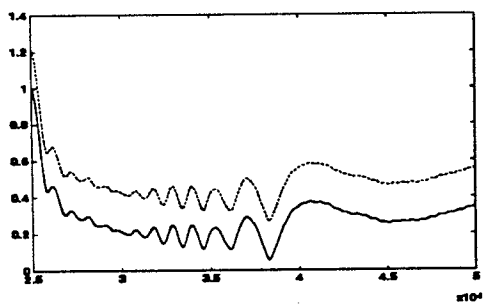

(b)

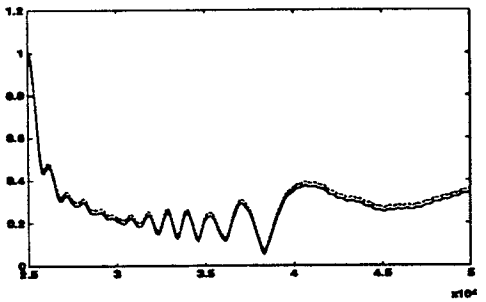

(e)

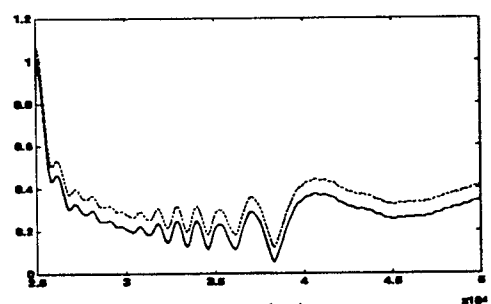

range (m)

(c)

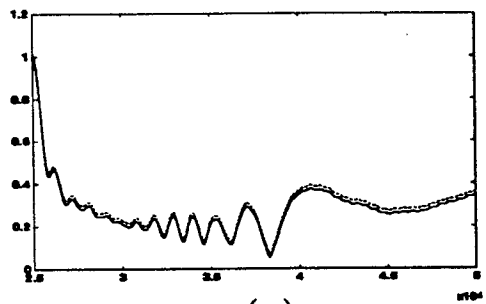

range (m)

(f)

FIGURE 5-11. The mean magnitude of the reconstructed field (solid line) and the mean magnitude plus one standard deviation of the reconstructed field (dotted line). The normalized reference strength is 120 dB, the ambient noise intensity is 70 dB, and the normalized target strength varies: (a) 90 dB; (b) 100 dB; (c) 110 dB; (d) 120 dB; (e) 140 dB; (f) 160 dB.

Acceptable system performance is possible if and only if the signal-to-noise mean power ratio is large, say SNR > 5. Thus the presence of noise, for a given reference source power level, will impose a lower limit on the detectable target signal. From the above analysis, we notice that the noise part of the reconstructed field is a function of both the target and reference signals. Therefore, for a given reference source, increasing the target power level will lead to increasing both the signal and the noise terms of the reconstructed field; this in turn leads to the conclusion that increasing the target power beyond a certain level will lead to no improvement in the SNR.

Fig. 5-12 shows the *SNR* at the output as a function of target strength normalized by the transmission loss, for various normalized reference source strengths, as shown on the curves. We notice that the *SNR* is a weak function of target strength for target power greater than the reference source power, and it is a strong function of the target strength when the latter is less than the reference source power.

Transmission loss due to wave propagation in the ocean was reviewed in chapter 1. As an example, assume the goal is to detect a target at range 100 km with minimum *SNR* of 15 dB, given the reference source power is 190 dB. Since the reference source is near the target, then the signals from both will endure approximately the same amount of transmission loss. Assume the transmission loss is 80 dB; then the normalized reference source power is 110 dB. From the plot and for *SNR* equal to 15 dB, we find the normalized target strength to be 102 dB, so the minimum detectable source strength (with the given minimum *SNR*) is 182 dB. Therefore, a target at that range (transmission loss) with power of 182 dB or greater will be detected with *SNR* of 15 dB or better.

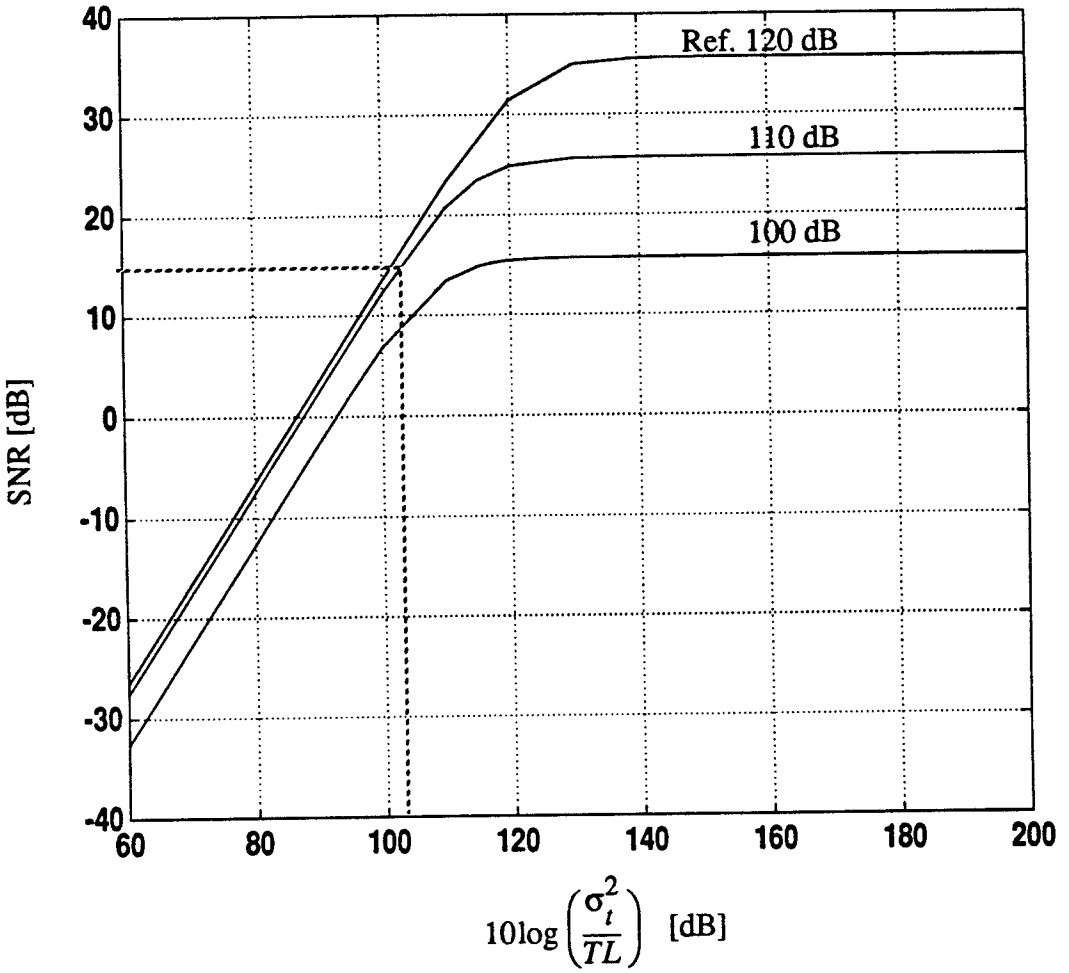

FIGURE 5-12. Signal to noise ratio of the reconstructed field as a function of normalized target strength, and for various normalized reference source power levels (as shown on the curves). The ambient noise intensity is 70 dB.

GENERAL CONCLUSIONS

This dissertation has demonstrated through theoretical analysis and numerical modeling that the holographic array processor can focus with great accuracy the acoustic field from a point source, in a range and depth dependent environment.

It has been shown that truncating the virtual or the receiving array reduces the imaging performance of the holographic array processor. Analytical and numerical analyses showed that the processor performance is more severely degraded by truncating the virtual array.

The performance of the holographic array processor in the presence of ambient noise has been analyzed. Theoretical analysis and numerical simulation revealed that the performance is limited by the signal to noise ratio of the reference source signals.

The following areas are suggested for further research:

- Multiple target detection and tracking using the HAP method.
- The effect of a mismatch in reference and target frequencies.
- The performance of the HAP in the presence of internal waves.
- The performance of the HAP under nonadiabatic propagation conditions.
- The performance of the HAP in shallow water.

REFERENCES

1. J. W. Goodman, W. H. Huntley, D. W. Jackson, and M. Lehman, "Wavefront-reconstruction imaging through random media," Applied Physics Letters, pp. 311-313, 1966.

2. Robert J. Urick, "Principles of underwater sound," McGraw-Hill 1975.

3. Schulkin, M., and H. W. Marsh, "Sound Absorption in Sea Water," J. Acoustical Society of America, vol. 34, p. 864, 1962.

4. Thorp, W. H., "Analytical Description of the Low Frequency Attenuation Coefficient," J. Acoustical Society of America, vol. 42, p. 270, 1967.

5. Wilson, W. D., "Speed of Sound in Sea Water as a Function of Temperature, Pressure and Salinity," J. Acoustical Society of America, vol. 32 p.1357, 1960, and vol. 34 p.866, 1962.

6. Leroy, C. C., "Development of Simple Equations for Accurate and More Realistic Calculation of the Speed of Sound in Sea Water," J. Acoustical Society of America, vol. 46, p. 216, 1969.

7. A. B. Baggeroer, W. A. Kuperman, and H. Schmidt, "Matched Field Processing: Source Localization in Correlated Noise as an Optimum Parameter Estimation Problem," J. Acous. Soc. Am. vol 83, 1988.

8. J. V. Candy and E. J. Sullivan, "Ocean Acoustic Signal Processing: A Method-Based Approach," Technical report, Lawrence Livermore National Laboratory, September 1991.

9. M. B. Porter, R. L. Dicus, and R. G. Fizzel, "Simulations of Matched-Field Processing in a Deep-Water Pacific Environment," IEEE J. Ocean Engineering, vol. OE-12, No. 1, Jan. 1987.

10. S. Unnikrishna Pillai, "Array Signal Processing," Springer-Verlag Publ. Inc. 1989.

11. Joseph W. Goodman, "Introduction to Fourier Optics," McGraw-Hill 1968.

12. C. Allan Boyles, "Acoustic Waveguides: Application to Oceanic Science," John Wiley & Sons, 1984.

13. L. Brekhovskihk and Y. Lysanov, "Fundamentals of Ocean Acoustics," Springervelag, Berlin, 1991.

14. Ivan Tolstoy and C. S. Clay, "Ocean Acoustics: Theory and Experiment in Underwater Sound," Acoustical Society of America, 1987.

15. R. P. Porter, "Transmission and Reception of Transient Signals in a SOFAR Channel," J. Acoust. Soc. Am. 54, pp. 1081-1091, 1973.

16. Walter H. Munk, "Sound Channel in an Exponentially Stratified Ocean, with Application to SOFAR," J. Acoust. Soc. Am., vol. 55, No.2, Feb. 1974.

17. W. H. Munk, "Sound Propagation through a Fluctuating Ocean: Theory and Observation," J. Acoust. Soc. Am. vol. 59, No.4, April 1976.

18. Bruce D. Howe, Personal communications.

19. B. D. Dushaw, P. E. Worcester, B. D. Cornuelle, and B. M. Howe, "On Equation for the Speed of Sound in Seawater," J. Acoust. Soc. Am., in press.

20. R. J. Urick, "Ambient Noise in the Sea," Undersea Warfare Technology Office, Naval Sea Systems Command, Department of the Navy 1984.

21. Wenz, G. M. "Acoustic Ambient Noise in the Ocean: Spectra and Sources," J. Acoust. Soc. Am., vol. 34, 1962.

22. Morris, G. B., "Depth Dependence of Ambient Noise in the Northeastern Pacific Ocean," J. Acoust. Soc. Am., vol. 64, p. 581, 1978.

23. Axelrod, E. H., B. A. Schoomer and W. A. VonWinkle, "Vertical Directionality of Ambient Noise in the Deep Ocean at a Site Near Bermuda," J. Acoust. Soc. Am., vol. 37, p. 77, 1965.

24. Ira Dyer, "Statistics of Distant Shipping Noise," J. Acoust. Soc. Am., vol. 53, 564-570, 1973.

25. S. M. Rytov, Yu. A. Kravtsov and V. I. Tatarskii, "Principles of Statistical Radiophysics 2: Correlation Theory of Random Processes," Springer-Verlag, Berlin Heidelberg 1988.

26. Athanasios Papoulis, "Probability, Random Variables, and Stochastic Processes," Second Edition, McGraw Hill Book Co. 1984.

27. Milton Abramowitz and Irene A. Stegun, "Handbook of Mathematical Functions With Formulas, Graphs, and Mathematical Tables," National Bureau of Standards, Applied Mathematics Series 55, Issued June 1964.

28. F. D. Tappert, "The Parabolic Approximation Method," in Wave Propagation and Underwater Acoustics, edited by J. B. Keller and J. S. Papadakis (Springer, New York, 1977).

29. J. F. Claerbout, "Fundamentals of Geophysical Data Processing," McGraw-Hill, New York, pp. 206-207, 1976.

30. A. Bamberger, B. Engquist, L. Halpern, and P. Joly, "Higher Order Paraxial Wave Equation Approximations in Heterogeneous Media," SIAM J. Appl. Math. 48, pp. 129-154, 1988.

31. M. D. Collins, "Benchmark Calculation for Higher-Order Parabolic Equation," J. Acous. Soc. Am., vol. 87, No. 4, April. 1990.

32. M. D. Collins, "The Time-Domain Solution of the Wide-Angle Parabolic Equation Including the Effects of Sediment Dispersions," J. Acous. Soc. Am., vol. 84, No. 6, Dec. 1988.

33. M. D. Collins, "Applications and Time Domain Solution of Higher-Order Parabolic Equations in Underwater Acoustics," J. Acous. Soc. Am., vol. 86, pp. 1097-1102, 1989.

34. A. Al-Kurd, R. P. Porter, and P. D. Mourad, "Holographic Array Processing in a Range Dependent Ocean," J. Acoust. Soc. Am., 91, No. 4, Pt. 2, p. 2364 (A).

35. P. D. Mourad, A. Al-Kurd, R.P. Porter, "Wavefront Reconstruction Applied to Matched Field Processing in Variable, Multimode Waveguide," Presented at the NATO Advanced Study Institute (Acoustic Signal Processing for Ocean Exploration) July 1992.

36. R. P. Porter, P.D. Mourad, and Azmi Al-Kurd, "Wavefront Reconstruction in Variable Multimode Waveguides," J. Optical Society of America, Vol. 9, No. 11, pp. 1984-1990, November 1992.

37. P. D. Mourad, D. Rouseff, R. P. Porter, and Azmi Al-Kurd, "Source Localization Using a Reference Wave to Correct for Oceanic Variability," J. Acoustical Society of America, August 1992.

38. Robert. P. Porter, P. D. Mourad, and Azmi Al-Kurd, "Wavefront Reconstruction of Acoustic Waves in a Variable Ocean," SPIE International Symposium on Optical Applied Science and Engineering, 'Proceedings vol. 1558 pp. 91-102, July 1991, (invited paper).

39. E. N. Leith and J. Upatnieks, "Holographic Imaging through Diffusing Media," J. Opt. Soc. Am. 56, p. 523, 1966.

40. A. D. Pierce, "Extension of the Method of Normal Modes to Sound Propagation in an Almost-Stratified Medium," J. Acoust. Soc. Am. 37 (1), pp. 19-27 (1965).

41. J. D. Gaskill, "Imaging Through a Randomly Inhomogeneous Medium by Wavefront Reconstruction," J. Opt. Soc. Am. 58, pp. 600-608, 1968.

42. M. B. Porter, R. L. Dicus, and R. G. Fizell, "Simulations of Matched-Field Processing in a Deep-Water Pacific Environment," IEEE, J. Ocean Eng., vol. OE-12, Jan.1987

43. 16. A. D. Pierce, "ACOUSTICS: An Introduction to its Physical Principles and Applications," Acoustical Society of America, Woodbury, New York, 1989.

44. F. S. Chwieroth, A. Nagl., H. Uberall, R. D. Graves, and G. L. Zarur, "Mode Coupling in a Sound Channel with Range-Dependent Parabolic Velocity Profile," J. Acoust. Soc. Am. vol. 64, pp. 1105-1112, 1978.

45. S. M. Jesus, "Normal-Mode Matching Localization in Shallow Water: Environmental and System Effects," J. Acous. Soc. Am., vol. 90 (4), Pt. 1, 1991.

46. A. Tolstoy and O. Diachok, "Acoustic Tomography via Matched Field Processing," J. Acous. Soc. Am. vol. 89 (3), 1991.

47. R. P. Porter, "Dispersion of Axial SOFAR Propagation in the Western Mediterranean," J. Acous. Soc. Am., 1972.

48. R. P. Porter, "Transmission and Reception of Transient Signals in a SOFAR Channel," J. Acoust. Am., 1973.

49. H. Schmidt, A. B. Baggeroer, W. A. Kuperman, and E. K. Scheer, "Environmentally Tolerant Beamforming for High-Resolution Matched Field Processing: Deterministic Mismatch," Acoustic. Soc. Am. 88, pp. 1851-1862, 1990.

50. E. L. Hamilton, "Elastic and Viscoelastic Models for Marine Sediments," (Physics of Sound in Marine Sediments) Edited by Loyd Hampton, Plenum Press, New York and London.

51. M. Collins, Personal communication. The author would like to acknowledge his debt to Mr. Collins for providing the PE code (FEPE).

Appendix I

WKB Approximation

The WKB approximation is used to calculate an approximation to the eigen-numbers. Because the WKB approximation is valid in the geometric-acoustic limit, the mode expansion presented here is simply related in many ways to a ray theory solution. The depth dependent portions of the field are standing waves that must satisfy the differential equation

$$\frac{d^2\Phi_m}{dz^2} + \gamma_m^2 \Phi_m = 0 \qquad \text{(I-1)}$$

where the vertical propagation constant is defined by

$$\gamma_m^2 = k^2(z, r) - \xi_m^2. \qquad \text{(I-2)}$$

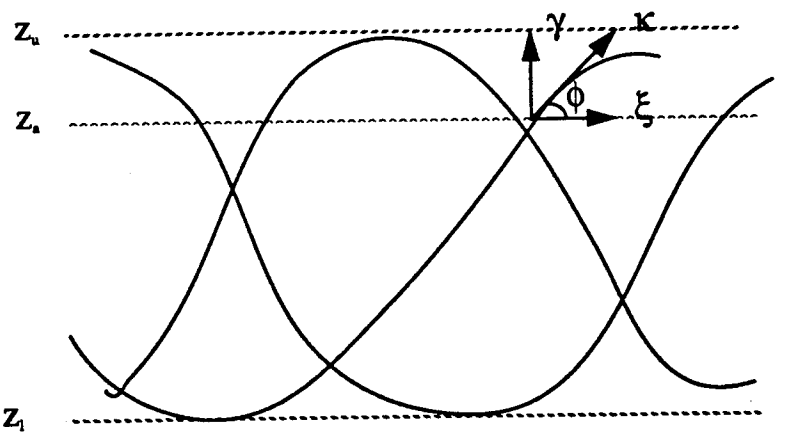

FIGURE I-1. Outward radiating cylindrical wave

The mode-propagation wavenumbers ξ_m are determined from the trapping requirement that the traveling waves that constitute each mode must be out of phase by $m\pi$ radiance.

The WKB approximation, or phase integral method, yields solutions to Eq. (I-1) that are valid far from the turning point, or if

$$\gamma^{-1} \cdot \left| \frac{d}{dz} (\log \gamma) \right| \ll 1 \ . \tag{I-3}$$

The WKB approximation yields upward and downward traveling waves whose phase is plus or minus

$$\theta(z, z', \xi) = \int_{z'}^{z} \gamma(\zeta, \xi)\, d\zeta. \tag{I-4}$$

As the waves are out of phase by $\pi/2$ rad upon reflection, the resonance condition is given by

$$\theta_m(z_u, z_l) = (m + \frac{1}{2})\pi \tag{I-5}$$

where z_u and z_l are the upper and lower turning points. Referencing the field to the upper turning point, the depth dependent field is approximated by

$$\Phi_m(z, \xi) = \begin{cases} \gamma_m^{-1/2} \cos\left[\theta_m(z_u, z) - \frac{\pi}{4}\right] & if (z_l > z > z_u) \\ \frac{1}{2}|\gamma_m|^{1/2} exp\left[-\int_{z_u}^{z} (\xi_m^2 - k^2)^{1/2} d\zeta\right] & if (z < z_u) \ . \end{cases} \tag{I-6}$$

For z below the turning point, the approximate field is found by substituting z_l for z_u and interchanging z and z_l in the damping term. This solution is a good approximation when $k|z - z_u| \gg 1$ and when the turning points are widely spaced. For z meeting these conditions such that $\theta \gg 1$, we can further approximate Φ=0 for z above or below the turning points, and as a result the ray exit angle ϕ is very small. The mode propagation wavenumber can be written as

$$\xi_m(r) = \frac{\omega}{c_a(r)} \cos[\varphi_m(r)] \ . \tag{I-7}$$

Using this notation and that

$$k(z, r) = \frac{N(z, r)}{N(z_a, r)} k(z_a, r) \ , \tag{I-8}$$

we can write

$$\gamma_m^2(z,r) = \omega^2\left[\frac{N^2(z,r)}{N^2(z_a,r)} - \cos^2\varphi_m(r)\right]c^{-2}(z_a,r) \tag{I-9}$$

and

$$\theta_m(z,z_u) = \frac{\omega}{c_a(r)}\int_{z_u}^{z}\left[\left(\frac{N(\zeta,r)}{N(z_a,r)}\right)^2 - \cos^2\varphi_m(r)\right]^{1/2} d\zeta \quad . \tag{I-10}$$

Appendix II

Sine Integral

The sine integral is a special function and is defined as

$$\text{Si}(z) = \int_0^z \frac{\sin(x)}{x} dx. \tag{II-1}$$

In series expansion the sine integral is

$$\text{Si}(z) = \sum_0^\infty \frac{(-1)^n z^{2n+1}}{(2n+1)\,[2n+1]!}, \tag{II-2}$$

and in terms of auxiliary functions is

$$\text{Si}(z)) = \frac{\pi}{2} - f(z)\cos z - g(z)\sin z \tag{II-3}$$

where $f(z)$ and $g(z)$ have asymptotic expansion as

$$f(z) \sim \frac{1}{z}\left(1 - \frac{2!}{z^2} + \frac{4!}{z^4} - \frac{6!}{z^6} + \ldots\right) \qquad (|\arg z| < \pi) \tag{II-4}$$

$$g(z) \sim \frac{1}{z^2}\left(1 - \frac{3!}{z^2} + \frac{5!}{z^4} - \frac{7!}{z^6} + \ldots\right) \quad (|\arg z| < \pi)\ . \tag{II-5}$$

A rational approximation follows, for $1 \le z < \infty$

$$f(z) = \frac{1}{z}\left(\frac{z^4 + a_1 z^2 + a_2}{z^4 + b_1 z^2 + b_2}\right) + \varepsilon_1(z) \tag{II-6}$$

$$g(z) = \frac{1}{z^2}\left(\frac{z^4 + c_1 z^2 + c_2}{z^4 + d_1 z^2 + d_2}\right) + \varepsilon_2(z) \qquad \text{(II-7)}$$

where $a_1 = 7.241163$, $a_2 = 2.463936$, $b_1 = 9.068580$, $b_2 = 7.157433$

$_1 = 7.547478$, $c_2 = 1.564072$, $d_1 = 15.723606$, $d_2 = 12.723684$.

This approximation has the error terms $|\varepsilon_1(z)| < 2\times10^{-4}$, and $|\varepsilon_2(z)| < 10^{-4}$.

A more accurate approximation is

$$f(z) = \frac{1}{z}\left(\frac{z^8 + a_1 z^6 + a_2 z^4 + a_3 z^2 + a_4}{z^8 + b_1 z^6 + b_2 z^4 + b_3 z^2 + b_4}\right) + \varepsilon_1(z) \qquad \text{(II-8)}$$

$$g(z) = \frac{1}{z^2}\left(\frac{z^8 + c_1 z^6 + c_2 z^4 + c_3 z^2 + c_4}{z^8 + d_1 z^6 + d_2 z^4 + d_3 z^2 + d_4}\right) + \varepsilon_2(z) \qquad \text{(II-9)}$$

where $a_1 = 38.027264$, $a_2 = 265.187033$, $a_3 = 335.677320$, $a_4 = 38.102495$

$b_1 = 40.021433$, $b_2 = 322.624911$, $b_3 = 570.236280$, $b_4 = 157.105423$

$c_1 = 42.242855$, $c_2 = 302.757865$, $c_3 = 352.018498$, $c_4 = 21.821899$

$d_1 = 48.196927$, $d_2 = 482.485984$, $d_3 = 1114.978885$, $d_4 = 449.690326$

This approximation has the error terms $|\varepsilon_1(z)| < 5\times10^{-7}$, and $|\varepsilon_2(z)| < 3\times10^{-7}$.

Appendix III

Parabolic Equation (PE) Approximation to the Wave Equation

The propagation of monochromatic sound in the ocean is described by the Helmholtz equation

$$\nabla^2 P + \frac{\omega^2}{c^2} P = 0. \tag{III-1}$$

In cylindrical coordinates this becomes

$$\frac{1}{r}\frac{\partial}{\partial r}\left(r\frac{\partial P}{\partial r}\right) + \frac{1}{r^2}\frac{\partial^2 P}{\partial \varphi^2} + \frac{\partial^2 P}{\partial z^2} + k_0^2 n^2 (r, z, \varphi) P = 0 \tag{III-2}$$

where $n = \dfrac{c_0}{c(r, z, \varphi)}$ is the normalized index of refraction, $k_0 = \dfrac{\omega}{c_0}$ is the reference wavenumber, and c_0 is the reference sound speed.

Rays propagating with angles greater than the maximum exit angle (the angle the ray makes with the horizontal) are not trapped in the ocean and thus do not contribute to the far field. Therefore, for waves propagating in the direction close to the horizontal, a solution to the wave equation may be attempted in the form

$$P(r, z, \varphi) = U(r, z, \varphi) H_0^{(1)}(k_0 r) \tag{III-3}$$

where $H_0^{(1)}$ is the Hankel function of the first kind of order zero (it describes the part of the solution rapidly varying in the r direction), and U is a slowly varying function in all three directions. For $k_0 r \gg 1$, the Hankel function has the asymptotic presentation

$$H_0^{(1)}(k_0 r) \sim \left(\frac{2}{i\pi k_0 r}\right)^{1/2} exp\,[ik_0 r] \quad . \tag{III-4}$$

Substituting Eq. (III-3) in Eq. (III-2) and considering Eq. (III-4) we get

$$\frac{\partial^2 U}{\partial r^2} + 2ik_0 \frac{\partial U}{\partial r} + \frac{1}{r^2}\frac{\partial^2 U}{\partial \varphi^2} + \frac{\partial^2 U}{\partial z^2} + k_0^2 (n^2 - 1) U = 0. \tag{III-5}$$

The variation of U over a distance of the order of the wavelength is small, $\frac{\partial U}{\partial r} \ll k_0 U$. Therefore, the first term in Eq. (III-5) is very small, at least compared to the second term; then

$$2ik_0 \frac{\partial U}{\partial r} + \frac{1}{r^2}\frac{\partial^2 U}{\partial \varphi^2} + \frac{\partial^2 U}{\partial z^2} + k_0^2 (n^2 - 1) U = 0. \tag{III-6}$$

At great ranges from the source we may neglect the curvature of the wavefront and set

$$r d\varphi = dy. \tag{III-7}$$

Then Eq. (III-6) becomes

$$2ik_0 \frac{\partial U}{\partial r} + \frac{\partial^2 U}{\partial y^2} + \frac{\partial^2 U}{\partial z^2} + k_0^2 (n^2 - 1) U = 0. \tag{III-8}$$

If the variation of the sound speed with azimuth can be neglected, then

$$2ik_0 \frac{\partial U}{\partial r} + \frac{\partial^2 U}{\partial z^2} + k_0^2 (n^2 - 1) U = 0. \tag{III-9}$$

The pressure at a point in the far field can be found by evaluating the field at an initial range[1] r_0 by some other method (geometric acoustic, normal mode,...etc.); then numerically, step-by-step, we find the field at the desired point using Eq. (III-9).

---

1. r_0 must be small enough that the field can be evaluated by other methods, but sufficiently large that the parabolic approximation is valid.

A split step algorithm [28] computes the complex pressure as a function of depth at a certain range given the pressure as a function of depth at a smaller range;

$$U(r+\Delta r, z) = F^{-1}\{exp\left[\frac{-i\Delta r s^2}{2k_0}\right] F[U(r,z)]\} exp\left[ik_0(n^2-1)\frac{\Delta r}{2}\right] \quad \text{(III-10)}$$

where r is range, Δr is PE range step, z is depth, $k_0 = \frac{2\pi f}{c_0}$ is reference wavenumber, f is frequency, c_0 is reference sound speed, and $s \triangleq k_0 \sin\varphi$. The Fourier transform notation is used to denote a discrete sine transformation from the physical space (z-space) to the vertical wavenumber space (k-space).

The transform is most efficiently computed for a number of mesh points equal to integer power of two. The set of depth mesh on which the field will be defined is chosen to be 2^N equally spaced depths. These points extend from the surface of the ocean to well below the water-sediment interface;

$$Z_{max} = 2^N \Delta z. \quad \text{(III-11)}$$

Once, the depth mesh is defined, the k-space mesh is determined;

$$\Delta s = k_0 \Delta \sin\varphi \quad \text{(III-12)}$$

where

$$\Delta \sin\varphi = \frac{\sin\varphi_{max}}{2^N}. \quad \text{(III-13)}$$

Appendix IV

Wide Angle PE Code (FEPE)

The parabolic equation (PE) method is an efficient and accurate approach for solving underwater acoustic propagation problems in range-dependent environments. The PE method replaces the reduced wave equation, which is a boundary value problem, with an initial value problem. The narrow angle PE, which is accurate for propagation angles up to 15 degrees, gives rise to phase errors that increase with range [13]. The phase error problem was reduced with the discovery of the wide-angle PE [29], which is accurate for propagation angles up to about 40 degrees. The phase error problem was eliminated entirely with the discovery of a family of higher-order PE's [31] [32], which are accurate for propagation angles of nearly 90 degrees.

The acoustic pressure P is assumed to satisfy the pressure release boundary condition P=0 at the ocean surface, the outgoing radiation condition at infinity, and the reduced wave equation

$$\rho \nabla \bullet \left(\frac{1}{\rho} \nabla P\right) + K^2 P = -4\pi \delta (x - x_s) \qquad \text{(IV-1)}$$

where the complex wavenumber $K = k + i\sigma\beta|k|$ is used to account for sediment loss. Absolute value is used so that energy loss occurs in the direction of propagation. The wavenumber is $k = \omega/c$, $\sigma = [40\pi \log e]^{-1}$, β is the attenuation in decibels per wavelength (dB/λ), ρ is the density, c is the sound speed, and $\mathbf{x}_s$ is the source location.

In cylindrical coordinates Eq. (IV-1) becomes [32]

$$\frac{\partial W}{\partial r} = ik_0 \sqrt{1 + X} W \qquad \text{(IV-2)}$$

where

$$X = k_0^{-2}\left(K^2 - k_0^2 + \frac{\partial^2}{\partial z^2} - \frac{1}{\rho}\frac{\partial \rho}{\partial z}\frac{\partial}{\partial z}\right) \tag{IV-3}$$

where we define $W = r^{1/2}P$ if the environment's range dependence is weak. To reduce the propagation problem to two spatial dimensions, the azimuthal variation was assumed to be negligible. Also, variation in range was assumed to be sufficiently weak that $\frac{\partial \rho}{\partial r}$ can be ignored.

Parabolic equations are based on approximations of the square root function appearing in Eq. (IV-2). The narrow angle PE is derived from the first two terms of the Taylor series expansion. The wide-angle PE is derived from a rational approximation. Bamberger [30] used Pade series to approximate the square root in Eq. (IV-2) and derived the following higher-order PE:

$$\frac{\partial U_n}{\partial r} = ik_0 \sum_{j=1}^{n} \frac{a_{j,n}X}{1 + b_{j,n}X} U_n, \tag{IV-4}$$

where

$$a_{j,n} = \frac{2}{2n+1} \sin^2\left[\frac{j\pi}{2n+1}\right] , \tag{IV-5}$$

$$b_{j,n} = \cos^2\left[\frac{j\pi}{2n+1}\right] , \tag{IV-6}$$

and

$$W \equiv W_n = U_n exp\,(ik_0 r) \ . \tag{IV-7}$$

Eq. (IV-4) is referred to as PE_n.

The computer code FEPE solves PE_n using finite elements for depth discretization and Crank-Nicolson integration in range [33]. The tridiagonal system

solver in FEPE has been designed to minimize computation time. The code uses an elimination scheme that involves sweeping downward to the row corresponding to the ocean bottom to eliminate entries below the main diagonal and sweeping upward to the ocean bottom to eliminate entries above the main diagonal followed by back substitution sweeping up and down from the ocean bottom. In contrast Gaussian elimination involves sweeping downward to eliminate all entries below the main diagonal followed by back substitution sweeping upward.

For problems involving range-dependent ocean depth, the new scheme is more efficient than Gaussian elimination. In the decomposition into upper and lower triangular matrices of Gaussian elimination, it is necessary to repeat sweeping downward from the ocean bottom as the ocean depth varies. With the new scheme, it is necessary to repeat sweeping only for a few rows near the ocean bottom. Since multiplication is faster than division on computers, the tridiagonal system solver has also been improved by replacing divisors with factors. FEPE comes with a set of five starters to calculate the initial field. Usually the Gaussian PE starter or Green's wide-angle PE starter is used to approximate $W(0,z)$.

VITA

Azmi A. Al-Kurd, Ph.D.

University of Washington

AFFILIATIONS:

- Eta-Kappa-Nu; The electrical engineering honor society.
- IEEE: Aerospace and Electronic Systems Society,

  Signal Processing Society,

  Communications Society

  Oceanic Engineering Society,

  Control Systems Society,

  Antenna and Propagation Society.
- Acoustical Society of America.

PUBLICATIONS:

- A. Al-Kurd, R. P. Porter, and P. D. Mourad, "Holographic Array Processing in a Range Dependent Ocean", J. Acoust. Soc. Am., 91, No. 4, Pt. 2, p. 2364 (A), (April 1992).
- P. D. Mourad, A. Al-Kurd, R.P. Porter, "Wavefront Reconstruction Applied to Matched Field Processing in Variable, Multimode Waveguide," Presented at the NATO Advanced Study Institute (Acoustic Signal Processing for Ocean Exploration) (July 1992).
- R. P. Porter, P.D. Mourad, and Azmi Al-Kurd, "Wavefront Reconstruction in Variable Multimode Waveguides", J. Optical Society of America (pp1984-1990, November 1992).
- Robert. P. Porter, P. D. Mourad, and Azmi Al-Kurd, "Wavefront Reconstruction of Acoustic Waves in a Variable Ocean," SPIE International Symposium on Optical Applied Science and Engineering, "Proceedings vol. 1558 pp. 91-102" (invited paper), (July 1991).
- P. D. Mourad, D. Rouseff, R. P. Porter, and Azmi Al-Kurd, "Source Localization Using a Reference Wave to Correct for Oceanic Variability", J. Acoustical Society of America (August 1992).

PROFESSIONAL ACTIVITIES:

- Chairman of the Aerospace and Electronic Systems Chapter (IEEE Seattle Section).
- Served on the Board of DASC 92 "Digital Avionics Systems Conference," that was held in Seattle, October 1992.